Physik Department

# PENeLOPE and AbEx
# On the Way Towards a New Precise Neutron Lifetime Measurement

Rüdiger Picker

Excellence Cluster
Universe

Technische Universität München

Fakultät für Physik der Technischen Universität München

Physik Department E18

# PENeLOPE and AbEx
# On the Way Towards a New Precise Neutron Lifetime Measurement

## Rüdiger Picker

Vollständiger Abdruck der von der Fakultät für Physik der Technischen Universität München zur Erlangung des akademischen Grades eines

Doktors der Naturwissenschaften (Dr. rer. nat.)

genehmigten Dissertation.

| | |
|---|---|
| Vositzender: | Univ.-Prof. Dr. A. J. Buras |
| Prüfer der Dissertation: | |
| | 1. Univ.-Prof. Dr. St. Paul |
| | 2. Univ.-Prof. Dr. K. Schreckenbach |

Die Dissertation wurde am 08. Mai 2008 bei der Technischen Universität München eingereicht und durch die Fakultät für Physik am 11. Juli 2008 angenommen.

# Abstract

The neutron lifetime $\tau_\mathrm{n}$ is a basic parameter in particle physics influencing the early evolution of the universe during Big Bang nucleosynthesis. Its precise knowledge may be used to test the Standard Model of particle physics through a unitarity check of the Cabibbo-Kobayashi-Maskawa matrix. The latest precise measurement $\tau_n = 878.7 \pm 0.8$ s deviates from the current world average, $\tau_n = 886.5 \pm 0.8$ s, by more than $6\,\sigma$, a discrepancy to be resolved.

PENeLOPE, a magneto-gravitational trap avoids the spurious losses encountered in the latest most precise lifetime experiments: using magnetic storage in strong fields from superconducting solenoids it achieves nearly loss-less trapping of ultra-cold neutrons (UCN). Because of gravity, the top may stay open to allow protons emitted from neutron decay to be extracted and detected in realtime. Focus of the measurement can be set on systematic studies because of the large number of stored neutrons.

The design of PENeLOPE, results from extensive Monte Carlo simulations of the trap and the preexperiment AbEx are presented: this experiment was conducted to examine a scheme to remove marginally trapped neutrons, i.e. UCN above the magnetic trap depth but rather long trapping times contributing a systematic error to the measured neutron lifetime.

# Zusammenfassung

Die Lebensdauer des freien Neutrons ist ein elementarer Parameter in der Teilchenphysik. Sie beeinflusst die Entwicklung des Universums während der Urknallnukleosynthese maßgeblich. Außerdem kann eine genaue Kenntnis dieses Werts dazu beitragen, das Standardmodell der Teilchenphysik zu überprüfen; die Unitarität der Cabibbo-Kobayashi-Maskawa Matrize kann getestet werden. Die letzte genaue Messung $\tau_n = 878.7 \pm 0.8$ s weicht vom aktuellen Weltmittelwert $\tau_n = 886.5 \pm 0.8$ s um mehr als $6\,\sigma$ ab, eine wesentlich Diskrepanz, die es zu lösen gilt.

PENeLOPE, eine magnetisch Falle, die gleichzeitig die Schwerkraft ausnutzt, vermeidet die unerklärten Verluste der letzten genauen Lebensdauermessungen: über starke Magnetfelder, die durch supraleitende Spulen erzeugt werden, können ultra-kalte Neutronen (UCN) nahezu verlustfrei gespeichert werden. Aufgrund der Gravitation muss die Falle oben nicht geschlossen werden. Dies macht es möglich die Protonen aus dem $\beta$ Zerfall direkt zu extrahieren und zu zählen. Aufgrund der großen Anzahl an gespeicherten Neutronen kann der Fokus auf systematische Studien gelegt werden.

Das Design von PENeLOPE, Resultate aus Monte Carlo Simulationen der Falle und das Vorexperiment AbEx werden präsentiert: dieses Experiment wurde durchgeführt um die Technik zu überprüfen um marginal gespeicherte Neutronen zu verhindern. Dies sind UCN mit höherer Energie als die Fallentiefe aber trotzdem Speicherzeiten der selben Größenordnung wie $\tau_n$, welche zu einem systematischen Fehler der Lebensdauermessung führen.

# Contents

# Chapter 1

# The Physics Context of Neutron Decay

## 1.1 The neutron, its decay and the CKM matrix

The neutron consists of two down quarks and an up quark. Free neutrons decay into a proton, an electron and an electron-antineutrino

$$\begin{aligned} n &\Rightarrow p + e^- + \overline{\nu}_\mathrm{e} + 0.783\,\mathrm{MeV}, \\ I:\ \frac{1}{2}^+ &\Rightarrow \frac{1}{2}^+, \end{aligned}$$

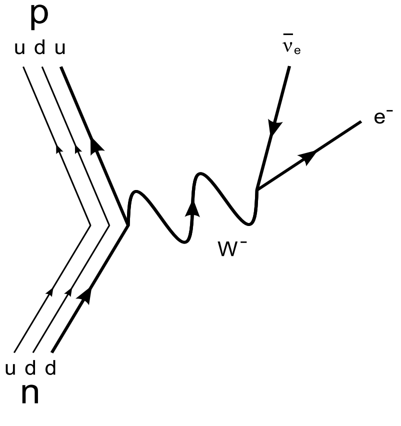

Figure 1.1: Quark picture of neutron $\beta$ decay.

and in leading order in the Standard Model this process is described by a mixed vector/axial-vector current. The Lagrangian can be written as

$$\mathfrak{L}_{\text{int}} = \frac{G_{\text{F}} V_{\text{ud}}}{2\sqrt{2}} \left( V_\mu - \lambda A_\mu \right) \left( v^\mu - a^\mu \right). \tag{1.1}$$

Here the hadronic and leptonic vector and axial-vector currents, constructed from the fermion fields, are

$$V_\mu = \overline{\psi_{\text{p}}} \gamma_\mu \psi_{\text{n}},\ v^\mu = \overline{\psi_{\text{e}}} \gamma^\mu \psi_\nu,\ A_\mu = \overline{\psi_{\text{p}}} \gamma_\mu \gamma_5 \psi_{\text{n}} \text{ and } a^\mu = \overline{\psi_{\text{e}}} \gamma^\mu \gamma_5 \psi_\nu,$$

where $G_{\text{F}}$ is the Fermi constant, $V_{\text{ud}}$ the first element of the Cabibbo-Kobayashi-Maskawa matrix, and $\lambda = g_{\text{A}}/g_{\text{V}}$ the ratio of the axial and vector couplings (see section 1.2).

The Feynman diagram of the decay in the quark picture is visualized in figure 1.1. In this picture, one of the down quark decays into an up quark without involving the two remaining spectator quarks.

The masses of the particles involved in $\beta$ decay and the kinematics are as follows:

$$\begin{aligned}
\text{Neutron mass: } m_{\text{n}} &= 939.57\,\text{MeV}/c^2 \\
\text{Proton mass: } m_{\text{p}} &= 938.27\,\text{MeV}/c^2 \\
\text{Electron mass: } m_{\text{e}} &= 0.511\,\text{MeV}/c^2 \\
\text{Neutrino mass: } m_\nu &< 2\,\text{eV}/c^2 @ 95\%\text{CL} \\
\text{Kinetic energy of the electron: } 0 &\leq E \leq 783\,\text{keV} \\
\text{Kinetic energy of the proton: } 0 &\leq E \leq 751\,\text{eV}.
\end{aligned}$$

Spectra of the electron and proton energy are shown in figure 1.2. The neutron has no charge, but a magnetic dipole moment

$$\mu_{\text{n}} = -1.91304273(45) \cdot \mu_{\text{N}}, \tag{1.2}$$

where $\mu_{\text{N}} = 3.152451236(45) \cdot 10^{-8}\,\text{eV}/\text{T}$ is the nuclear magneton, so

$$\mu_{\text{n}} = -60.3\,\text{neV}/\text{T}. \tag{1.3}$$

The current world average value for the neutron lifetime $\tau_{\text{n}} = 885.7 \pm 0.8\,\text{s}$ [Y$^+$06] is the weighted mean of several measurements and will be discussed later.

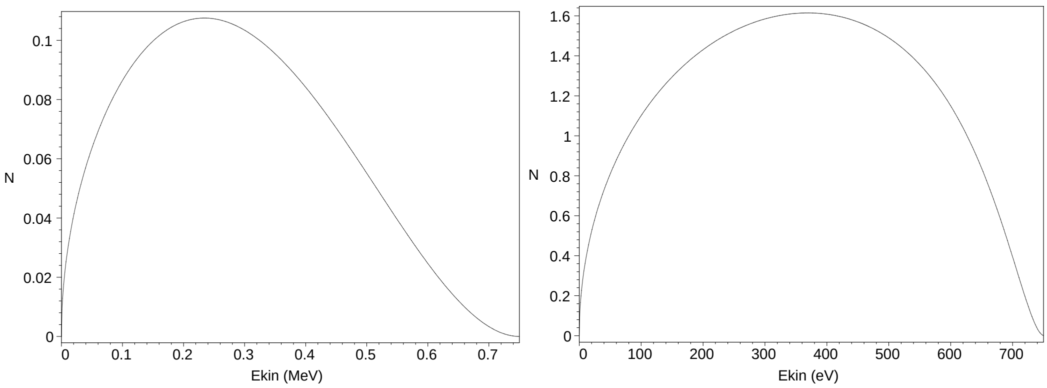

Figure 1.2: Energy spectra of electrons (left) and protons (right) from free neutron decay.

### The Cabibbo-Kobayashi-Maskawa matrix

The coupling strengths for weak processes were supposed to be universal constants and accordingly should be equal for leptonic, semi-leptonic and hadronic processes. This concept, however, did not fit to measured data: the coupling strengths for the semi-leptonic decay of hadrons are smaller than the leptonic ones of the muon decay $\mu^- \Rightarrow e^- + \overline{\nu_e} + \nu_\mu$. For $\beta$ decay, e.g., where a $d$ quark is transformed into a $u$ quark, it is 4% smaller.

A solution to this dilemma was found through the realization that quark flavor or mass eigenstates are not equal to the eigenstates of weak charged currents. In fact, the charged vector bosons $W^\pm$ couple to linear combinations $(|d'\rangle, |s'\rangle)$ of quark mass eigenstates

$$|d'\rangle = \cos\theta_C |d\rangle + \sin\theta_C |s\rangle \tag{1.4}$$

$$|s'\rangle = \cos\theta_C |s\rangle - \sin\theta_C |d\rangle, \tag{1.5}$$

rather than to the mass eigenstates $(|d\rangle, |s\rangle)$ themselves. Here, $\theta_C$ is the Cabibbo quark mixing angle, with $\sin\theta_C \approx 0.225$ [Y+06]. Cabibbo's approach only included two quark families, extending this to all three quark families $\binom{u}{d}$ $\binom{c}{s}$ $\binom{t}{b}$ leads to the $3 \times 3$ Cabibbo-Kobayashi-Maskawa (CKM) matrix

$$\begin{pmatrix} |d'\rangle \\ |s'\rangle \\ |b'\rangle \end{pmatrix} = \begin{pmatrix} V_{ud} & V_{us} & V_{ub} \\ V_{cd} & V_{cs} & V_{cb} \\ V_{td} & V_{ts} & V_{tb} \end{pmatrix} \bullet \begin{pmatrix} |d\rangle \\ |s\rangle \\ |b\rangle \end{pmatrix},$$

where the $|V_{q_iq_j}|^2$ are proportional to the transition probabilities from quark $q_i$ to $q_j$. $V_{ud}$ corresponds to $\cos\theta_C$ above.

According to the Standard Model, which assumes there are only three quark families, this matrix has to be unitary which means $VV^\dagger = 1$. This leads to a criterion for testing the model itself. If for the first row of the CKM-matrix

$$|V_{\mathrm{ud}}|^2 + |V_{\mathrm{us}}|^2 + |V_{\mathrm{ub}}|^2 = 1 \tag{1.6}$$

is not fulfilled, this will be a contradiction to the prerequisites of the three-generation Standard Model [P+03, Byr97, Byr02]. The diagonal elements of the CKM matrix have the largest absolute value. $|V_{\mathrm{ud}}|$ is averaged by the Particle Data Group (PDG) to $0.9746(4)_{\tau_n}(18)_{g_A}(2)_{\mathrm{RC}}$ and contributes most to equation 1.6. The three different uncertainties originate from the neutron lifetime, the axial vector coupling strength and radiative corrections. For the other elements besides $V_{\mathrm{ud}}$ in the first row, the Particle Data Group has adopted the following values [Y+06]:

$$V_{\mathrm{us}} = 0.2255(19) \text{ and } V_{\mathrm{ub}} = 4.31(30) \cdot 10^{-3}.$$

The status of equation 1.6 is

$$|V_{\mathrm{ud}}|^2 + |V_{\mathrm{us}}|^2 + |V_{\mathrm{ub}}|^2 = 0.9999(5)_{\mathrm{stat}}(9)_{\mathrm{sys}}.$$

This result is in good agreement with unitarity, but is a value always in motion. Some years ago, a deviation of $2.7\sigma$ was found [H+02] and a new neutron lifetime value obtained 2005 [S+05] would also suggest another value for $V_{\mathrm{ud}}$.
Therefore, it is crucial to nail down the neutron decay values further to increase the precision in testing the Standard Model [G+01, GGL02].

## 1.2 Neutron decay as a test for the Standard Model

An accurate lifetime of free neutrons can help to determine the first element $|V_{\mathrm{ud}}|$ in the CKM matrix, but to do that, one also needs the ratio $\lambda = g_{\mathrm{A}}/g_{\mathrm{V}}$ of the axial vector and vector coupling strengths. By computing the decay rate at the tree level and applying radiative corrections, $V_{\mathrm{ud}}$ can be computed to an accuracy at the $10^{-4}$ level via

$$|V_{\mathrm{ud}}|^2 = \frac{10^3}{0.1897(1+3\lambda^2)(1+0.0739(8))}\,\frac{1}{\tau_{\mathrm{n}}}\,\mathrm{s}. \tag{1.7}$$

The error originates in an uncertain cutoff in the axial-induced photonic corrections [G+01].

The value $\lambda$ can be measured through several parameters of the neutron $\beta$ decay other than the lifetime: by looking at a polarized neutron almost at rest with polarization $\boldsymbol{\sigma}_{\mathbf{n}}$, the energies $E_{\mathrm{e}}$, $E_{\overline{\nu}}$ and $E_{\mathrm{p}}$ and the momenta $\mathbf{p}_{\mathrm{e}}$, $\mathbf{p}_{\overline{\nu}}$ and $\mathbf{p}_{\mathrm{p}}$ of the decay products, the transition rate can be written down as

$$\begin{aligned} dW(\sigma, \mathbf{p}_{\mathrm{e}}, \mathbf{p}_{\overline{\nu}}) \propto F(E_{\mathrm{e}}) d\Omega_{\mathrm{e}} d\Omega_{\overline{\nu}} \Bigg[ 1 + a \frac{\mathbf{p}_{\mathrm{e}} \mathbf{p}_{\overline{\nu}}}{E_{\mathrm{e}} E_{\overline{\nu}}} + b \frac{m_{\mathrm{e}}}{E_{\mathrm{e}}} \\ + \langle \boldsymbol{\sigma}_{\mathbf{n}} \rangle \left( A \frac{\mathbf{p}_{\mathrm{e}}}{E_{\mathrm{e}}} + B \frac{\mathbf{p}_{\overline{\nu}}}{E_{\overline{\nu}}} + D \frac{\mathbf{p}_{\mathrm{e}} \cdot \mathbf{p}_{\overline{\nu}}}{E_{\mathrm{e}} E_{\overline{\nu}}} + \ldots \right) \Bigg] . \end{aligned} \tag{1.8}$$

In lowest order the correlation coefficients may be related to $\lambda$ by

$$\begin{aligned} a &= \tfrac{1-|\lambda|^2}{1+3|\lambda|^2}, \; b = 0, & A &= -2\tfrac{|\lambda|^2+\Re(\lambda)}{1+3|\lambda|^2}, \\ B &= 2\tfrac{|\lambda|^2-\Re(\lambda)}{1+3|\lambda|^2}, & D &= 2\tfrac{2\Im(\lambda)}{1+3|\lambda|^2}. \end{aligned}$$

$\Re$ and $\Im$ are the respective real and imaginary parts of a complex number. Other correlations with a smaller contribution are omitted [NS05]. The world average value of $\lambda = -1.2695 \pm 0.0029$ [Y+06] can be improved among other things by testing the following correlations:

- The **electron-antineutrino angular correlation coefficient** $a$ can be determined by measuring the recoil spectrum of the proton with high precision. Non-zero values of $a$ show up as a distortion of the spectrum: if the neutrino and the electron emerge in the same direction, the proton needs to have a higher momentum compared to the case when both are emitted in different hemispheres to fulfill momentum conservation. If they emerge in opposite directions, the proton recoil is smaller. An experiment which uses this phenomenon to determine $a$, called "*a*SPECT", has been built by a collaboration also involving the Physics Department E18 of the Technical University Munich. Here, the proton recoil spectrum is integrated above an adjustable electrostatic barrier. Magnetic fields in the apparatus guide the protons and assure $4\pi$ solid angle detection. The experiment's goal is a relative uncertainty of $\Delta a/a \approx 10^{-3}$ [B+02]. First measurements at the Forschungsneutronenquelle Heinz Maier-Leibnitz (FRM II) proved that the principle works, a run to collect statistics was done at Institut Laue-Langevin (ILL) in Grenoble in spring 2008 and should be analyzed by the end of the year.

- The **electron-neutron spin-asymmetry coefficient** $A$ has been studied extensively. The experiment principle is to divide the space of neutron decay into two hemispheres, one in direction of the neutron spin, the other in opposite directions, and to count the number of electrons emitted in these two hemispheres ($N^{\uparrow}$ and $N^{\downarrow}$ respectively). The asymmetry computes to:

$$A = \frac{N^{\uparrow} - N^{\downarrow}}{N^{\uparrow} + N^{\downarrow}}.$$

The best measurements so far were done with the electron spectrometers PERKEO and PERKEO II at ILL, which used a polarized cold neutron beam and magnetic guidance of electrons to their respective detectors. A new setup (PERKEO III) is in the commissioning phase and will take first data for $A$ in 2008. The best current average is $-0.1173(13)$ [Y+06].

- The **Fierz interference term** $b$ is zero in the Standard Model, a deviation requires the existence of scalar (S) or tensor (T) weak interactions in addition to the dominant vector (V) and axial-vector (A) weak interactions and would alter the shape of the electron energy spectrum.

- The determination of the **antineutrino-neutron spin-asymmetry coefficient** $B$ requires polarized neutrons and proton spectroscopy with good energy resolution. At the end of the last century the value $B = 0.9821(40)$ has been published, obtained with a superconducting correlation spectrometer for ultra-cold neutrons at the ILL. Because of the difficulties of this measurement, the relative uncertainty is rather high $\approx 4 \cdot 10^{-3}$. Moreover $\lambda$ is not very sensitive to changes in $B$ because $\partial B / \partial \lambda = 0.075$ [S+98].

- The **triple correlation coefficient** $D$ can be measured by recording proton and antineutrino momenta and the neutron polarization. It is also a criterion for the violation of the time-reversal symmetry and expected to be vanishingly small. The experiment TRINE at ILL could determine a new preliminary limit $D = -3.1 \pm 0.62^{\text{stat}} \pm 4.7^{\text{syst}} \pm 4.7^{\text{syststat}}$ [S+04, Byr02].

Ongoing efforts are made to improve the precision of all these coefficients, which will also enhance the precision of $\lambda$. Therefore, the logical task is to decrease the uncertainty of the neutron lifetime as well, the remaining value necessary to compute $|V_{\text{ud}}|$.
On the one hand $\tau_{\text{n}}$ is a means to test for $\lambda$ by virtue of

$$f \cdot t_{\text{n}} = \frac{K}{|G_{\text{V}}|^2} \frac{1}{1 + 3|\lambda|^2} \tag{1.9}$$

with $t_{\text{n}} = \tau_{\text{n}}/\ln(2)$ and $K = 8120.271(12) \cdot 10^{-10}\,\text{s}/\text{GeV}^4$ [Byr02]. The factor $f$ is the integral of the Coulomb-corrected Fermi phase space function and, including outer radiative corrections $\delta_{\text{R}} > 0$, has the value $f(1+\delta_{\text{R}}) = 1.71335(15)$ [A+04]. The relatively large uncertainty in this factor makes it more feasible to use the experiments above to determine $\lambda$.
On the other hand, more important, via equation 1.7 and an accurate knowledge of $\lambda$, the matrix element $V_{\text{ud}}$ can be determined. This, in turn, contributes to the open question of the CKM unitarity.

## 1.3 Neutron lifetime and cosmology

Besides its role in particle physics, the neutron lifetime is important for cosmology. It plays a vital role in the first few minutes after the Big Bang during primordial nucleosynthesis. During this phase of the universe the first elements heavier than $^1$H ($p$) are produced ($^2$H ($d$), $^3$H, $^3$He, $^4$He, $^6$Li, $^7$Li and $^7$Be) and the temperature has dropped to a level where the reactions

$$\begin{aligned} p + e^- &\rightleftharpoons n + \nu \\ n + e^+ &\rightleftharpoons p + \overline{\nu} \end{aligned}$$

are no longer in thermal equilibrium. The predominant reaction one second after the Big Bang, changing the ratio of protons to neutrons in favor of protons, is the $\beta$ decay of the free neutron

$$n \rightarrow p + e^- + \overline{\nu}.$$

If no other reaction took place, the universe would purely consist of hydrogen, but deuterium formation

$$n + p \rightarrow d + \gamma$$

preserves the neutrons after the temperature has dropped further below 0.1 MeV about 100 s after the Big Bang. The following reactions generate the other elements mentioned above:

$$\begin{aligned} d+p &\rightarrow {}^3\mathrm{He}+\gamma \\ d+d &\rightarrow {}^3\mathrm{H}+p \\ d+d &\rightarrow {}^3\mathrm{He}+n \\ {}^3\mathrm{He}+{}^4\mathrm{He} &\rightarrow {}^7\mathrm{Be}+\gamma \\ {}^3\mathrm{He}+d &\rightarrow {}^4\mathrm{He}+p \\ {}^3\mathrm{He}+n &\rightarrow {}^3\mathrm{H}+p \\ {}^7\mathrm{Li}+p &\rightarrow {}^4\mathrm{He}+{}^4\mathrm{He} \\ {}^7\mathrm{Be}+n &\rightarrow {}^7\mathrm{Li}+p \\ {}^3\mathrm{He}+{}^4\mathrm{He} &\rightarrow {}^7\mathrm{Be}+\gamma \\ {}^3\mathrm{He}+d &\rightarrow {}^4\mathrm{He}+n. \end{aligned}$$

Hence, the yields of specific elements depend on the neutron lifetime and eleven nuclear cross sections[Wei84, B+99].

The neutron lifetime affects the nucleosynthesis in two ways. On the one hand different values of $\tau_n$ imply different interaction rates through influence on the coupling constant $G_F$, on the other hand it directly influences the proton to neutron ratio: the element with the strongest connection to neutron lifetime is helium. If the lifetime is shorter, the helium abundance will become lower. The other important parameter is the baryon-to-photon ratio $\eta_{10}$, because it corresponds to the temperature and baryon density of the early universe. It can be measured through the power spectrum of the cosmic microwave background of the universe, which was recently performed very precisely with the satellite Wilkinson Microwave Anisotropy Probe (WMAP) [S+07].

The element abundances can also be inferred through cosmic observations, in the case of helium through observations of low-metallicity galaxies. Taking all three values, the parameter space is overdetermined and the Big-Bang nucleosynthesis can be tested.

A plot of the parameter space, taken from [M+05], is shown in figure 1.3. It is especially interesting, because two recently discussed values of the neutron lifetime are compared.

The current value $\tau_\mathrm{n} = 885.7 \pm 0.8$ s, adopted by the Particle Data Group, is an average of seven measurements during the last sixteen years, where the major contribution comes from [A+00] . These values and some more, which are not included in the average are presented in tables 2.2 and 2.3.

The lifetime precision of $\Delta\tau_\mathrm{n}/\tau_\mathrm{n} \approx 10^{-3}$ is lower than the achievable accuracy in the determination of $|V_\mathrm{ud}|$ via 1.7 and has to be improved. How-

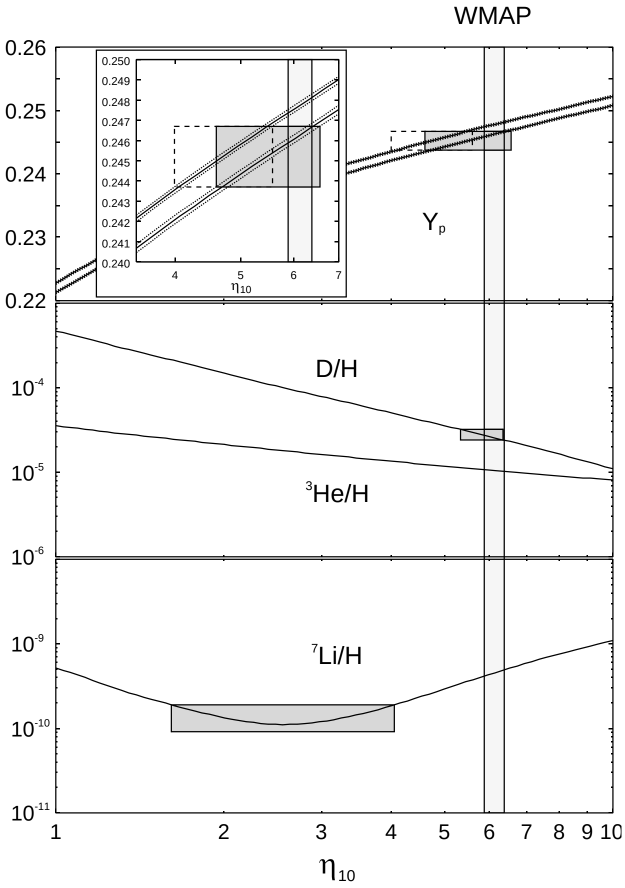

Figure 1.3: The predicted light-element abundances from Big-Bang nucleosynthesis vs. the baryon to photon ratio $\eta_{10}$ compared with observationally inferred abundances and the WMAP data for $\eta_{10}$. Additionally, the allowed region for two values of the neutron lifetime ($\tau_n = 885.7 \pm 0.8$ s and $\tau_n = 878.5 \pm 0.8$ s) are marked as the banded regions [M+05].

ever, because of the lack of electric charge, storing neutrons long enough to be able to keep track of the decay rate is not an easy task.

In principle there are two categories into which neutron lifetime experiments can be classified: Beam methods, using cold neutrons, and bottle or trapping methods utilizing ultra-cold neutrons, which will be discussed in more detail in chapter 2.

# Chapter 2

# Combining the Advantages of Beam and Storage Experiments

In order to trap neutrons, their kinetic energy needs to be very low, which in terms of temperature makes them ultra cold.

## 2.1 UCN in a nutshell

By definition, ultra-cold neutrons (UCN) are free neutrons with a kinetic energy $E_{\mathrm{kin}}$ low enough, so that they are reflected by certain materials for all angles of incidence. The energy range attributed is below around 250 neV. In order to categorize correctly, one has to introduce the Fermi pseudo-potential [G$^{+}$91]. This effective potential arises from averaging over many nuclear potentials in compact materials because the neutron wavelength $\lambda_{\mathrm{n}}$ in this energy region is much larger than nuclear or even molecular dimensions. For $E_{\mathrm{kin}} = 200\,\mathrm{neV}$, e.g., the wavelength equals 400 $\AA$ and the important value for the scattering length is the integral of the potential $U(\mathbf{r})$ over the volume covered by the neutron wave $\int U(\mathbf{r}) d^3\mathbf{r}$. Hence, we can write the Fermi potential in the Born approximation as

$$U_{\mathrm{F}}(\mathbf{r}) = \frac{2\,\pi\,\hbar^2}{m_{\mathrm{n}}} b\,\delta^{(3)}(\mathbf{r}), \tag{2.1}$$

with the bound neutron scattering length $b$ and the three-dimensional Dirac delta function $\delta^{(3)}$. For homogeneous materials the delta functions at the places of the nuclei can be expressed via the number density $N$ and

| Material | | Fermi pot. real $U_F$[neV] | Fermi pot. imag. (abs.) $W_{F,abs}$[neV] | Fermi pot. imag. (upscatt.) $W_{F,upscatt}$[neV] |
|---|---|---|---|---|
| solid deuterium | $^2$H | 108 | $2.3 \cdot 10^{-6}$ | $2.8 \cdot 10^{-5}$ |
| beryllium | Be | 251 | $6.8 \cdot 10^{-5}$ | $6.8 \cdot 10^{-2}$ |
| aluminum | Al | 54.2 | $1.0 \cdot 10^{-3}$ | $6.6 \cdot 10^{-3}$ |
| titanium | Ti | $-50.8$ | $2.5 \cdot 10^{-2}$ | $1.8 \cdot 10^{-2}$ |
| natural nickel | Ni | 245 | $3.0 \cdot 10^{-2}$ | $1.2 \cdot 10^{-1}$ |
| nickel 58 | $^{58}$Ni | 347 | $3.0 \cdot 10^{-2}$ | $1.7 \cdot 10^{-1}$ |
| copper | Cu | 170 | $2.0 \cdot 10^{-2}$ | $1.9 \cdot 10^{-2}$ |
| copper oxide | $Cu_2O$ | 190 | $1.0 \cdot 10^{-2}$ | $5.0 \cdot 10^{-2}$ |
| PE[1] | $(C_2H_4)_n$ | $-8.56$ | $1.9 \cdot 10^{-3}$ | $4.9 \cdot 10^{-1}$ |
| solid oxygen | $sO_2$ | 65 | $5.9 \cdot 10^{-7}$ | $1.3 \cdot 10^{-2}$ |
| stainless steel | 1.4435 | 183 | $1.9 \cdot 10^{-2}$ | $6.6 \cdot 10^{-2}$ |
| DLC[2] | C | 269 | $3.9 \cdot 10^{-5}$ | $3.2 \cdot 10^{-2}$ |

Table 2.1: Fermi pseudo-potentials of common materials; the imaginary part is derived from the absorption cross section and the upscattering cross-section at room temperature. [1] polyethylene, [2] diamond-like carbon.

the formula simplifies to

$$U_F = \frac{2\,\pi\,\hbar^2}{m_n} N b. \tag{2.2}$$

Owing to equation 2.2, a material wall is like a step-potential for neutrons. If $U_F$ is larger than $E_{kin}$, they will be reflected and, following the laws of quantum-mechanics, the neutron wave function will only penetrate the material on the scale of its wavelength $\lambda_n$ which corresponds to $10^{-7}$ m. This makes it possible to store neutrons for a longer period of time. The arising possibilities were already studied in great detail around 1960 [Zel59]. Nonetheless, the reflection process is not perfect; many materials also have an upscattering or absorption cross section for neutrons, which in the simple quantum-mechanical step-potential picture translates into an imaginary component of the potential $V_F = U_F + iW_F$ (cf. chapter 6.1).
Some typical values of Fermi potentials (real and imaginary part) and the resulting critical neutron velocities can be seen in table 2.1. These were

| $\tau_n[s]$ | **Method** | **Year** | **Group** |
|---|---|---|---|
| $881 \pm 8$ | detect $p$ in realtime | 1978 | Bondarenko |
| $878 \pm 10 \pm 19$ | pulsed beam | 1988 | Last |
| **$891 \pm 9$** | **store $p$, flush, detect** | **1988** | **Spivak** |
| **$889.2 \pm 3.0 \pm 3.8$** | **store $p$, flush, detect** | **1996** | **Byrne** |
| **$886.3 \pm 1.2 \pm 3.2$** | **in-beam $n$, trapped $p$** | **2005** | **Nico** |

Table 2.2: Results for $\tau_n$ measured in beam experiments [Y⁺06]. The results included in the PDG world average are printed bold face.

calculated using neutron scattering data from the NIST[1] neutron scattering database [Sea92]. For UCN physics both mechanisms, absorption as well as upscattering, are losses because upscattered neutrons have an energy much higher than the real part of the Fermi potential and can therefore no longer be stored. The loss mechanisms will be discussed in chapter 5, but in most cases a neutron with $E_{\text{kin}} < U_{\text{F}}$ will bounce off a wall $10^3$ to $10^5$ times before being captured.

## 2.2 Storage versus beam experiments

The two types of experiments to measure the neutron lifetime both have their advantages and limitations.

Cold neutrons have kinetic energies in the range $5 \cdot 10^{-5}\,\text{eV} \leq E_{\text{kin,n}} \leq 0.025\,\text{eV}$, a collimated beam can be produced using rectangular nickel-coated boron glass tubes. The lifetime of the neutron in such a beam may be determined by detecting the decay particles that are produced in a certain known volume of the beam per second. In this way, the neutron lifetime can be determined online.

Several problems and experimental challenges exist hereby:

- The decay volume has limitations as the cross section of the beam is roughly $100\,\text{cm}^2$ and for a typical flux of $10^8\,\text{cm}^{-2}\,\text{s}^{-1}$ , the rate is only one neutron decay per $\text{cm}^3$ and second.
- The number of neutrons simultaneously inside the volume has to be known accurately. Therefore, the flux of the beam has to be determined online, which is not a trivial task. Most experiments utilize the radioac-

---

[1] National Institute of Standards and Technology, Gaithersburg, Maryland.

| $\tau_n[s]$ | **Method** | **Year** | **Group** |
|---|---|---|---|
| $903 \pm 13$ | gravitational trap | 1986 | Kosvintsev |
| $\mathbf{887.6 \pm 3.0}$ | **gravitational trap** | **1989** | **Mampe** |
| $877 \pm 10$ | magnetic storage ring | 1989 | Paul |
| $\mathbf{888.4 \pm 3.1 \pm 1.1}$ | **gravitational trap** | **1992** | **Nesvizhevskii** |
| $\mathbf{882.6 \pm 2.7}$ | **gravitational trap** | **1993** | **Mampe** |
| $\mathbf{885.4 \pm 0.9 \pm 0.4}$ | **UCN double bottle** | **2000** | **Arzumanov** |
| $878.5 \pm 0.7 \pm 0.3$ | gravitational trap | 2005 | Serebrov |

Table 2.3: Results for $\tau_n$ measured with trapping experiments [Y$^+$06]. The results included in the PDG world average are printed in bold face.

tivity created by the neutrons hitting a detector behind the decay volume. Also precise knowledge of the decay volume is not easy to obtain.

- $4\pi$ solid angle collection of the charged decay products is desirable because one cannot afford to loose any of the few decay products. Magnetic fields to guide the charged decay particles ascertain this.
- If the particles reach the detector, the detection efficiency either has to be 100%, or the energy distribution of the decay particles and the energy dependence of the detector efficiency has to be known exactly; both is very hard to realize.
- The decay events must be completely separable from any background occurring. This can be done by coincidence measurement of electrons and protons, but often limits the solid angle of detection.

Due to all these challenges and the fact that this type of experiment requires absolute values of all magnitudes, the uncertainties in $\tau_n$ could not be reduced to an acceptable level. Different experiments also gave significantly different values of $\tau_n$, often not even compatible despite their large uncertainties [Byr97].

Three values measured by beam methods are included in the current world average for $\tau_n$ adopted by the Particle Data Group. A list of representative measurements is given in table 2.2.

In contrast to beam methods, neutron storage experiments rely on long observation times of less neutrons, and, up to now, a method to extrapolate to zero losses. The storage lifetime of UCN in a lossy trap.

$$\frac{1}{\tau_{st}} = \frac{1}{\tau_n} + \frac{1}{\tau_{loss}} \tag{2.3}$$

is composed of the (unknown) neutron lifetime $\tau_n$ and the so called loss lifetime $\tau_{loss}$.

All storage experiments to date had to deal with $\tau_{loss} < \infty$, mostly because of absorption or upscattering at the trap walls.[2] Hence, we can rewrite

$$\frac{1}{\tau_{loss}} = \mu(E) \cdot \gamma_w(E), \tag{2.4}$$

$\mu(E)$ being the energy dependent loss probability per wall bounce and $\gamma_w(E)$ the energy dependent wall collision frequency for UCN. One of these two values has to be extrapolated to zero to arrive at the real neutron lifetime. Representative examples for trapping experiments are listed in table 2.3.

In the two most recent material storage experiments [A+00, S+05], the volume to surface ratio $V/S$ of the trap was altered, varying $\gamma_w$ according to the approximate formula

$$\gamma_w = \frac{S \cdot \bar{v}}{4V}, \tag{2.5}$$

assuming a mean UCN velocity $\bar{v}$.

Both groups used fomblin[3] oil, Arzumanov et al. at room temperature and Serebrov et al. at 123 K. The earlier experiment [A+00] used a bath of fomblin oil and a rotating mechanism to renew the storage layer, see Fig. 2.1. The inner part of a spherical vessel or the annular gap between two nested spherical vessels could be used for storage, allowing a change of $\gamma_w$ by a factor of five without breaking the vacuum. In addition the upscattered UCN were monitored by surrounding the trap with thermal-neutron detectors.

This experiment realized a longest storage lifetime of $\tau_{st} = 780$ s; the final extrapolated neutron lifetime was $\tau_n = 885.4 \pm 0.9_{stat} \pm 0.4_{syst}$ s.

The latest experiment, called Gravitrap, was conducted using low-temperature fomblin and two storage vessels of different width to alter $\gamma_w$ by a factor of 2.5. The shape of the smaller one is indicated by the dashed line in figure 2.2. Also the storage lifetime was recorded for different slices of the UCN energy spectrum by rotating the trap only partially downward while emptying. The major improvement of this new setup was the long storage lifetime $\tau_{st} = 869 \pm 0.5$ s which then only makes an extrapolation of less then 2% necessary.

---

[2] The cross section of the rest gas in the storage volume can be neglected below a vacuum pressure of $1 \cdot 10^{-5}$mbar.

[3] PFPE, perfluoropolyether.

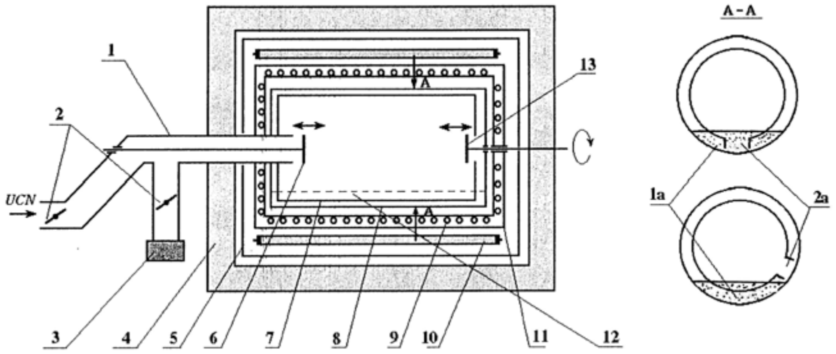

Figure 2.1: The scheme of the experimental setup of the fomblin trap at the ILL. (left side) 1: UCN guide, 2: shutters, 3: UCN detector, 4: polyethylene shielding, 5: cadmium housing, 6: entrance shutter of the inner vessel, 7: inner storage vessel, 8. outer storage vessel, 9: cooling coil, 10: thermal-neutron detector, 11: vacuum housing, 12: oil puddle, 13: entrance shutter of the gap vessel. (right side) 1a: oil puddle, 2a: slit [A$^+$00].

The final value achieved with this experiment was $\tau_n = 878.7 \pm 0.7_{\text{stat}} \pm 0.3_{\text{syst}}$ s.
This result was discussed for a long time because it did not fit to the Particle Data Group (PDG) world average, whereas the result published in Arzumanov et al. did and now dominates this world average of $\tau_n = 885.8 \pm 0.8$ s. The PDG even did not include it in its latest issue because of this discrepancy puzzle (see figure 2.3).
Major disadvantages of storage methods up-to-date are the need for extrapolation mentioned, but also the scheme of determining the storage lifetimes through consecutive fillings of the experiment, emptying after different storage times and counting the remaining UCN. If the UCN source is not completely stable over this period of time, additional uncertainties will come up.
The best solution is to combine the best of the two methods while avoiding their major drawbacks: online detection of decay particles together with the long observation time of storage experiments and simultaneously eliminating storage losses and the need to know the decay volume exactly. A concept to achieve this will be presented in the next chapters.

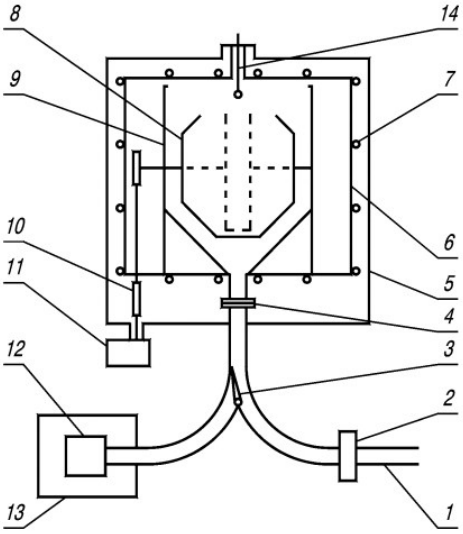

Figure 2.2: The scheme of "Gravitrap", a gravitational UCN storage system. 1: neutron guide from UCN Turbine, 2: UCN inlet valve, 3: beam distribution flap valve, 4: connection unit, 5: high vacuum volume, 6: rough vacuum volume, 7: cooling pipes, 8: UCN storage trap (narrow cylindrical trap is indicated by a dashed line), 9: cryostat, 10: mechanics for trap rotation, 11: stepping motor, 12: UCN detector, 13: detector shielding, 14: fomblin evaporator [S+05].

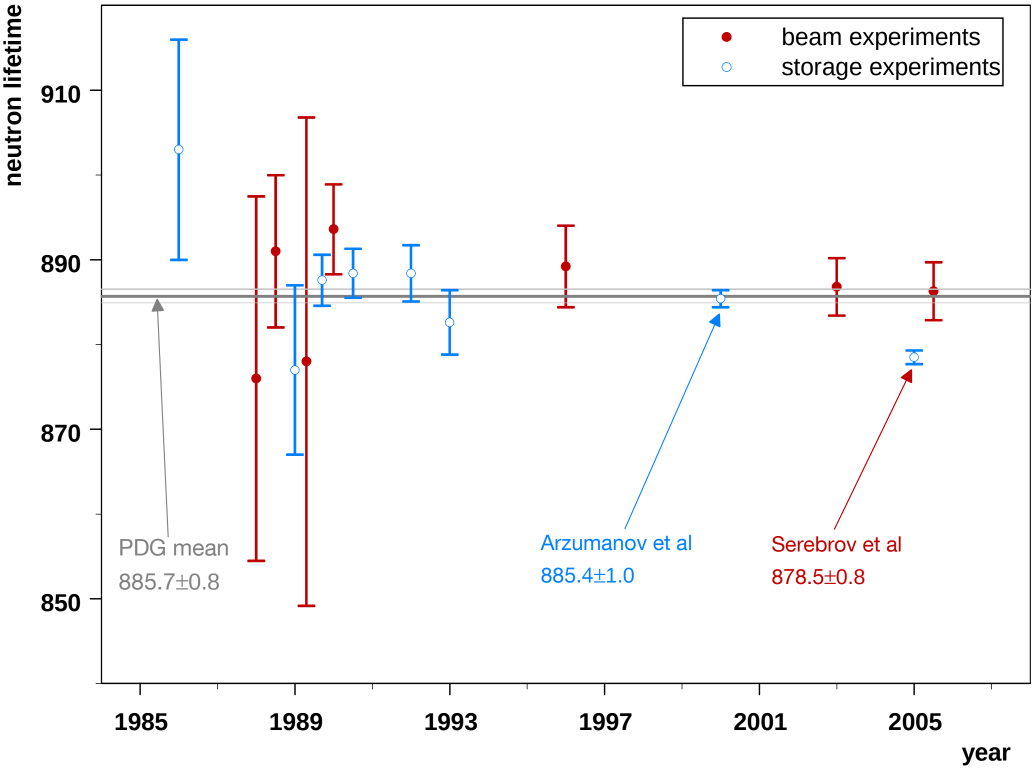

Figure 2.3: Lifetime results for the free neutron in the last 20 years.

# Chapter 3

# The Design of PENeLOPE, a Superconducting Magnetic Trapping Device for Ultra-cold Neutrons

## 3.1 The key: magnetic UCN storage

The principle of the method arises from the magnetic moment (or spin) of the neutron $\mu_\mathrm{n} = -60.3\,\mathrm{neV/T}$ and the acceleration exerted on it in an inhomogeneous magnetic field $\mathbf{B}(\mathbf{r}, t)$. Two coupled equations govern the interaction

$$\frac{\mathrm{d}^2\mathbf{r}}{\mathrm{d}t^2} = -\frac{\mu_\mathrm{n}}{m_\mathrm{n}} \nabla \left(\sigma_\mathrm{n} \cdot \mathbf{B}\right) \tag{3.1}$$

$$\frac{\mathrm{d}\sigma_\mathrm{n}}{\mathrm{d}t} = \gamma_\mathrm{n} \sigma_\mathrm{n} \times \mathbf{B}, \tag{3.2}$$

where $\gamma_\mathrm{n} = \frac{2\mu_\mathrm{n}}{\hbar} = 1.83247185(45) \times 10^8\,\mathrm{rad\,s^{-1}T^{-1}}$ and $\sigma_\mathrm{n}$ denotes the unit vector parallel to the magnetic moment of the neutron [SO01]. In the case of a constant projection of the magnetic moment onto the magnetic field, the equations of motion can be simplified to

$$\frac{\mathrm{d}^2\mathbf{r}}{\mathrm{d}t^2} = \pm \frac{\mu_\mathrm{n}}{m_\mathrm{n}} \nabla |\mathbf{B}|. \tag{3.3}$$

Hence, the neutron acceleration depends on the sign of the spin projection on the magnetic field: if the spin is aligned parallel to $\mathbf{B}$, high flux density regions repel the neutrons and they are called "low-field seekers". Correspondingly, neutrons aligned antiparallel are "high-field seekers". The potential due to the magnetic field can be expressed by

$$U_{\mathrm{B}} = \mp \mu_{\mathrm{n}} |\mathbf{B}|. \tag{3.4}$$

The latter ones are hard to store magnetically, they are attracted by regions with a high magnetic flux density. Regions of strong field, however, always have to be created by some material (coils or permanent magnets) and therefore the neutrons tend to hit these materials.

For low-field seekers, in contrast, a magnetic field of 2 T around a low field region, for example, is sufficient to store neutrons of $E_{\mathrm{kin}} \leq 120\,\mathrm{neV}$. The necessary field gradient can be created by coils using multi-polarity. A prerequisite to achieve this is a persistent alignment of the spin: considering a spinning object in a magnetic field only its projection on **B** is a good quantum number. Its value can be $m_{\mathrm{s}} = \pm 1/2$. Perpendicular to the magnetic field vector the magnetic moment has a degree of freedom, the phase angle $\phi$. So it precesses around the **B** vector with the Larmor frequency

$$\omega_{\mathrm{L}} = \frac{2\mu_{\mathrm{n}}}{\hbar} B, \tag{3.5}$$

where $B$ denotes the absolute value of the magnetic flux density. To assure that the spin will not change its orientation, any change of the magnetic field has to be adiabatic, which means "slow" enough, so that the spin can follow the field rotation. The statement

$$\omega_{\mathrm{L}} \gg \frac{\frac{\mathrm{d}\mathbf{B}}{\mathrm{dt}}}{B}, \tag{3.6}$$

(often called adiabatic condition) is fulfilled in the neutron reference frame when the Larmor precession is much faster than the field change normalized to the absolute value of the flux density. Already from this simple rule one can see, that in order to store low-field seekers in a volume surrounded by strong fields, no region of zero field should exist because in this case, equation 3.6 can never be fulfilled and spin flip may occur. Consequently, the neutron becomes a high-field seeker and will be lost.

So, if the magnetic trap is designed carefully, fulfilling the adiabatic condition for the neutron, losses may be brought down to a level that is negligible. This will allow to improve the current neutron lifetime precision significantly. The experimental proof of principle for magnetic UCN storage in larger volumes has recently been carried out [E+05].

## 3.2 The add-on: realtime $\beta$-decay proton detection

The conditions mentioned above provide a loss-less trap for ultra-cold neutrons, but there is still the problem of the measurement principle. To obtain a value for the neutron lifetime one has to fill the trap several times, wait for different storage times and count the remaining neutrons. This involves an uncertainty in the number of neutrons inside the trap at storage start, which is difficult to monitor. Moreover, emptying the trap is not an instantaneous process; in common material bottles, the emptying time constant is in the range of 10 s. To extract the neutrons from magnetic bottles, the magnetic field has to be ramped down or altered so that the UCN can exit. The time constant to be dealt with may be as long as several 100 s depending on the design if superconducting coils are utilized.

Thus, measuring the decay rate of the trapped neutrons is a much cleaner approach. Preferable particles are protons because electrons cannot be manipulated by technically-feasible electrode configurations; the voltages which can be achieved are in the range of several 10 kV compared to a few hundred keV kinetic energy of decay electrons. This, in turn, makes a $4\,\pi$ solid detection angle very difficult to achieve. Neutrinos are out of the discussion for obvious reasons.

Again, protons emerging from $\beta$ decay only have energies up to 750 eV, too low to be detected, hence they have to be post-accelerated electrostatically.

## 3.3 Gravity as a lid

Proton extraction is only possible if there is a direct line of sight into the storage volume which is not blocked by e.g. coils. This is where gravity becomes important because it serves as a natural lid of the trap: UCN kinetic energies correspond to jumping heights in the meter range. In this way, the trap can stay open (also magnetically) at the top to permit extraction.

Therefore, the goal of our design effort was a loss-less magneto-gravitational trap for ultra-cold neutrons which allows real-time extraction and detection of protons with high efficiency. The result of this effort will be presented in the next chapters.

## 3.4 The design of the magnets for PENeLOPE

The main design parameters for a magnetic trap are:

- The ratio of the lowest to the highest flux density in the storage volume $B_{\text{max}}/B_{\text{min}}$: it determines the maximum energy spread of the trapped neutrons through $E_{\text{kin,max}} = -\mu_{\text{n}}(B_{\text{max}} - B_{\text{min}})$, but must not reach infinity, as this signifies a zero-field region which will cause UCN losses as discussed above.
- The effective storage volume $V$, which is surrounded by a surface fulfilling the equation $E_{\text{kin,max}} = m_{\text{n}}gh + \mu_{\text{n}}B_{\text{max}}$. Here $h$ is the height above the bottom of the storage volume and $g$ the gravitational acceleration.
- Compliance with the adiabatic condition

$$\omega_{\text{L}} \gg \frac{\frac{\text{d}\mathbf{B}}{\text{dt}}}{B_{\text{min}}} \approx \frac{\sqrt{\frac{2E_{\text{kin,max}}}{m_{\text{n}}}} \cdot \nabla\mathbf{B}}{B_{\text{min}}}, \tag{3.7}$$

  which can be approximated by using the maximum kinetic energy of the UCN and the gradient of the magnetic field $\nabla\mathbf{B}$. If it is too big, the probability of neutron spin flip will become significant.
- The extraction efficiency $\eta_{\text{p}}$ of protons being emitted from decaying stored neutrons. It should be sufficiently large and constant over time.

The optimization process for the coils was a quite complex task: first the decision was made to use superconducting coils having an up to five times higher usable field than normal-conducting coils or permanent magnets. A multipole arrangement of solenoids in vertical direction was chosen to create large field gradients at the boundaries of a low-field region.[1] The shape of the solenoids was defined using multi-parameter non-linear optimization algorithms with the commercially available program package MagNet® along with OptiNet®.

The final result of the magnet design can be seen in figure 3.1. The main storage volume is surrounded by a set of solenoids aligned vertically with an inner radius of 0.5 m that form the outer magnetic boundary along with concentric solenoids on a horizontal plane on radii between 0.135 m and 0.475 m as bottom boundary. The nominal current densities in these coils lie in the range $317 - 370$ A/ mm$^2$. Adjacent coils always have alternating current direction, thus a magnetic field with approximately exponential decay into the storage volume is created when the coils are energized.

---

[1] This does not contradict with the adiabatic condition 3.6 as the magnitude of the flux density is very large here.

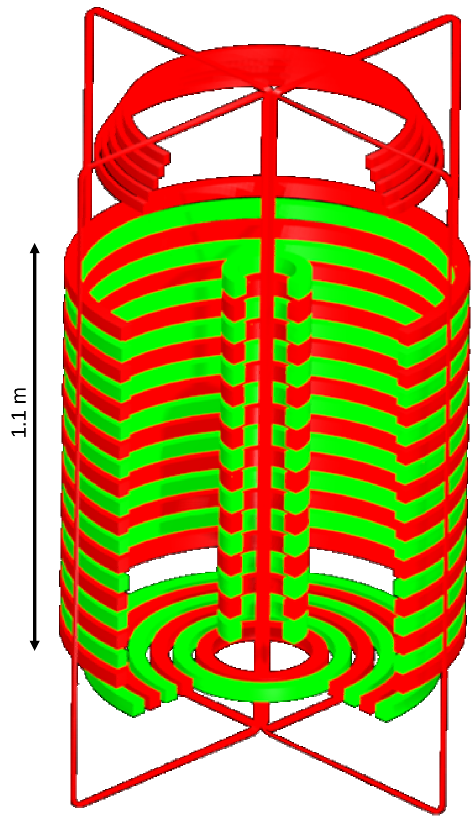

Figure 3.1: Magnet design of PENeLOPE (cut-open view): The green and red colors symbolize the alternating current direction inside the coils.

By examining the field map it becomes topologically inevitable that zero field regions in the storage volume are present. These rings are indicated in the vertical cut-away view of the magnetic flux density (Fig. 3.2). Therefore an azimuthal magnetic field component had to be created, which is achieved through four race-track coils. The importance of those coils will be shown in chapter 4 in detail. They shall be constructed to have a summed up current of around 10 kA. The current cannot be much higher because of technical feasibility. With the total current in one coil the number of windings necessary rises linearly and it is not practical to wind up to a few thousand wires interwoven with the main storage coils. Consequently the field produced by only a few windings is not strong enough to avoid collisions of UCN with the coils, so an inner array of solenoids had to be added as magnetic shield for the race-track coils. They have current densities between 256 and 315 $\mathrm{A/mm^2}$.

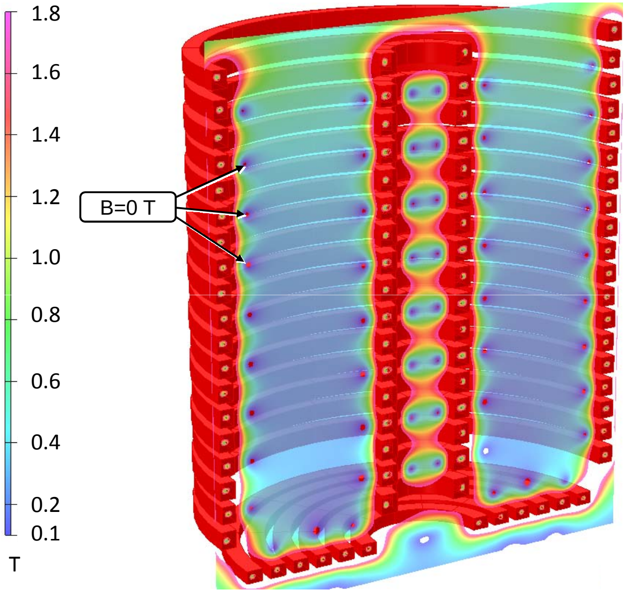

Figure 3.2: Vertical cut plot of $|B|$ in the storage volume of PENeLOPE created by the storage coils.

Figure 3.3 visualizes the sum of gravitational and magnetic potential energy: the red area, e.g., can only be reached by UCN having a kinetic energy $> 120\,\mathrm{neV}$ when entering the trap. Just for the purpose of neutron storage the magnets mentioned so far would suffice, but the proton-extraction capability is also crucial. Two measures are planned to reach this goal: firstly, every second of the inner and outer solenoids bears a slightly larger total current, which results in a net z-directed flux density in the bulk of the neutron volume. Protons emitted in this volume will follow and spiral around these field lines[2] and subsequently be guided toward the top which is open (if they are emitted into the upper hemisphere already). Secondly, a set of additional solenoids that do not have alternating current direction may be placed above the trap to focus the protons onto a smaller area, saving detector surface $S_{\mathrm{det}}$(see figure 3.4). In chapter 4 the configuration with and without focusing coils are examined further.

---

[2] The maximum gyration radius is in the range of centimeters, as the magnetic field in the bulk of the storage volume is around 0.3 T and the kinetic energy of the proton less than 10keV.

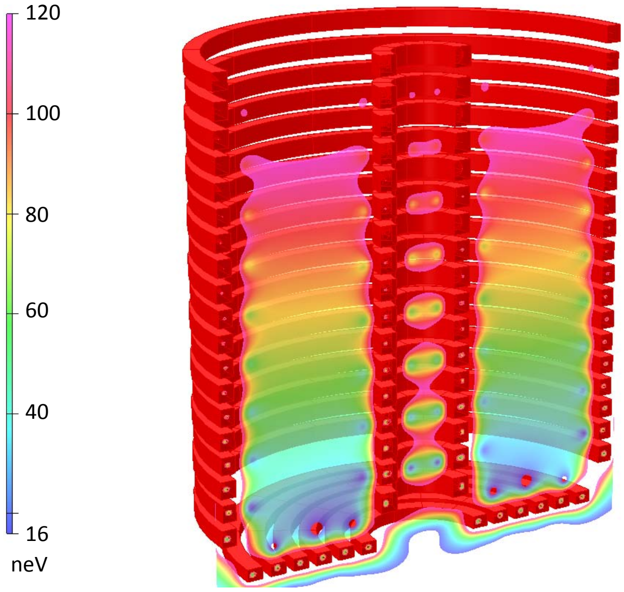

Figure 3.3: Sum of potential energy $U = m_{\mathrm{n}}gh + \mu_n B$ in the storage volume of PENeLOPE created by the storage coils.

## 3.5 High-voltage system

Just shaping the magnetic field would result in a proton collection efficiency of less than 50% because all protons emitted into the lower hemisphere would be lost. Extraction electrodes, the bottom one at ground potential and the top one at $-10\,\mathrm{kV}$, will create a fairly homogeneous electric field (cf. 4.11). This electric mirror will accelerate the protons to the top and thereby reverse the z-component of their velocity within a few centimeters for all proton energies occurring at neutron decay.

The electrodes will be located on the inner vertical surfaces of the storage volume at heights above bottle ground between 0 and 1.1 m. They could be arranged as ring electrodes, being placed in high-field regions, that the UCN cannot reach, built from a high-resistive sheet electrode or a resistor chain; they have to be covered by UCN reflecting material to assure a long storage lifetime during the phases of PENeLOPE with zero or low magnetic field.

To detect the protons efficiently, their kinetic energy should be higher than 30 keV, therefore the detector has to be set on a potential of approximately $-40\,\mathrm{kV}$.

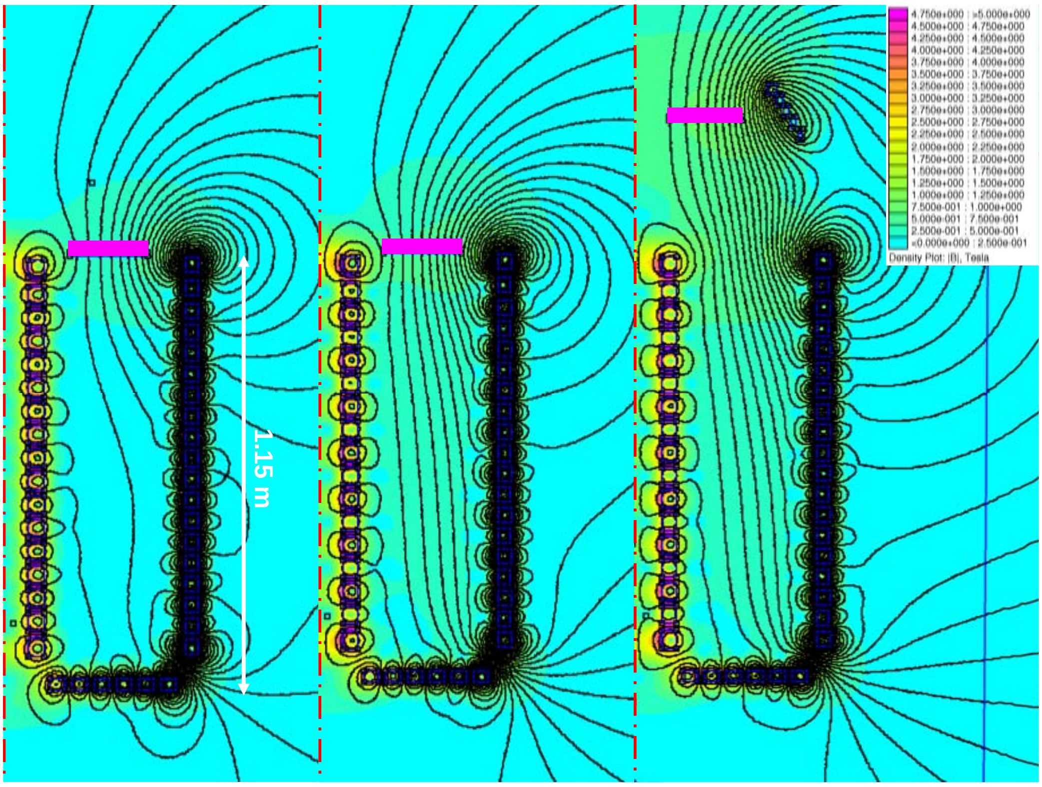

Figure 3.4: (left) Field map of coils without optimization for proton extraction; $S_{\text{det}} = 0.31\ \text{m}^2$ (middle) Additional z-directed field is added through shaping the storage coils; $S_{\text{det}} = 0.31\ \text{m}^2$ (right) Focusing coils in place; $S_{\text{det}} = 0.25\ \text{m}^2$. The rotational symmetry axes are indicated by red dashed lines, the respective proton detector position by a purple rectangle.

## 3.6 Proton detection system

The proton detector has to cover quite a large area between 2500 and 3050 cm$^2$. Moreover, the detector has to work under extreme conditions: high vacuum $p < 10^{-7}$ mbar, large magnetic field $B \approx 2\,\text{T}$ and low temperature $T \approx 30\,\text{K}$. A scheme for a large proton detector was developed at the Physics Department E18 of the Technical University Munich [M$^+$07b]: a thin layer of CsI scintillator ($\approx 1\,\mu$m) shall be evaporated onto a 3 mm thick plastic ultra-violet-transparent light guide and read out from the side. The light is transported by a 90° bend and Princeton-type optics to large-area avalanche photo diodes (LAAPD). The whole setup could look similar to figure 3.5 utilizing 36 equal trapezoidal segments. Each of them

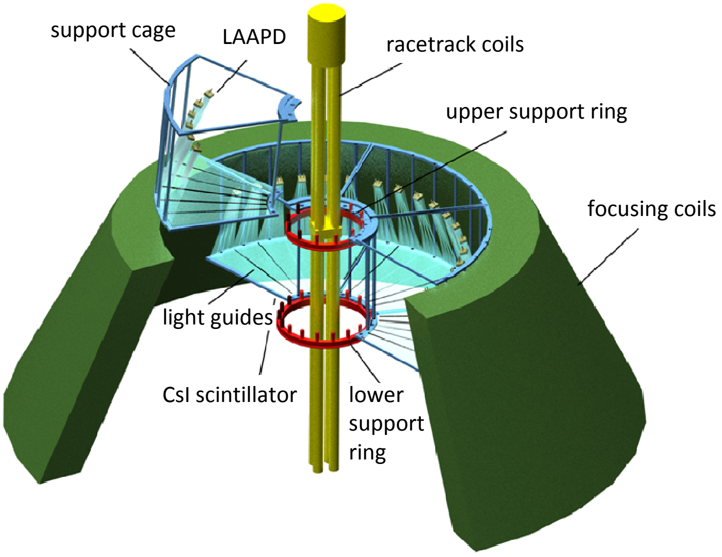

Figure 3.5: View of the proton detection scheme of PENeLOPE [Mül08].

comprises a complete and independent proton detector system with CsI scintillator, light guide and photo diode.
Characterization measurements of all detector components have been performed, now they have to be scaled up to the desired size.

## 3.7 UCN material storage capability

To fill in and extract neutrons from the trap, the magnet current has to be ramped down. According to a feasibility study, this could be achieved in less than 100 s [SM05]. Nevertheless, during this time the UCN will hit the walls and would be lost if there were no neutron reflecting surface. The best possible solution is a diamond-like carbon (DLC) coating of the trap walls; it has high Fermi potential and low absorption cross section (see table 2.1 and may also serve as extraction electrode; depending on the production process (speed of deposition, thickness, ...), a wide range of resistance values can be achieved with this material, allowing a homogeneous voltage drop from 10 kV to 0 over 1.1 m height.
Surface charge effects because of electron and proton bombardment have to be examined, however.

## 3.8 Foreseen experimental procedure

One measurement cycle of PENeLOPE could look as follows:

1. **Filling** (around 100 s):
   The experiment is open to the UCN source, the storage coils are not energized, but the racetrack coil may be at nominal current during the whole cycle. The detector opening is sealed for UCN, with which the trap is now filled.

2. **Cleaning from high-energy neutrons** (around 100 s):
   The filling opening is now closed, and the neutron energy spectrum is cut at the top by the absorber ring inside the storage volume of PENeLOPE.

3. **Ramping-up storage coil-current** (around 100 s):
   Depending on the outcome of the coil-test setup (chapter 8.2.2, the superconducting storage coils may be ramped up in around 100 s.

4. **Storage period** (between 100 s and 3000 s):
   The connection of PENeLOPE to the UCN detector is opened now to get rid of the neutrons inside the buffer volume and also detect depolarized neutrons after the first mentioned have vanished. Real-time proton detection is active. The absorber ring is protected from UCN with energies below the trap depth by the magnetic field. The storage time is also varied to determine the neutron lifetime from the UCN remaining in the trap after storage.

5. **Ramping-down storage coil-current** (around 100 s):
   The magnetic field energy is deposited into large resistor arrays to decrease the current in the storage coils.

6. **Emptying** (around 100 s):
   After the magnetic field has reached the lowest value, the remaining neutrons may be counted. The cycle is concluded by closing the detector connection and opening the connection to the UCN source.

# Chapter 4

# Physics Simulation

Before constructing PENeLOPE, it was crucial to examine as many effects and systematics of the system, that could affect the neutron lifetime measurement, as possible. To this end, a Monte Carlo code, called TRACKER, was developed to simulate the physics aspect of PENeLOPE with focus on particle tracking.

The foundations of this C++ program tracking the neutron, proton, electron[1] trajectories and neutron spin are algorithms from "Numerical Recipes" [$\mathrm{P}^{+}92$]: a 4th order Runge-Kutta or a Bulirsch-Stoer algorithm with Richardson extrapolation are used to integrate first order ordinary differential equations. The two algorithms agree within the precision long double[2] used throughout the code. For details about the equations of motion used, see [Pic04], chapter 4.

In the following chapters the general layout of the code will be explained and new features and results will be presented.

The coordinate system chosen for the computation is cylindrically symmetric with the $z$-axis concurring with the rotational axis of the storage coils: PENeLOPE is by and large cylindrically symmetric, as the storage coils are all concentric solenoids. This symmetry speeds up calculation immensely and is only broken by the four race-track coils, whose field is introduced by analytically calculating the magnetic field of the current bars of the coils. Analytical formulas are used here to calculate the magnetic flux density of the four bars outside the storage volume at $r = 0.6\,\mathrm{m}$ and in the center.[3] As the field generated by those coils is small in com-

---

[1] For references on electron see [Pic04].

[2] Long double representation of a floating-point number: 80 bits including one sign bit, 64 significant bits, 15 exponent bits resulting in 19 significant decimal places.

[3] This is only significant for spin tracking, as the field of the current bars create only very

parison with the storage coils, this does not slow down the integration too much.

## 4.1 Basic concepts of the Monte Carlo code for PENeLOPE

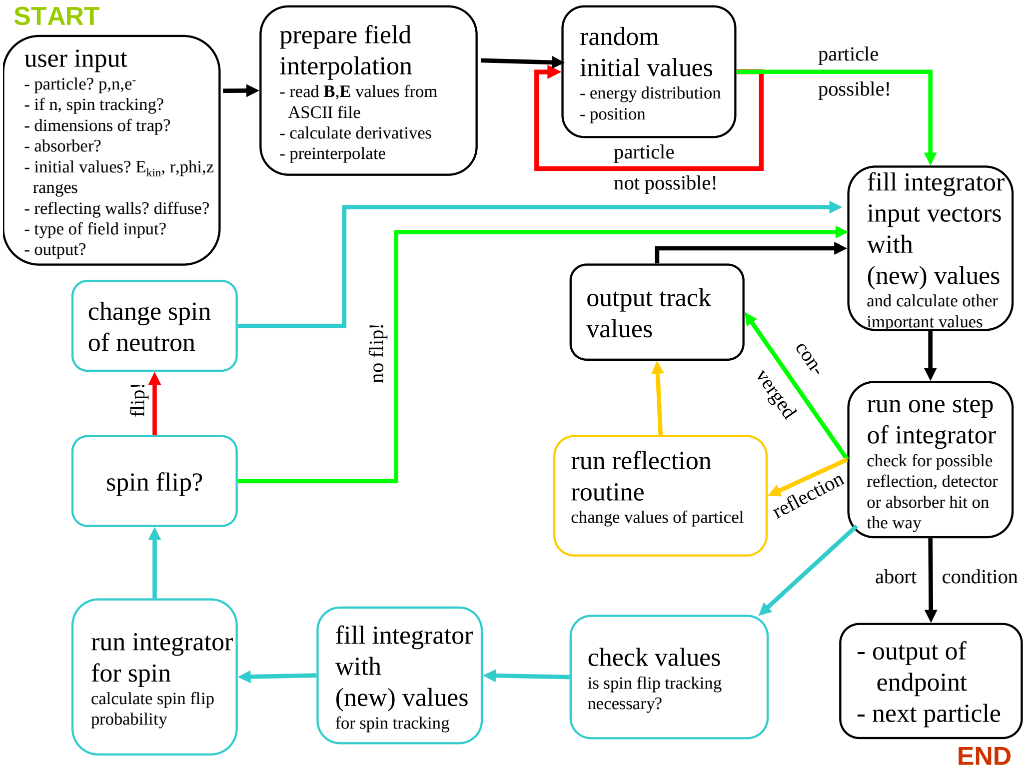

Figure 4.1: Run-time scheme of calculations and decisions in the PENeLOPE Monte Carlo code TRACKER.

As can be seen in figure 4.1, during run-time the program starts with reading in the configuration to be used for the current set of particles from `config.in`. In this file the user can specify basic parameters like the type and number of particles, if spin tracking shall be performed, or if the spatial particle distribution shall be determined and output to a file. Moreover, the type of track output to file is determined (end points and/or whole tracks and/or spin tracks) and the magnetic field input specified.

---

small field gradients, so they do not influence particle tracking.

The information about the dimensions of the trap to be simulated, the detector and absorber position is retrieved from the file `dimensions.in`, and the intervals for energy and starting positions of the particle, from `neutronen.in` or `protonen.in`.

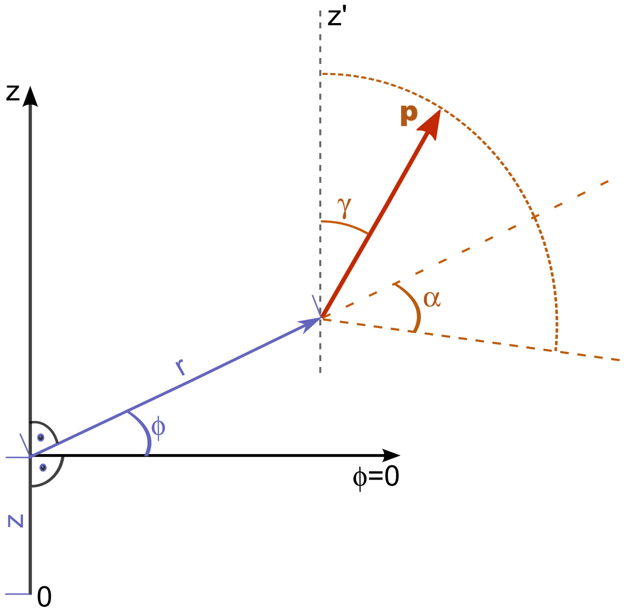

Figure 4.2: Illustration of the coordinates used for particle position and direction.

The starting position should also be given in cylindrical coordinates and the starting velocity vector is calculated from the kinetic energy and two angles: $\gamma$ is the angle between momentum and $z$ axis, $\alpha$ the angle between the projection of the velocity vector onto the $r$-$\phi$-plane and the radius vector from the $z$-axis to the particle position (see figure 4.2).
If interpolation of the magnetic and electric field from a given table file is selected, the values in `fieldval.tab` are read and the pre-interpolation is started: The derivatives and cross derivatives of the field values at each point of the table file are calculated and stored in memory (see appendix A). From this data, the coefficients necessary for a two-dimensional bicubic interpolation are computed and stored in a four-dimensional array. This speeds up the interpolation process significantly during the actual particle tracking. After that the individual particles are created using the random-number generator algorithm Mersenne Twister [MN98][4] taking

---

[4] Mersenne Twister is a 623-dimensionally equidistributed uniform pseudo-random number generator with period $2^{19937}-1$.

into account the expected energy distributions of protons, neutrons or electrons; for protons and electrons it is as shown in figure 1.2, for neutrons a Maxwellian distribution directly proportional to the starting energy is applied.

The starting values $(r, \phi, z, \dot{r}, \dot{\phi}, \dot{z}, t_{\text{start}}, t_{\text{end}})$ are then filled into an array that is handed over to the Runge-Kutta or Bulirsch-Stoer algorithm, which does the actual integration. This routine, adapted from the "Numerical Recipes" [P+92] is extended to the needs of a UCN storage experiment, for example, a check for possible reflection of the neutron at the walls is incorporated after each internal integrator step is completed. This is necessary because the step-width $t_{\text{end}} - t_{\text{start}}$ given to the integrator is too long to ensure accurate reflection at the walls. All other exit conditions are tested after the integration routine has reached the desired end time of the integration step. When one of them is given, the fate of the particle is written to file and the calculation for the next particle started or the program stopped.

Another approach had to be followed for spin tracking. The time scales of the spin and neutron-track dynamics are quite different for UCN: in a magnetic field of 1 T, the neutron spin precesses $2.9 \cdot 10^7$ times per second, but because of the low velocity of UCN, the wall-hit frequency for a trap like PENeLOPE is only around 10 per second. Different approaches by Vladimirsky [Vla61], Matora [Mat73, Brö04] and Sobolev [Sob03] (see also appendix B) were followed, but did not yield satisfying results.

The method described below produces very promising results. The two very different evolutions of particle position and spin are treated in two separate steps: for the classical motion of the UCN a constant orientation of the neutron spin towards the magnetic field is assumed, which basically assumes adiabaticity (equation 3.6) and effectively a time averaging of the real quantum mechanical state of the spin is performed. This is a good assumption for most parts of the UCN track in the trap, especially in high-field regions, where the adiabatic condition is well fulfilled. However, a small fraction of the track leads through regions of low flux density, in which we are especially interested because here a spin-flip is much more likely.

In practice, the algorithm checks if during a completed particle-tracking integration step a low-field region ($B < 0.1\,\text{T}$) is passed and invokes the spin-tracking routine if this is the case. The magnetic flux density vector is recorded during the step and used for the spin-tracking routine. Cartesian coordinates are applied instead of cylindrical coordinates because of higher calculation speed. The evolution is then determined using the Bloch equation for the spin $S$ in a magnetic field

$$\frac{\mathrm{d}\mathbf{S}}{\mathrm{dt}} = [\boldsymbol{\omega} \times \mathbf{S}] \,,$$

where $\boldsymbol{\omega}(\mathrm{t}) = -\gamma_{\mathrm{n}} \cdot \mathbf{B}(t)$ is a product of the gyro-magnetic ratio and the magnetic flux vector. $\mathbf{S}$ is a spin $1/2$ vector $|\mathbf{S}| = 1/2$. In cartesian coordinates, the cross product becomes

$$\begin{aligned} \dot{S}_{\mathrm{x}}(t) &= \omega_{\mathrm{y}} S_{\mathrm{z}} - \omega_{\mathrm{z}} S_{\mathrm{y}} \\ \dot{S}_{\mathrm{y}}(t) &= \omega_{\mathrm{z}} S_{\mathrm{x}} - \omega_{\mathrm{x}} S_{\mathrm{z}} \\ \dot{S}_{\mathrm{z}}(t) &= \omega_{\mathrm{x}} S_{\mathrm{y}} - \omega_{\mathrm{y}} S_{\mathrm{x}}. \end{aligned}$$

The same integrator routine as for position tracking is applied to this set of first order ordinary differential equations, but with a much smaller time step compared to particle tracking.[5]

Technically, the output of intermediate values of the magnetic flux density in the particle integration step is used to transform from the lab frame to the neutron reference frame: the position-dependent magnetic flux vector in cylindrical coordinates is first transformed to Cartesian coordinates and then into time-dependent ones along the neutron trajectory. As this vector is only given at discrete time values, interpolation has to be performed in between. A fourth-order polynomial interpolation algorithm is applied here [P+92]. Hence, the routine calculates the spin evolution from a point on the neutron trajectory of fairly large field through the low-field region until a high-field region is reached again; if the spin projection onto the magnetic flux vector after such a pass through a low-field region deviates from the projection before, this results in a non-zero spin-flip probability.

A fully oriented polarization vector ($S_{\mathrm{proj}} = |\mathbf{S}|$) is assumed at the start of the spin tracking; this may be explained by the fact that at reflection of the UCN on the magnetic walls, the quantum mechanical uncertainty in the spin projection is reset, because only the low-field seeker part of the neutron is reflected. The high-field seeker part is lost at the walls. Accordingly, the probability that the spin does not flip (the survival probability), computes to

$$P_{\mathrm{surv}} = \frac{1}{2}\left(\frac{\mathbf{S}\cdot\mathbf{B}}{|\mathbf{S}|\cdot|\mathbf{B}|} + 1\right). \tag{4.1}$$

The total spin-flip probability of a particle after it has passed $n$ low-field regions is then given by

$$P_{\mathrm{flip}} = 1 - \prod_{i}^{\mathrm{n}} \left(P_{\mathrm{surv}}\right)_i . \tag{4.2}$$

---

[5] Here the Runge-Kutta algorithm is preferred, as it is a more robust solver.

The assumption that the spin dynamics are separable from the particle dynamics is only valid if the probability for a spin to change its orientation is so small that it can practically be neglected. If the probability were significant, both, the low and high-field seeker tracks would have to be computed. The field configuration of PENeLOPE, however, is designed to minimize spin flips, hence $P_{\text{flip}}$ is very small (see chapter 4.4.5).
Additionally to integration of the equations of motion, a neutron reflection routine is interwoven with the integrator algorithm and called on demand when a particle is close to a wall. It provides specular and diffuse reflection and also absorption considering the respective Fermi potential of the wall material.
When one of the possible abort conditions[6] is fulfilled, tracking is stopped and the state of the particle is written to disc. Finally, a new particle is created or the program is terminated.

## 4.2 Benchmarks and precision considerations

**Proton tracking**
The program Opera[7], used to calculate static electric and magnetic fields for PENeLOPE, has also charged-particle functionality included so it can be used as a benchmark for TRACKER. It has no Monte Carlo capability, so only single trajectories could be compared; one example is visualized in figure 4.3, featuring a track reaching the detector, plotted in side and top view. The agreement is quite remarkable considering that the TRACKER result has been achieved after writing the field values of Opera to table files, interpolating them again and then solving the initial value problem numerically. Changing the integrator from Bulirsch-Stoer to Runge-Kutta produces the same results.

**Neutron tracking**
Neutron tracking poses more challenges to a simulation program as the storage times are quite long and the magnetic field distribution of PENeLOPE rather complex. Hence, most trajectories are chaotic; this may be attributed to the character of the magnetic mirror at the boundaries of the trap. In figure 4.4 on the left, two reflections at the magnetic walls with identical starting velocities and a position difference of only $|\Delta \mathbf{r}| < 10^{-8}$ m

---

[6] Abort conditions are given, when the particle is absorbed at a wall, hits a detector, reaches the filling tube or decays.

[7] Vectorfields® Opera along with the 3D magnetostatic and electrostatic solver Tosca.

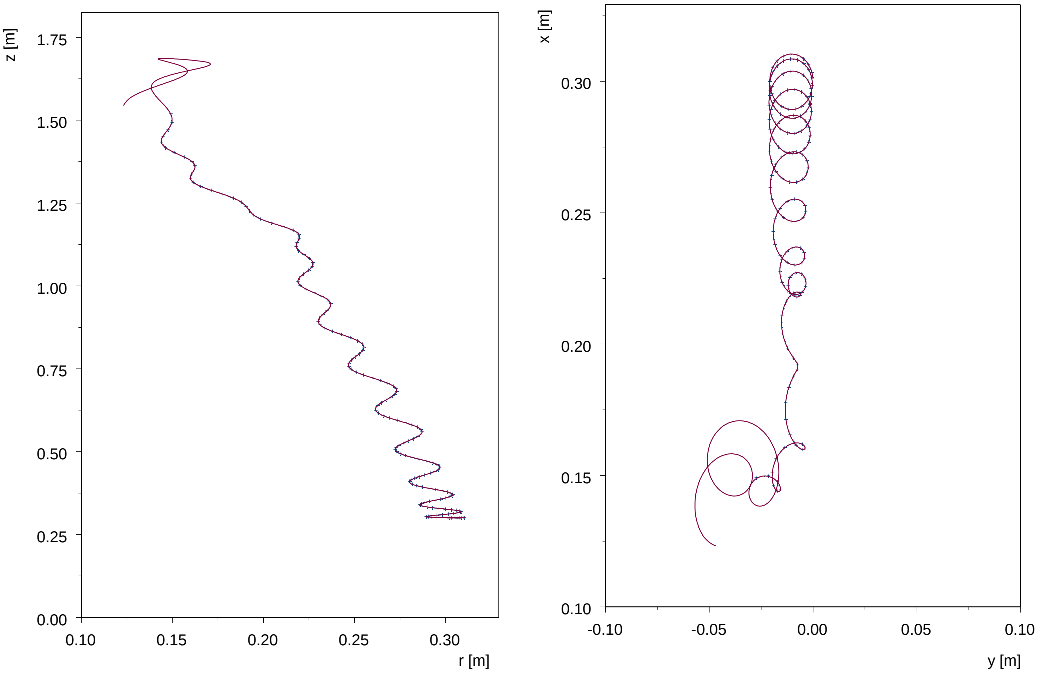

Figure 4.3: Proton-track comparison. Red line: Opera result, blue crosses: TRACKER result; (left) side view, $r$-$z$ projection; (right) top view, $x$-$y$ projection. The Opera track is a little bit longer, because the particle is not stopped when it reaches the detector volume.

are displayed. It becomes clear that the distance between tracks with slightly different initial values tends to grow exponentially. The right side shows the same tracks, only a longer section of 30 s. It should be remarked, that the envelope of the UCN trajectories on the right-hand side is identical for both cases. This dynamical instability could also originate from numerical errors adding up coherently, but figure 4.5 indicates that real physically-chaotic behavior is given. The blue curve shows the time evolution of the distances of the two trajectories of figure 4.4. The change of the energy (kinetic energy *plus* potential energy in the gravitational and magnetic field) with respect to the start energy for one track is plotted in red. Whereas the point distances grow exponentially until they reach the dimensions of the potential valley in which the UCN is confined, the difference between the current and the starting energy only grows due to the numerical uncertainties of the integration and stagnates at a low level around $10^{-7}$ neV.

Remarkably, not the whole phase space for the UCN shows these insta-

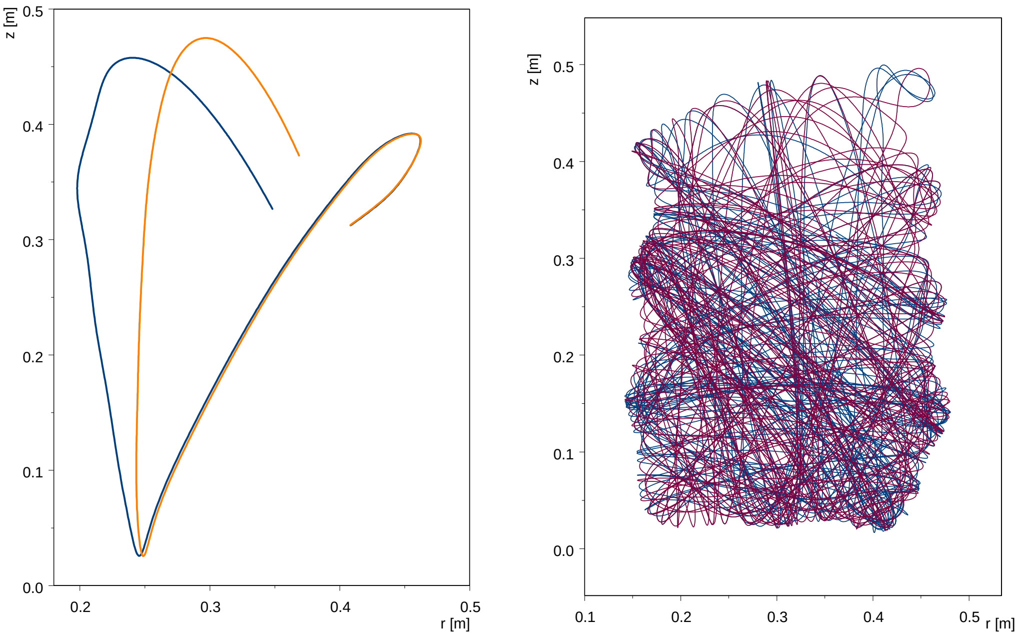

Figure 4.4: Chaotic UCN trajectories. (left) visualization of the fast separation of tracks with almost equal initial conditions (0.7 s of the trajectory are plotted); (right) 30 s of the two trajectories, the only difference in the initial values was $\Delta z = 10^{-17}$ m.

bilities. Figure 4.6 shows three different tracks in a case where the angular momentum of the neutron is comparably large, which leads to larger reflection radii. The two trajectories integrated with Bulirsch-Stoer and Runge-Kutta integration, but identical initial conditions show a deviation $|\Delta\mathbf{r}| < 10^{-7}$ m after 30 s. If the initial $z$ value is reduced by around $10^{-5}$ m, the distance to the original trajectory is still less than $10^{-3}$ m, hence not growing exponentially. If the difference of the initial values is only half of that, the trajectory distances also get cut in half, which is a very strong indication for a deterministic motion.

Summarizing these results, one may state the UCN trajectories in a magnetic field shaped as in PENeLOPE with high multi polarity undergo dynamical instabilities. Hence, it cannot be calculated deterministically when an individual neutron will be at a certain point in space, in fact the results should rather be considered as statistical probabilities. This is not in contradiction to the Monte Carlo idea as long as thousands of trajectories are calculated.

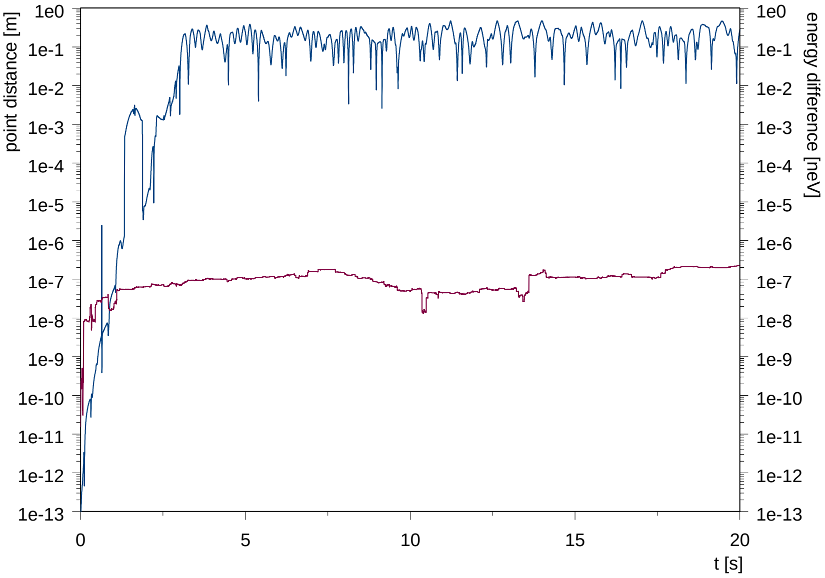

Figure 4.5: Time evolution of the distances of the trajectories shown above (blue) and energy deviation of one trajectory from the starting value (red).

**Spin tracking**

In neutron physics, spin tracking is most important for spin echo experiments, where a cold neutron beam is used to measure inelastic scattering processes with extremely high-precision [M+03]: the longitudinally polarized spins in the beam are first flipped perpendicularly to the magnetic field by a $\pi/2$ flipper and free precession starts in a magnetic holding field. In the center of the spin echo machine a $\pi$ flipper rotates the precession plane by 180°, which essentially reverses the spin precession. Then the neutron is scattered of a sample and the spin is rotated back up by another $\pi/2$ flipper. If the scattering on the sample is elastic, the total precision angle of the neutron is zero, if not, the scattering function of the probe can be determined.

To test the spin tracking part of TRACKER, the spin flippers used for the spin echo technique may serve as a benchmark; two types of spin-flippers, where the resulting polarization can be analytically deduced will be simulated: a spin-flipper coil and a radio-frequency flipper.

The radio frequency flipper ideally generates a magnetic field rotating

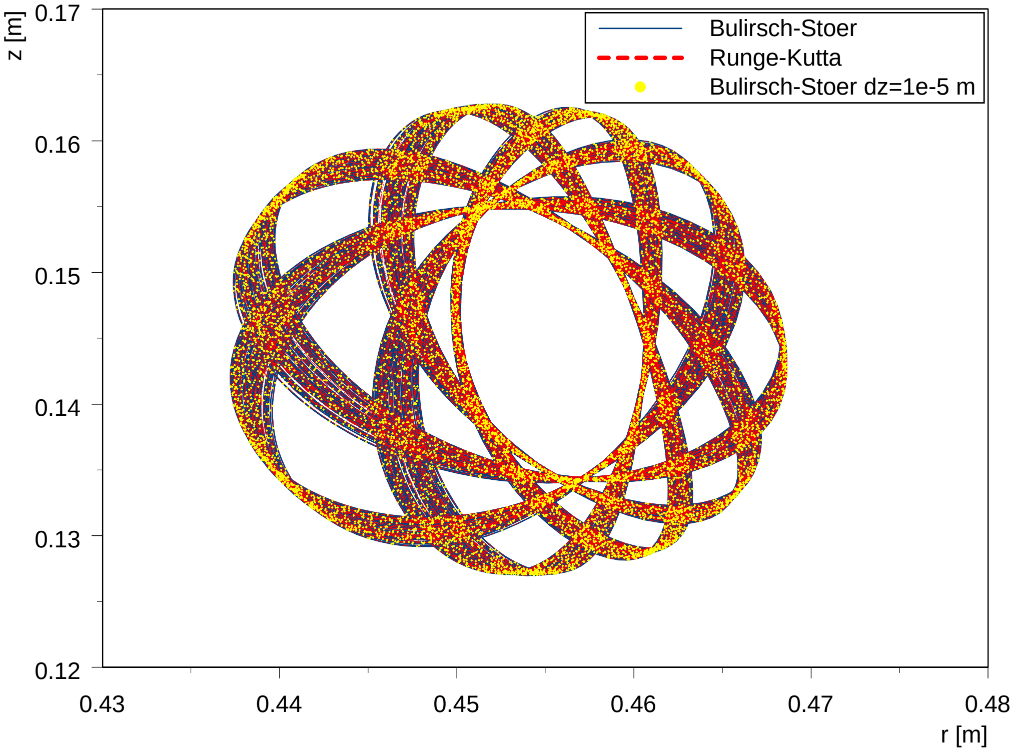

Figure 4.6: Example of a stable UCN trajectory: (blue curve) $r$-$z$ projection of a UCN trajectory with high angular momentum calculated with Bulirsch-Stoer algorithm - (light-red line) the same track calculated using Runge-Kutta algorithm - (yellow dots) starting $z$ position $10^{-5}$ m lower.

with the same frequency as the neutron spin in the holding field $B_0$

$$\mathbf{B}(t) = \begin{pmatrix} B_1 \cos(\omega t) \\ B_1 \sin(\omega t) \\ B_0 \end{pmatrix}, \tag{4.3}$$

where $\omega = -\gamma_n B_0$. In the rotating frame coincident with the precessing spin, the neutron spin experiences a constant magnetic field and so it is rotated with the frequency $\omega_1 = -\gamma_n B_1$ around this field. By applying the field $B_1$ long enough, the polarization can be rotated by any angle desirable. Figure 4.7 shows an example calculated with the spin-tracking algorithm of TRACKER: a $\pi/2$ flip is induced by a field shaped as in equation 4.3 starting with polarization in $z$ direction, ending transversally polarized as expected.

A second way to change the polarization direction of neutrons is through

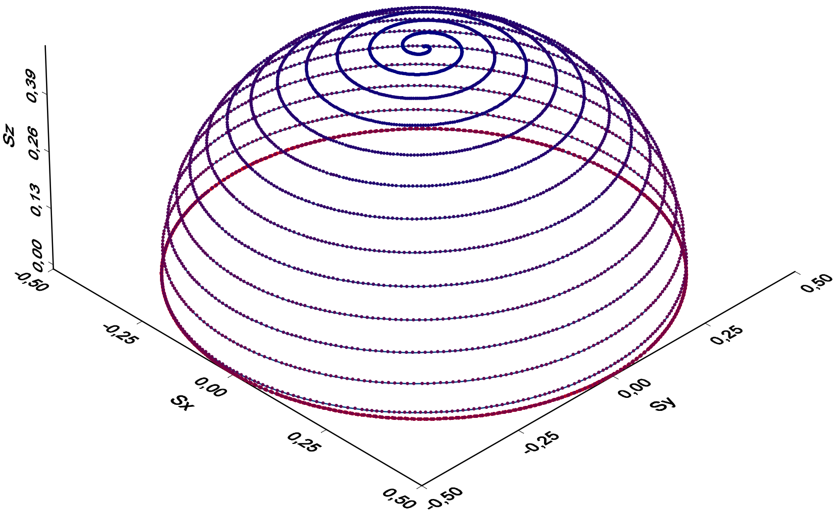

Figure 4.7: Simulation of an RF $\pi/2$ spin flipper. The tip of the polarization vector is plotted, the color code changes from blue to red with simulation time.

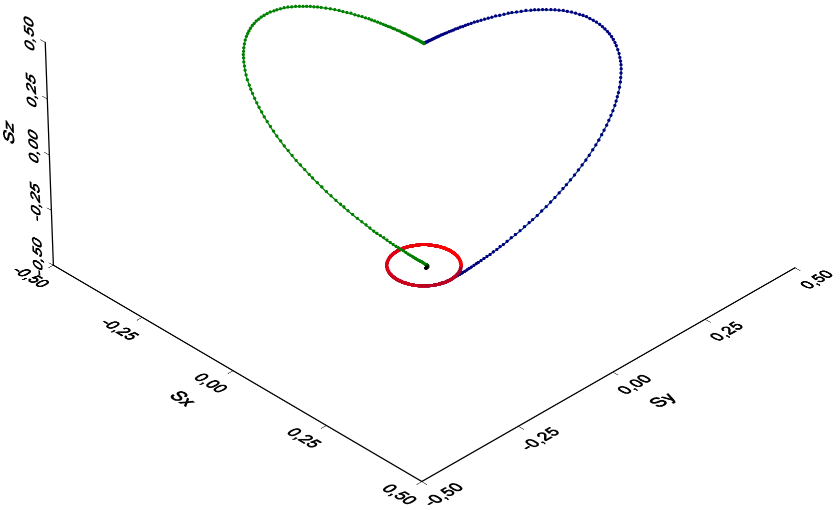

Figure 4.8: Simulation of a magnetostatic $\pi$ spin flipper, the tip of the polarization vector is plotted for two cases; in case A the color code changes from blue to red with simulation time, case B is displayed in green.

static spin-flip coils, again applying a field perpendicular to the holding field $B_0$. The field integral along the neutron track in this case has to fulfill

$$\int B_1(t)dt = 2\pi \frac{1}{n} \gamma_\mathrm{n}. \tag{4.4}$$

$n$ has to be two or four, to arrive at $\pi$ or $\pi/2$ spin rotation, respectively.

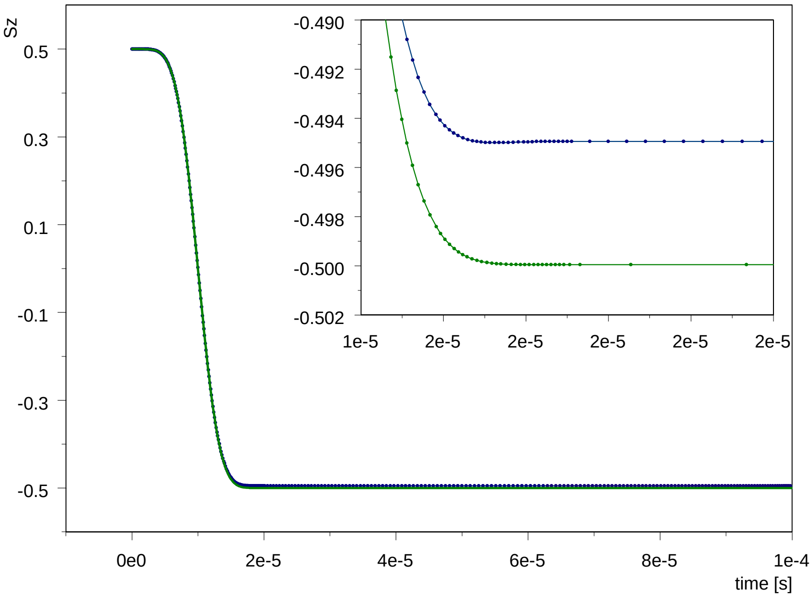

Figure 4.9: Simulation of an RF $\pi$ spin flipper, the $z$ component of the polarization vector is plotted in blue for case A and green for case B.

An important effect of this method is visualized in figures 4.8 and 4.9: A $\pi$ spin flip is simulated using the time dependent flipping field

$$B_1(t) = \begin{cases} \dfrac{\pi}{\gamma_\mathrm{n} t_1} \left(1 + \sin\left(\dfrac{2\pi t}{t_1} - \dfrac{\pi}{2}\right)\right) & \forall\, t \leq t_1 \\ 0 & \forall\, t > t_1 \end{cases}$$

and a duration $t_1 = 2 \cdot 10^{-5}$ s which fulfills equation 4.4 with $n = 2$. A complete 180° flip, however, is only achieved if $\omega_1 \gg \omega_0$ during the flipping phase. In other words, the rotation due to the holding field $\omega_0$ has to be negligible during the rotation of the flipping field $\omega_1$. If this is not the case, the spin vector will undergo significant rotation around the $z$-axis and the field integral has to be increased to achieve a complete $\pi$ or $\pi/2$ spin rotation. The figures show two cases A and B with holding fields

$B_{0\mathrm{A}} = 10^{-4}\,\mathrm{T}$ and $B_{0\mathrm{B}} = 10^{-5}\,\mathrm{T}$, respectively: in case A, the $z$ component of the polarization vector only reaches $S_z = -0.49494$ because the vector rotates 21° around the $z$-axis during the flipping process. This can be interpreted as a depolarization of the beam after the flipper of around $5 \cdot 10^{-3}$. A rotation around the $z$-axis of 2.1° in case B leads to a depolarization of only $5 \cdot 10^{-5}$.
These examples show that TRACKER reproduces common spin-flip techniques accurately.

## 4.3 Refinements and extensions of the code

The physics simulations from [Pic04] were repeated, because some algorithms were smoothed and significant extensions added to the program. Besides debugging and a change in the magnetic field interpolation routine (cf. appendix A), the geometry of the trap was adapted to the outcome of a cryostat design study (see section 8.2.1). The layout of the storage volume and the boundaries of the proton detector space were changed accordingly and the code was extended to include a buffer volume below the storage space, a UCN filling tube and the detector opening. In this way, UCN filling and detection efficiencies may be analyzed more realistically. The new geometry is illustrated in figure 4.10, a scatter plot of UCN reflections without magnetic field. In the region on the left-hand side where only a few reflection took place, the absorber ring is placed. On the right-hand side one can also see some reflections, where the racetrack coils traverse the filling channel within its vacuum housing at angles $\phi = 0°, 90°, 180°$ and $270°$.
The realistic model of the helium cryostat of PENeLOPE was also used to create new maps of the electric and magnetic fields with the finite-element program Opera. The electrodes are realized as sheets reaching from 0.06 m to 1.3 m above the bottom storage coils, with a linear voltage drop $V(z) = -8064.5\ \mathrm{V/\ m} \cdot z$ (see figure 4.11). The detector was set on $-40\,\mathrm{kV}$, every other surface grounded.

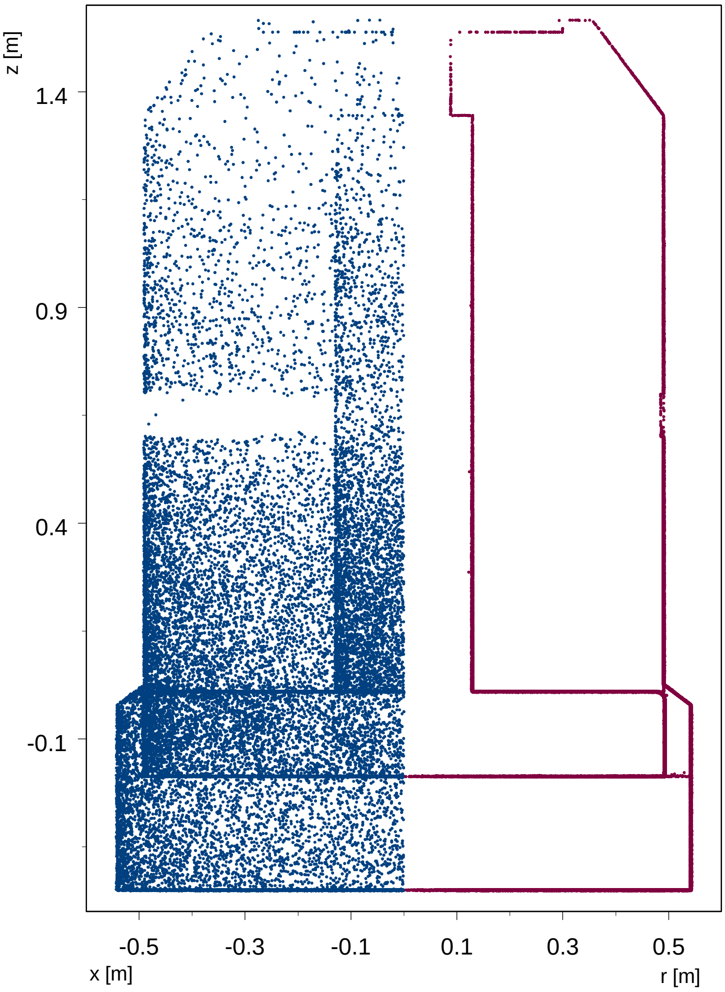

Figure 4.10: Geometry implemented in Tracker, visualized by the scatter plot of UCN reflections in PENeLOPE. Left side: projection onto $x-z$ plane, right side: $r$ and $z$ components in cylindrical coordinate system. The probability for diffuse reflection was set to 16%.

## 4.4 Updated results of the Monte Carlo simulations

### 4.4.1 Magnetic storage

The optimized coil structure of PENeLOPE allows to store neutrons with energies below 107.8 neV magnetically, all neutrons with higher energies will undergo material reflections and therefore losses may occur (see fig-

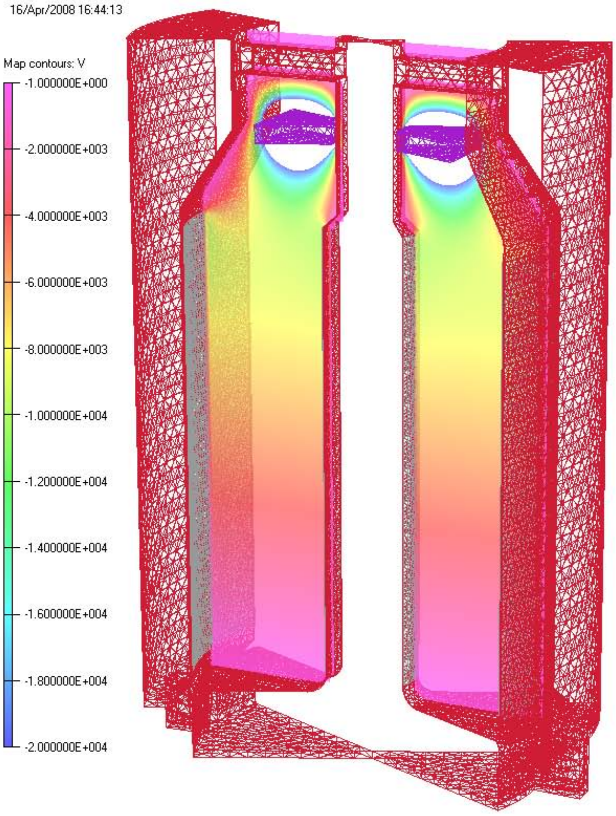

Figure 4.11: Electric potential inside PENeLOPE. Red framework: helium cryostat, purple framework: proton detector, gray framework: electrode sheet. The potential is only displayed in the magnetic storage volume in the interval $[-1\ \mathrm{V}, -20000\ \mathrm{V}]$.

ure 4.12). But even for energies up to 120 neV, out of $10^4$ simulated UCN none was statistically absorbed at the walls.

### 4.4.2 Extraction and detection of stored UCN:

Through the exit slit at the outside bottom corner of the storage volume, the UCN reach the buffer volume. In the simulation, a neutron is counted as detected when it hits a horizontal circular area of 60 mm radius at the bottom around the point $(0.45\,\mathrm{m}, 0, -0.45\,\mathrm{m})$. In the real experiment, a vertical tube might guide the UCN down to a standard $^3$He detector. Losses of this vertical tube are not taken into account in the simulation, but these should be very small.

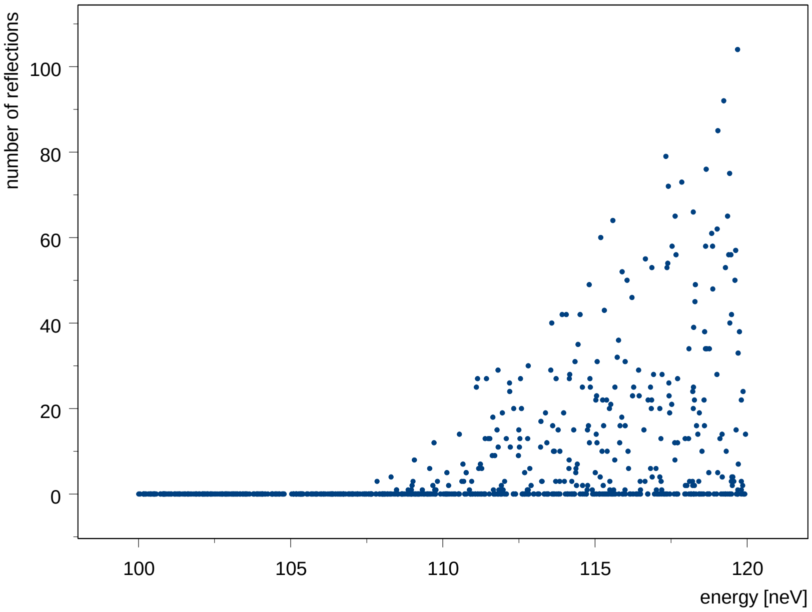

Figure 4.12: Number of wall reflections versus UCN energy for 1500 s storage time in the magnetic trapping field of PENeLOPE.

Figure 4.13 shows the time evolution of UCN that were generated with energies in the interval [16 neV, 110 neV] at the beginning of the ramp-down phase of the PENeLOPE coils. The lowest energies are not zero, because the combined gravitational and magnetic potentials are larger than zero everywhere in the trap. The histogram is broken down into "loss" channels: the $\beta$ decay in red starts right at the beginning of the simulation; all other losses only come up as soon as the magnetic field is weak enough for wall collision to happen. In the vicinity of the emptying slit, the flux density is relatively low ($\approx$ 1.8 T at full current), therefore UCN can reach the buffer volume and, hence, the detector after 50 s already, when the coils are at half nominal current. To reach the absorber, the coils have to be further ramped down, because it is situated at an elevation of 0.6 m above the trap bottom and protected by the magnetic field, so the first UCN are absorbed here after 60 s (yellow histogram). The first statistical wall losses (white) set in with UCN detection (blue), as in the buffer volume only material storage is realized.

All in all, around 76% of the stored neutrons can be collected and detected within 150 s after the coils of PENeLOPE have been ramped down.

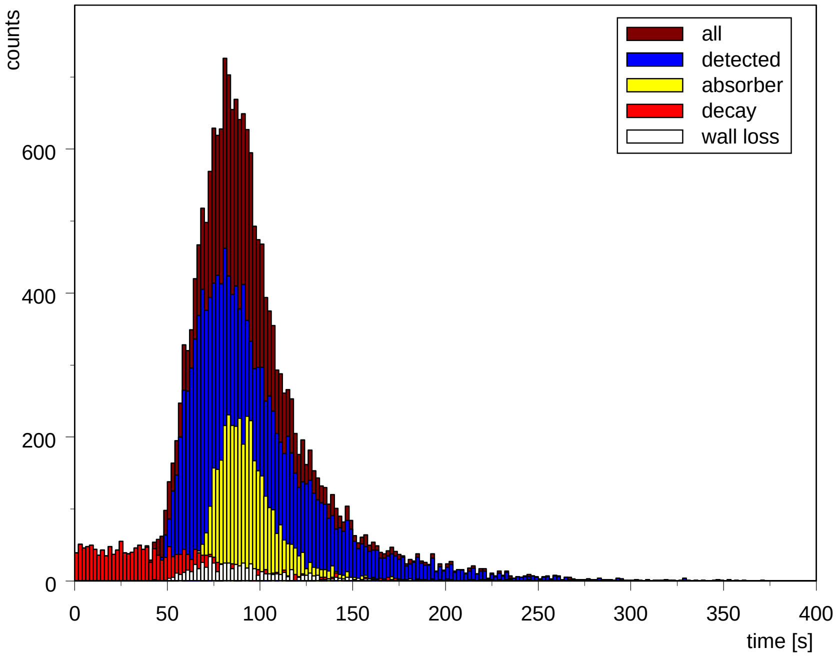

Figure 4.13: Emptying histogram of magnetically stored UCN, broken down into loss channels. Ramp-down phase: $[0, 100\,\mathrm{s}]$.

### 4.4.3 Detection of depolarized neutrons

If the orientation of the spin of a low-field seeker towards the magnetic field is reversed, the emerging high-field seeker will be attracted to large flux-density regions, hence it will have high velocities perpendicular to the walls of the storage volume and therefore a high probability of being absorbed. Accordingly, the storage lifetime is quite short as shown in figure 4.14; if the storage volume is only covered with stainless steel, most of the UCN are absorbed directly at the walls and the storage lifetime is as short as $\tau_{\mathrm{st,SS}} = 1.11 \pm 0.02\,\mathrm{s}$. When using diamond-like carbon[8] with a larger Fermi potential $V_{\mathrm{F}}$ (cf. table 2.1), the absorber accounts for a majority of the losses and the storage lifetime increases to $\tau_{\mathrm{st,DLC}} = 3.66 \pm 0.06\,\mathrm{s}$. Despite these short times, UCN can find their way through the exit slit and be detected in the UCN detector. Unfortunately, the relatively high percentage in [Pic04] cannot be confirmed with the more realistic geometric model: this is mainly because the 100 mm absorber ring at a height of 0.6 m has not been included yet; it is responsible for 75% of the losses

---

[8] In the simulation, the storage volume bottom was covered with DLC and the storage walls up to a height of 1.35 m.

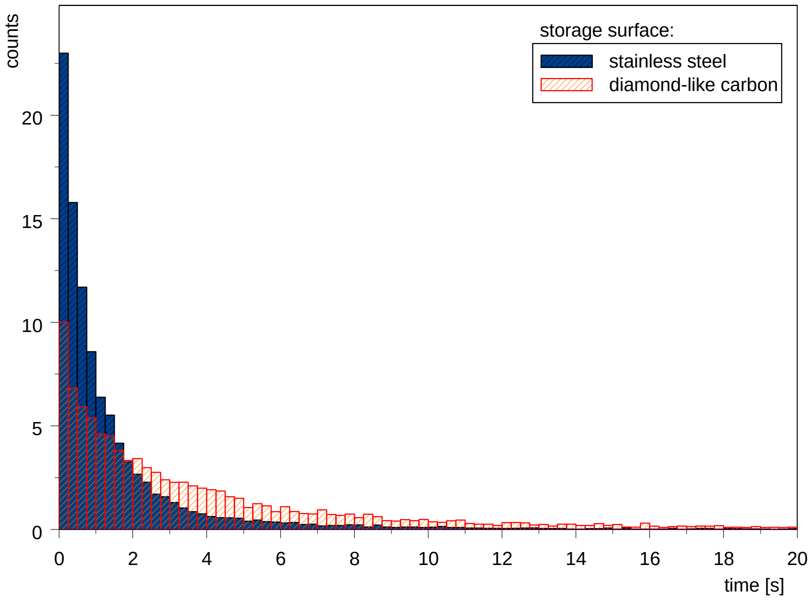

Figure 4.14: Storage lifetime distribution of high-field seekers.

with a DLC coated storage volume (15% for stainless steel). This, together with a more realistic modeling of the emptying slit, results in 5.9% of the high-field seekers reaching the detector with DLC and only 1.8% without. Extraction times here are around $12 \pm 1$ s (DLC) and $7 \pm 1$ s.

Assuming the numbers presented later in this work[9], during one cycle we should still be able to collect around 150 spin-flipped neutrons.

Another point worth mentioning is, that the wall losses mainly occur in the storage volume, absorption in the buffer volume is nearly negligible. The reason lies in the magnetic flux density at the walls of the storage volume: it is between 1 T and 2 T, whereas the buffer volume walls are further away from the coils with flux densities below 0.1 T. Therefore the mean velocity perpendicular to the walls in the latter case is not nearly as high, despite sitting lower in the gravitation potential. This means lining the buffer volume with DLC would not yield much benefit.

---

[9] The values are: Number of UCN per filling for the PSI UCN source $1.5 \cdot 10^8$, storage time 1500 s and spin-flip loss time $7.5 \cdot 10^7$ s.

### 4.4.4 Proton collection and detection

The proton energy spectrum for the Monte Carlo runs with protons is derived from the theoretical neutron decay spectrum [Nac68] using the current PDG average for the electron-antineutrino correlation coefficient $a$ [Y+06]. The starting points for the protons in the magnetic trap of PENeLOPE are determined by convolution of the Maxwellian neutron spectrum and the distribution function of UCN in the field configuration during storage. Two configurations were examined; one with (version A) and one without the focusing coils (version B). The detector size and position were adjusted accordingly: it is situated at a height of 1.5375 m with inner and outer radii of 0.1 and 0.3 m, respectively, for version A and at a height of 1.15 m with radial dimensions between 0.18 and 0.36 m for version B.

The plot of the $r$ and $z$ starting points of protons in figure 4.15 shows the positions from which protons have to start to be detected. For version A,

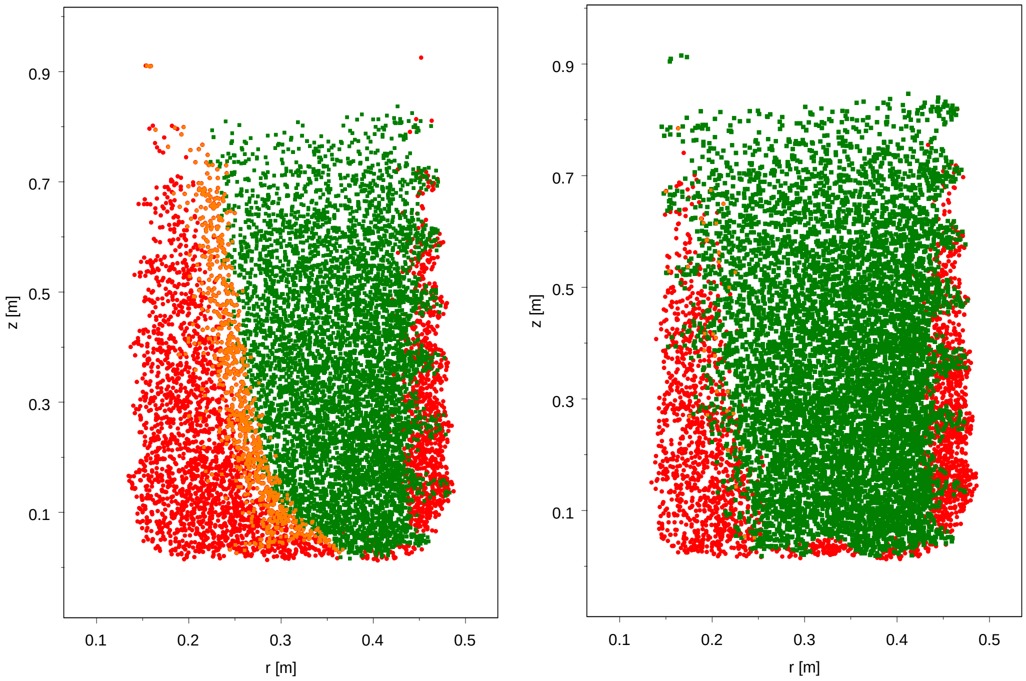

Figure 4.15: Starting points of protons color coded; left: Version A, right Version B; red circles - protons were lost - green rectangles: protons reached detector - orange dots: protons that could reach the detector after a small cryostat optimization for version A.

the collection efficiency of protons emerging from decay of UCN stored in the trap is around 62 %. Additional $6-8\,\%$ protons may be guided towards the detector, if the inner cylinder of the helium cryostat would become narrow above 1.15 m, and not 1.3 m, as it is foreseen in the current design (cf. figure 4.10). The relevant UCN are marked as orange dots in figure 4.15. This would bring the efficiency up to 70 % for version A, version B already has a collection efficiency of 76 %.

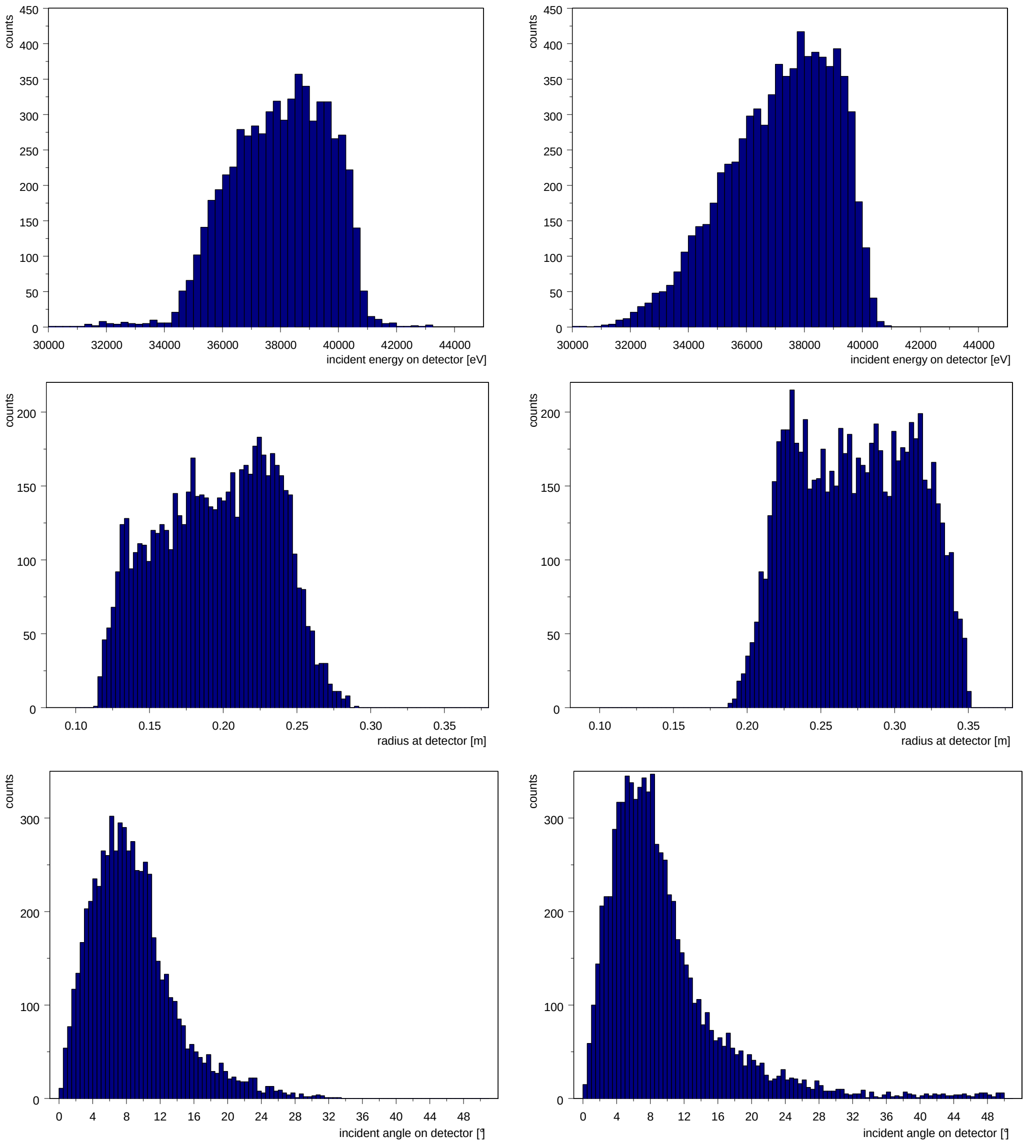

Figure 4.16: Proton energy, radius and incident-angle distribution on detector; (left) version A with focusing coils, (right) version B without.

The energy, radius and incident-angle[10] distribution of protons reaching the detector may be seen in figure 4.16. From these histograms it can be inferred, that the energy of the protons to be detected are within the interval [30 keV, 40 keV], the detector positions and sizes as described above are sufficient to collect all relevant protons, and the angles of incidence are all below 40° in version A, without the focusing coils some have larger angles.

Comparing the results for the two different configurations, it seems the decision to use focusing coils should be reevaluated; with only 20 % more detector surface, the collection efficiency would be increased by at least 6 % and five superconducting coils could be saved. Moreover, access to the UCN storage volume will be much easier because one could afford a larger opening at the top of the cryostat. What has to be pondered, are the cost reduction through needing less coils and a simpler cryostat on the one hand and the additional cost of a larger detector and more LAAPDs on the other.

### 4.4.5 Prediction of the spin-flip probability during storage

The spin tracking routine needs a lot of computation time: tracking one neutron over a typical storage time of 1500 s including spin evolution, as described in section 4.1, takes around ten days of CPU time on one processor of the node in the computing cluster at the institute E18 of the Physics Department of Technical University Munich.[11] On all 16 nodes this results in around 1.5 neutrons per day, hence, it is not possible to collect sufficient statistics. Consequently, after 5 s neutron lifetime the calculation is stopped and the spin-flip probability derived. From this, the spin-flip loss lifetime may be calculated; figure 4.17 shows the results of a variation in the current through the spin-flip suppression coils.

As expected, the loss lifetime depends on this current: above around 50 % of the nominal current of 9 kA the lifetime is larger than $10^{10}$ s for all simulated UCN, below this value some UCN have a significantly shorter spin-flip lifetime. The azimuthal field generated by the racetrack coils fills up the zero field regions, so that the Larmor precession in these volumes is sped up and the polarization vector able to follow the rotation of the magnetic field. The remnant spin flip probability with large current through the racetrack coils may be attributed to the error accumulated because of

---

[10] The incident angle is defined as the angle between the velocity vector and the perpendicular of the surface.

[11] Configuration of the nodes: dual AMD Opteron™, 1.4 GHz, 2 GB RAM.

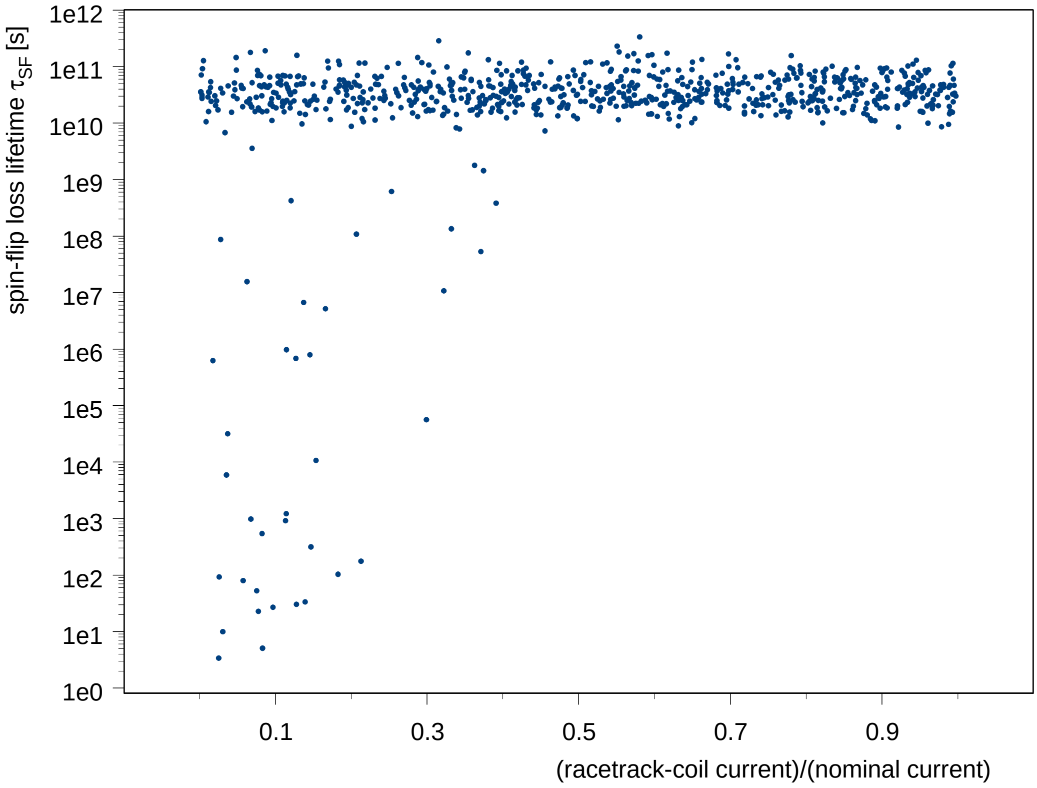

Figure 4.17: Spin-flip loss lifetime of high-field seekers simulated in the magnetic trap PENeLOPE, nominal current 9 kA.

the limited numerical precision of long double representation.
For the aspired precision of 0.1 s, the spin-flip loss lifetime has to be longer than $10^7$ s, which is obviously fulfilled.

# Chapter 5

# Marginally Trapped Neutrons and AbEx

## 5.1 Removal of marginally trapped UCN

In order to reach a high-precision in the neutron lifetime value, systematic effects have to be avoided or known very well. Besides spin-flip, another important source of possible systematic errors are so-called marginally trapped neutrons. These are UCN that have energies above the trapping threshold (110 neV for PENeLOPE), but still a storage lifetime in the trap of the same order of magnitude as the neutron lifetime. This causes a false effect on the neutron lifetime, as $\tau_{\mathrm{loss}}$ is, on average, less than infinity.

In figure 5.1 the energy dependent storage lifetimes for starting energies within $[110\,\mathrm{neV}, 200\,\mathrm{neV}]$ are shown. Around $10^4$ UCN were simulated, starting at the beginning of the magnetic storage phase of PENeLOPE. The loss times, are histogrammed separately for every bin of 10 neV width and an exponential fit performed to arrive at the storage lifetime. From values close to the $\beta$-decay lifetime for energies below 130 neV, the storage lifetime decreases significantly above 150 neV and for higher energies it is lower than 40 s. It is clear from figure 5.1 that UCN only slightly above the magnetic trapping contribute the biggest effect. The influence of UCN above 150 neV can be avoided by introducing another cleaning phase at the beginning of magnetic storage before starting proton detection.

Thus, it is crucial to get rid of the neutrons with energies slightly higher than 110 neV before the magnetic storage period starts. In former UCN trapping experiments without proton extraction, the top was accessible because of gravitational confinement and a material, which absorbs UCN or scatters them to higher energies, was brought in from the top. Only

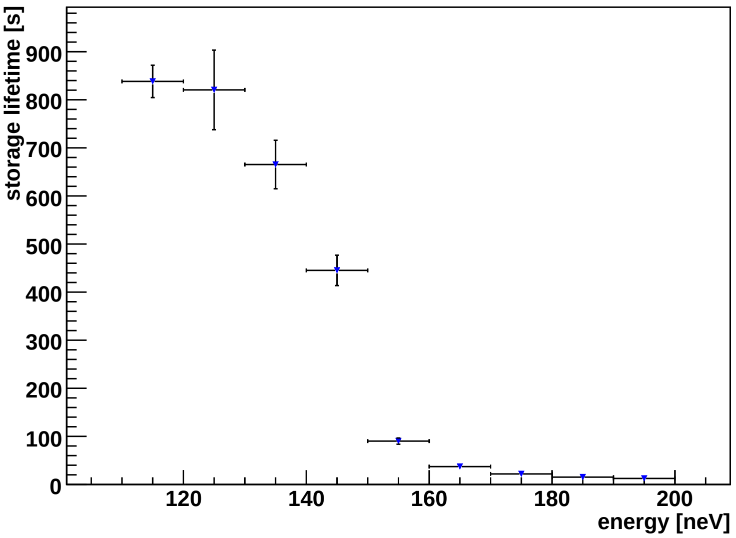

Figure 5.1: Energy dependent storage lifetimes for UCN in PENeLOPE. The horizontal error bars indicate the bin width of 10 neV.

absorption leads to immediate loss of the free neutron, but the result of upscattering is quite similar: the energy transfer to the neutron is usually much larger than the trapping potentials of the storage vessel, therefore in the next collision with the trap walls, the UCN is very likely absorbed. To enhance the penetration probability the absorber structure was sometimes even rotated [B+00]; this increases the relative velocity between UCN and absorber and thereby reduces the reflection probability at the vacuum-absorber boundary.[1]

Both is not possible in our case; as we have to keep the top of the trap open to allow proton extraction, the absorber has to be placed at the trap side-walls; this, in turn, makes rotating almost impossible because it takes place close to the superconducting coils at liquid helium temperature. Hence, a ring shaped absorber of about 10 cm height is chosen, placed at the outer walls of the storage volume. The resulting absorber surface adds up to 0.3 $m^2$.

---

[1] For simplicity, absorbing and upscattering materials are referred to as absorbers, only addressing the differences where necessary.

The details mentioned above brought up several unknowns that had to be clarified before PENeLOPE starts measuring:

1. **Efficiency of the chosen geometry:** Monte Carlo simulations give hints on the number of UCN collisions with the absorber, but only for ideal conditions.
2. **Choice of absorber material:** There are several possible solutions including titanium, polyethylene or a multilayer structure.[2]
3. **Absorber behavior down to liquid helium temperature:** Upscattering cross sections are temperature dependent, which could deteriorate the efficiency of the absorber. Also, at very low temperatures rest gas particles are adsorbed on the absorber surface. This may lead to an increased reflection probability for UCN and increase the cleaning time.

## 5.2 Ramp heating

Ramping up the magnet after filling in the neutrons in the trap causes a space compression for the UCN, because the volume accessible to the neutrons gets (depending on their kinetic energy) smaller (see [Pic04], p. 89). Following Liouville's theorem of constant phase-space density, this is compensated by increasing the mean absolute momentum or energy. The distribution of the corresponding energy gain can be seen in figure 5.2; in the simulation the UCN were stored by the material walls in the trap for $T_{\text{clean}} = 100\,\text{s}$ and then the magnetic field was switched on smoothly[3] within another $T_{\text{ramp}} = 100\,\text{s}$.

In order to test the proposed spectrum cleaning scheme, an experiment was designed and built at the TU Munich and conducted at the Institut Laue-Langevin (ILL), Grenoble in 2006 and 2007: the **Ab**sorber **Ex**periment **AbEx**.

## 5.3 Design of AbEx

The unknowns, which should be clarified, required AbEx being designed to store ultra-cold neutrons in a material storage bottle with an absorber of

---

[2] Multilayer structures can be prepared so that the real part of their Fermi potential $U_{\text{F}}$ is very close to zero.

[3] The ramping function was: $B_{\text{scal}}(t) = \frac{1}{2}(1 - \cos(\pi \cdot \frac{t}{T_{\text{ramp}}})) \in [0, 1]$.

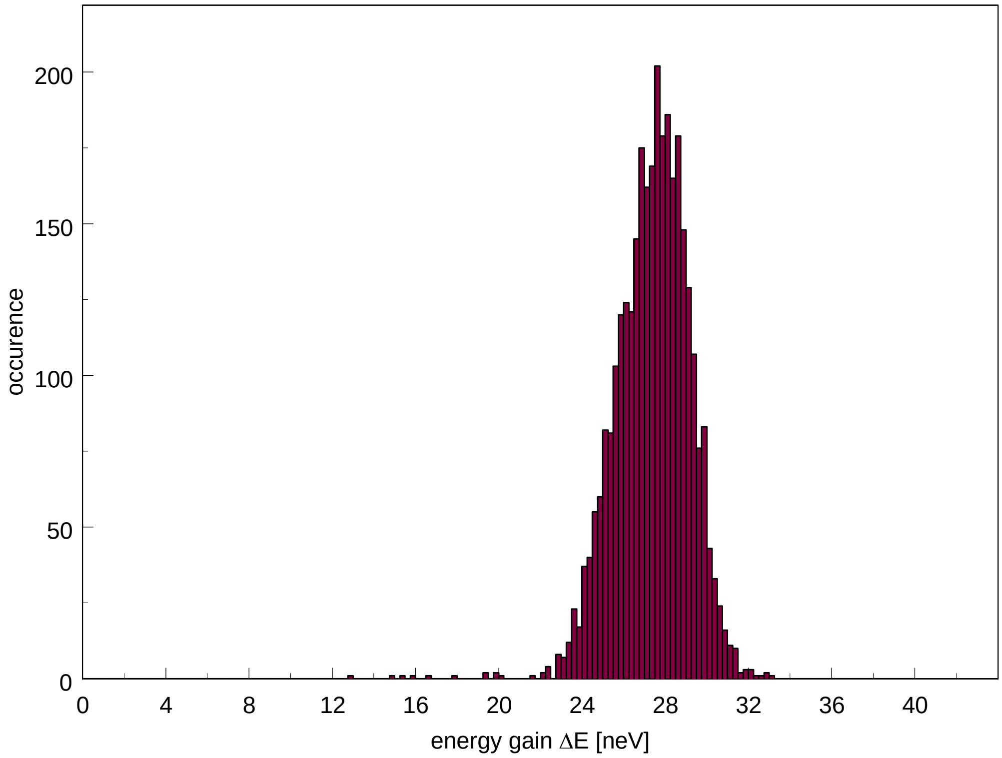

Figure 5.2: Heating of ultra-cold neutrons (simulation) when the coils of PENeLOPE are ramped up smoothly from zero to nominal current within 100 s.

similar shape as in PENeLOPE. Furthermore, it should enable us to measure energy dependent storage lifetimes for different shapes and materials of absorber at temperatures ranging from liquid helium temperature to room temperature.

A cylindrical double-walled storage bottle made of electro-polished stainless steel, also serving as helium-bath cryostat, and a ring-shaped support structure for an absorber with variable height, constitute the main components of AbEx (see figures 5.3 and 5.4). Titanium and polyethylene absorber foil were attached to copper blades mounted to the support structure.

Two UCN valves (V1 and V3)[4] connect the experiment either to the UCN source and/or the $^3$He UCN detector. To avoid the slits in UCN guide-

---

[4] These valves were originally built at E18 for the experiment CubeD$_2$ [Tor07] at the Forschungsneutronenquelle Heinz Maier-Leibnitz measuring the UCN production rate of solid deuterium in a cold neutron beam.

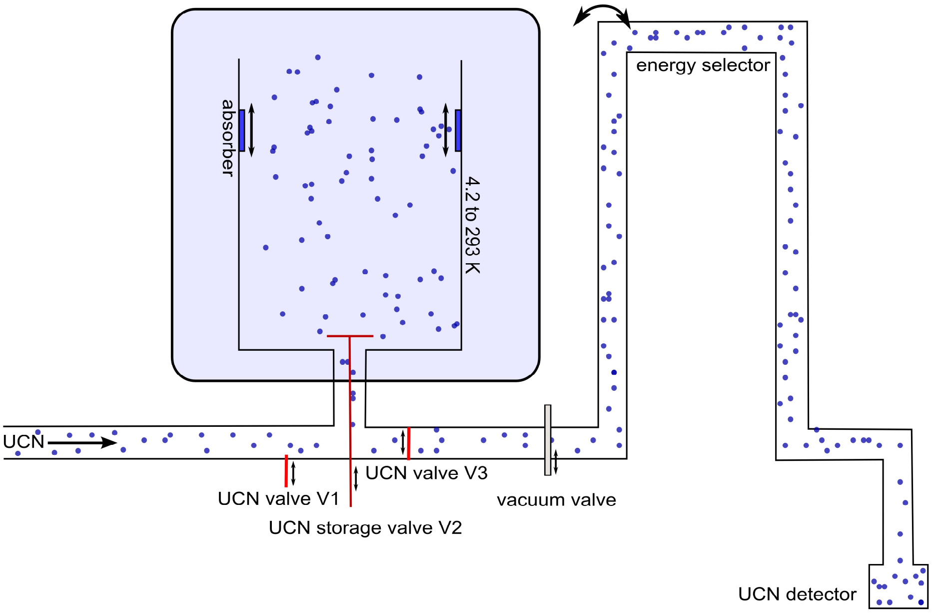

Figure 5.3: Sketch of the AbEx setup: UCN (represented by blue dots) coming from the turbine on the left can be stored in the storage vessel and then guided to the detector, after they pass a gravitational energy selector.

tube connections below the trapping volume, an additional storage valve V2 is installed at the flat bottom of the trap. This measure was taken to maximize the UCN storage lifetimes. Between UCN trap and detector, a gravitational spectrometer is situated, which is an integral energy selector to cut the spectrum of the neutrons to be detected from the bottom. This is realized by a so-called "U"; UCN guide tubes and elbows are connected to form a "U" and then turned upside down, creating a gravitational barrier. To select the low-energy threshold, the "U" has to be rotated, which poses the threat of a vacuum leakage, so it is separated from the vacuum of the cryostat by a large vacuum-tight valve.[5] This valve has a special stainless-steel protection ring to minimize UCN transport losses while it is open. B esides room temperature, two more temperature ranges may be reached by filling the cryostat with liquid nitrogen or helium.

The details of the setup are shown in figure 5.4: A nitrogen shield made of copper surrounds the bath cryostat to protect it from room-temperature radiation. Cooling of this shield is achieved through a constant flow of liquid nitrogen provided by e.g. a $lN_2$ dewar. The He and $N_2$ systems can

---

[5] VAT® HV gate valve.

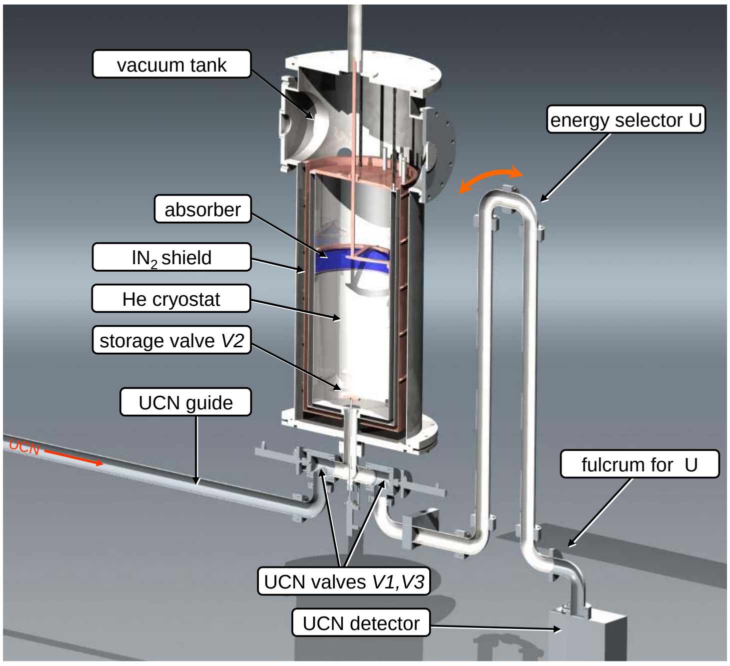

Figure 5.4: 3D cutaway view of AbEx.

also be connected to cool down the UCN storage vessel and the absorber to around 77 K.

The tube on top of the big vacuum vessel houses the absorber drive unit, a linear drive with 1000 mm travel, which is connected to the absorber support wheel by a long rod. In the original design, this copper rod should provide conductive cooling through contact with the (cold) copper lid of the bath cryostat (see figure 6.5). This cooling method proved to be to inefficient during the 2006 run, so it was revised in 2007: Some gas from the helium exhaust line of the bath cryostat now flows through small tubes on the absorber support wheel to actively cool it. In order to achieve this, 1400 mm long edge-welded bellows had to be installed to maintain an absorber travel of 800 mm.

Filling and emptying of neutrons is accomplished through a circular opening of 70 mm at the bottom, where a stainless-steel UCN guide tube can be inserted. This opening can be closed by valve V2, which is operated from the outside the vacuum vessel by an O-ring sealed feed-through at the warm tube T-piece below. Additionally, the experiment can be connected to the UCN source (V1) and the detector (V3) by stainless steel valves originally built for the CubeD$_2$ experiment [Tor07]. All three valves are driven by pressurized air as is the big vacuum valve situated between the trap and the "U". A $^3$He gas counter detects the UCN. It has a 0.1 mm aluminum entrance window and is placed more than 540 mm below the bottom level of the storage volume.[6] Figure 5.5 shows the whole experiment setup on the PF2 platform at ILL and some of the details described above.

Figure 5.5: (Left top) Absorber cooling and drive system in 2007 with bellows - (left bottom) UCN storage valve V2 - (middle) AbEx installed at the experiment plattform at ILL - (right top and middle) absorber support wheel with cooling pipes - (right bottom) $^3$He UCN detector. Two copper blades with PE foil are shown in the red inlay.

---

[6] This is necessary to overcome the aluminum Fermi potential of 54 neV.

## 5.4 Experimental procedure

To determine the UCN storage lifetime of the trap for a particular set of parameters, the system must be brought to the aspired temperature first, which is either room temperature (293 K), close to liquid nitrogen (77 K) or helium temperature (4.2 K), respectively. Then, the absorber height has to be adjusted remotely by controlling a motor on top of the linear drive system.[7] After that, the height of the U-shaped energy selector (called U-height from now on) has to be adjusted by hand. During this operation the vacuum valve to the experiment should be closed in case of a vacuum breach while rotating. Ten different storage times of UCN inside the trap can be fed to the experiment control PC, which automatically operates the three valves below the storage volume as shown in table 5.1. Filling, counting and cleaning times remain the same for all runs to maintain comparability. The last step is to start the data acquisition and the experiment control program.

| **experiment stage (and code):** | **V1** | **V2** | **V3** | **time [s]** |
|---|---|---|---|---|
| **filling** UCN into the trap (1) | open | open | closed | 100 |
| **storing** (2) | closed | closed | open | 2-500 |
| emptying and **counting** (3) | closed | open | open | 120 |
| **cleaning** the trap (4) | closed | open | open | 50 |

Table 5.1: Valve positions during different stages of AbEx. V1 is the valve between source and AbEx, V2 the storage valve and V3 the valve between AbEx and the detector (see figure 5.4).

## 5.5 Control and data acquisition

An overview of the data flow of AbEx for the beamtime 2007 can be seen in figure 5.6.

### 5.5.1 Experiment control

The AbEx valves are operated via PC using a mini DAQ and control module.[8] It can read and send analog or digital signals through 30 signal lines

---

[7] The scale measuring the position of the linear drive is recorded by a camera connected to the slow control PC.

[8] Meilhaus Redlab®.

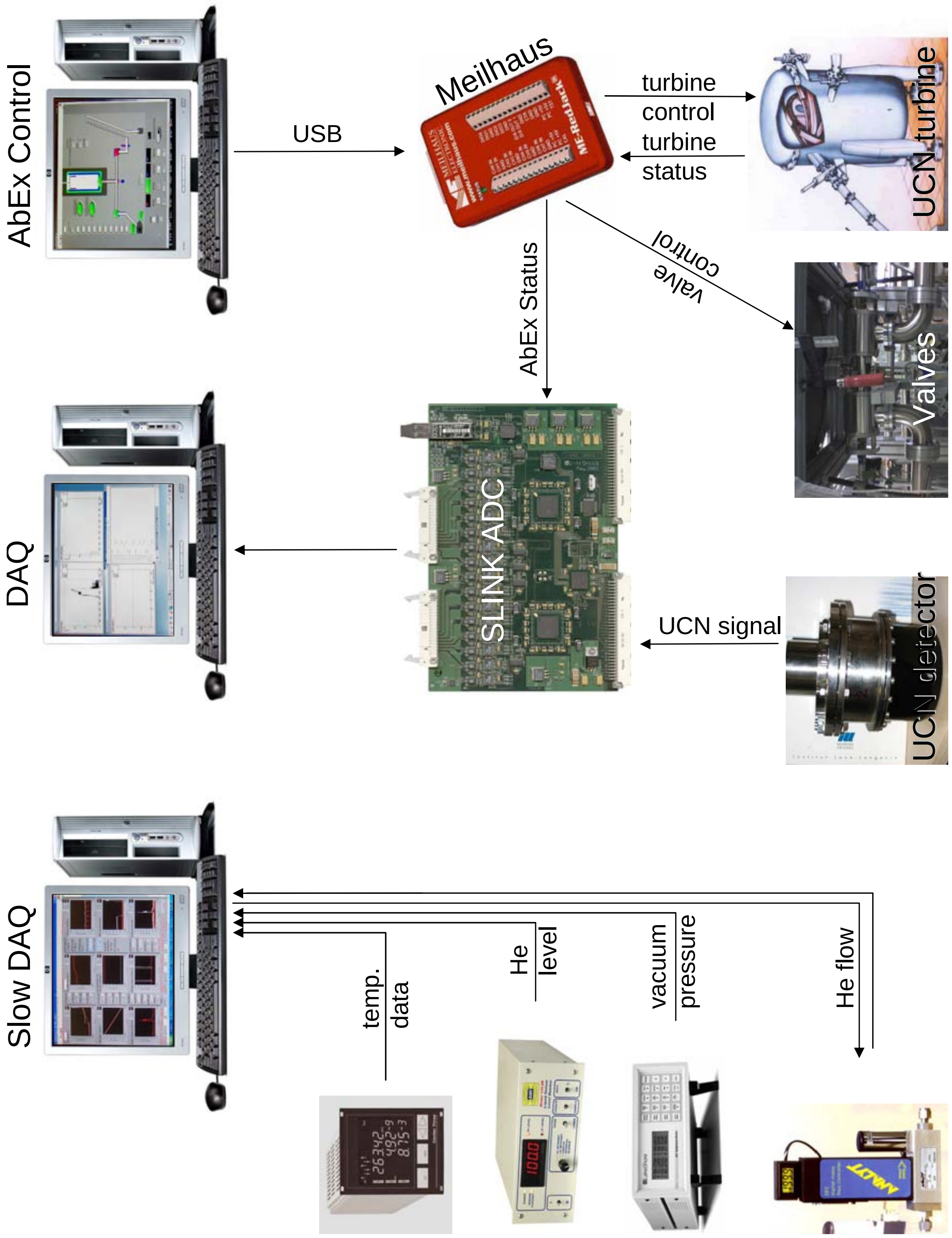

Figure 5.6: Data acquisition and control system for the AbEx beam time 2007.

and is connected to the experiment control computer via USB. A graphical development environment[9] is used as a platform for both controlling and slow data acquisition. To perform experiments at the UCN source of ILL, the experimenter also has to manage the availability of UCN from the turbine, in other words, demand the UCN beam and give a veto to other UCN users during the filling period, so that nobody is able to take away the beam during this essential period. This is controlled via the control PC and the USB box; TTL[10] signals during runtime request the beam and generate the veto during the filling period. This period is only started when the UCN beam is available. Furthermore, the experiment status code (filling, storing, counting or cleaning as in table 5.1) is transmitted to the data acquisition system via two TTL signals to be stored there. This is important because counted UCN only become meaningful by knowing during which experiment phase they were detected.

The data acquisition system was changed between the runs 2006 and 2007 from a externally triggered CAMAC based system with a controller[11] and a successive approximation ADC[12] to a self-triggered SADC system with a PCI interface which has the advantage of practically zero dead time. Both transferred their signals to a LINUX PC where they were processed and each event stored in a ROOT[13] tree.

### 5.5.2 Data-acquisition

**CAMAC DAQ system**

The $^3$He detector has two output signals, one digital gate signal and the analog signal, which is proportional to the charge deposited on the detector anode wire. To trigger the CAMAC system, the gate signal was used and the analog signal fed to the ADC. The two experiment status channels are put into a CAMAC I/O register and stored on a UCN event basis only. As elapsed and preset acquisition timer are only compared when an event is registered, the storage time can only be known to the precision of the interval between two detected UCN. Especially in the case where only few neutrons are counted, this is a major disadvantage: without further knowledge, the storage time can only be determined inaccurately. The signals are transferred to a PCI card which is then read out by the DAQ

---

[9] National Instruments LabVIEW®.

[10] Transistor-transistor logic.

[11] CAEN® CC32.

[12] Silena® 4418/V.

[13] ROOT is an object-oriented software package developed at CERN.

program.
Another drawback of the system is the comparatively large dead time, the count rate of registered signals is already saturated at around 3000 incoming per second.

**SADC DAQ system**
The SADC system is completely self-triggered, so only the analog signal from the detector is needed. It applies a scheme of different time intervals on whose signal amplitude the trigger decision is made. It is based on an ASIC[14] with continuous digitization at 40 MHz. The signal height in a large and a small time interval are compared and if the height in the small window exceeds a certain threshold, the trigger decision is made. Two modes of signal analysis can be programmed, integration or peak search; the latter was used for AbEx. For a more detailed description of the trigger scheme see [M+07a].
As the system is originally designed for high occupancy, UCN count rates of $5 \cdot 10^4\,1/\mathrm{s}$ and more are possible without further optimization. With one SADC three UCN detectors can be read out. Additionally to these three UCN signal channels (channels $0-2$), three more status channels (channels $3-5$) can be read out at equal user-defined time intervals. For the 2007 AbEx run, the two experiment status TTL signals were connected to channels three and four and read out approximately every 100 ms. This makes the accuracy of the storage time determination independent from the UCN count rate. The digital signal is transferred from the SADC card to the DAQ PC via optical fiber and the on-line analysis is performed by ROOT based programs. The status events are now stored additionally to the UCN events in the same tree but can still be distinguished because the channel number is also saved.

**Slow DAQ system**
A third PC, equipped with several serial interfaces acquires the following slow control data to monitor and control the system status:

- vacuum pressure inside the experiment (two sensors)
- temperatures at various points (eight sensors)
- helium level inside the bath cryostat
- helium mass flow through cryostat and absorber exhaust system (two flow controllers)

---

[14] ASIC: application-specific integrated circuit.

- gauge pressure inside liquid nitrogen and helium system (two sensors)

From this terminal, the cooling power to the absorber can also be regulated by flow controllers[15] at the two helium exhaust systems. Additionally the camera picture showing the current absorber position is periodically stored on this PC. All data are displayed well arranged via a LabVIEW® program and stored every ten seconds into a table file during runtime.

---

[15] Analyt MTC® mass flow controllers Series 358.

# Chapter 6

# AbEx: From the Idea to the Runs 2006 and 2007

The idea for the absorber characterization experiment came up late in 2005 and it was decided to apply for a beam time at the ILL, Grenoble for the second half of 2006. Therefore a proposal was submitted to the scientific council of the ILL February 2006 (cf. appendix D). Right after that it was agreed upon to use an existing vacuum vessel[1] and equip it with a large UCN storage vessel and the necessary cryogenics to cool down the storage surface and the absorber as described in chapter 5. Titanium and polyethylene (PE) were chosen as absorbers; the first is predominantly a neutron absorber, the second a neutron upscatterer at room temperature. The UCN upscattering cross section of PE is almost two orders of magnitude larger than the absorption cross-section but decreases drastically by cooling down the absorber [HL05].

## 6.1 The theory of neutron absorbers and upscatterers

The real Fermi potential, describing the spatially averaged interaction of neutrons with wall materials, can be extended to the complex plane $V_\mathrm{F} = U_\mathrm{F} + iW_\mathrm{F}$ and thus incorporate losses. From the total cross section (absorption and upscattering added up) at thermal neutron velocities $\overline{v}_\mathrm{th} \approx 2200\,\frac{\mathrm{m}}{\mathrm{s}}$ the imaginary part of the potential can be computed via

$$W_\mathrm{F} = \frac{\hbar}{2} N \sigma_\mathrm{tot} \overline{v}_\mathrm{th}. \tag{6.1}$$

---

[1] Mark 3000 built by H. Yoshiki et al. [Y+92].

$\sigma_{\text{tot}}$ denotes the total cross section

$$\sigma_{\text{tot}} = \sigma_{\text{absorption}} + \sigma_{\text{coh. scatt.}} + \sigma_{\text{incoh. scatt.}} + \dots \tag{6.2}$$

(absorption *plus* upscattering) and $N = \frac{\rho N_{\text{A}}}{A}$ the number density, where $\rho$ is the mass density, $N_{\text{A}}$ the Avogadro constant and $A$ the mass number of the material [G+91]. For molecules or mixtures one just has to sum up the individual potentials weighted with the respective number density of the element in the molecule or mixture

$$U_{\text{F}} = 2\pi\hbar \sum_i N_{\text{i}} b_{\text{i}} \quad \text{and} \quad W_{\text{F}} = \frac{\hbar \overline{v}_{\text{th}}}{2} \sum_i N_{\text{i}} \sigma_{\text{tot,i}}. \tag{6.3}$$

The next step is to transfer this expansion to the simple quantum mechanical step potential displayed in figure 6.1.

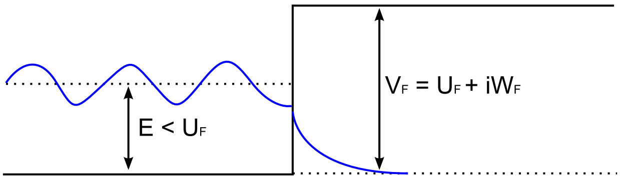

Figure 6.1: Complex potential step.

When the kinetic energy of the neutron is smaller than the real part of the Fermi potential ($E < U_{\text{F}}$), a non-zero imaginary part leads to absorption or upscattering, which may be associated to the loss probability per bounce encountered during material UCN storage. For $E > U_{\text{F}}$ not all neutrons are transmitted into the material, but a certain reflection probability exists. In other words, the imaginary part introduces imperfection, UCN reflectors do not reflect to 100% and absorption also does not happen to 100% where desired.

Following the notation in [Sch05], but using a complex potential the reflection probability r can be derived to be

$$r = \frac{U_{\text{F}}^2 + W_{\text{F}}^2}{\left(E + \sqrt{2E(Q + E - U_{\text{F}})} + Q\right)^2}, \tag{6.4}$$

with $Q = \sqrt{(E - U_{\text{F}})^2 + W_{\text{F}}^2}$ (see appendix C). $E$ is the kinetic energy component perpendicular to the reflecting wall. The frequently used formula

$$r = 1 - 2\frac{W_{\text{F}}}{U_{\text{F}}} \sqrt{\frac{E}{U_{\text{F}} - E}}, \tag{6.5}$$

published for example by Golub *et al.* [G+91], is an approximation of equation 6.4 using series-expansion, keeping only first-order terms. It is a good approximation for cases where $E << U_{\mathrm{F}}$, but not valid if $E > U_{\mathrm{F}}$ (see figure 6.2).

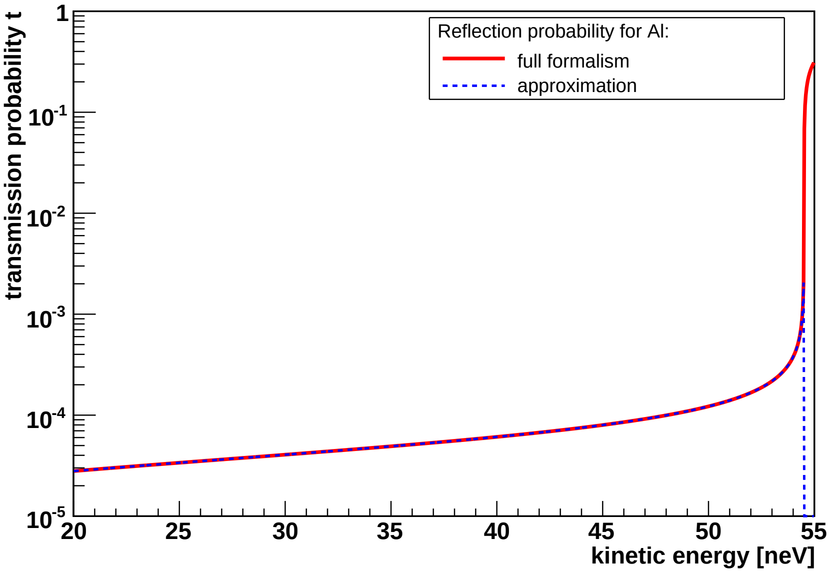

Figure 6.2: Comparison of full and approximated transmission probability $t$ for UCN hitting aluminum ($V_{\mathrm{F}} = (54.2 + \mathrm{i}\, 1.01 \cdot 10^{-3})$neV) with kinetic energy $E$ perpendicular to the material boundary.

With the full solution on the other hand, the reflection probability of absorbing or upscattering materials can also be predicted. The reflection probabilities $r$ for some commonly used materials are plotted in figure 6.3. Here one can see that despite having enough kinetic energy to overcome the step potential there is still a significant probability to be reflected.

It is commonly stated by UCN experts that polyethylene should only be used at room-temperature because upscattering is highly suppressed at low temperatures. The evolution of the cross section was calculated by Hill and Liu [HL05], and from figure 6.4 it is visible that below approximately 70 K absorption should be the dominant process.

However, in theory, the influence of the imaginary part of the spectrum is much smaller than naively expected. The curves for absorption and total cross section of polyethylene in figure 6.3 do not differ significantly, differences are less than $10^{-3}$. Hence, the question is raised why PE is said to be less favorable at low temperatures? Is the step potential model too

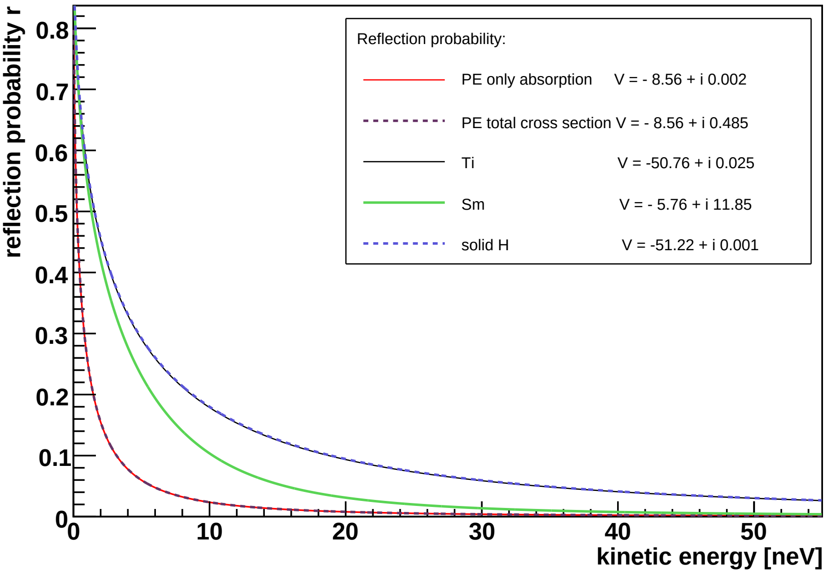

Figure 6.3: Reflection probabilities for a UCN hitting a material boundary with kinetic energy *E* perpendicular to this boundary.

simple? Do surface contaminations, predominantly by hydrogen, play a role?

To test these hypothesis was another reason to conduct AbEx.

## 6.2 Beam time 2006: Cooling problems

21 days of beam-time were allocated for AbEx at the UCN facility PF2 at Niveau D of ILL, Grenoble. The experiment included testing polyethylene and titanium absorbers down to liquid-helium temperatures and also examining the temperature dependence of the storage lifetime of the stainless steel trap. 16 days of data taking could be achieved after installing the setup.

At the ILL it became clear that the heat load on the 4 K vessel was quite large and the helium consumption up to 20 $\mathrm{dm}^3/\mathrm{h}$. This put a stringent limit on the measuring time below liquid nitrogen temperature, because the supply of helium was limited to 200 $\mathrm{dm}^3$ per day at maximum. In addition the heat removal from the absorber support wheel was not sufficient: Conductive cooling just by means of contact of the helium vessel lid to the copper absorber support rod through CuBe springs (cf. figure 6.5) proved to be too inefficient. Keeping the bath cryostat below 5 K for 20 h

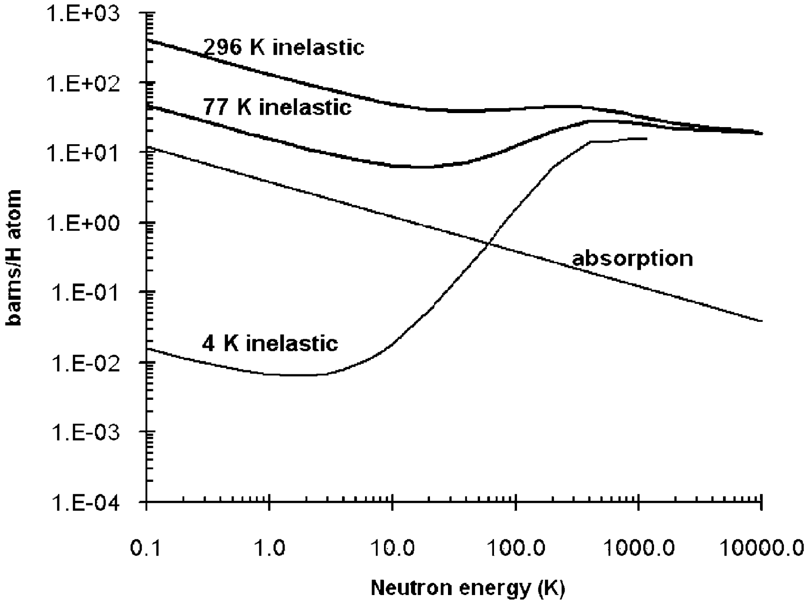

Figure 6.4: Calculated neutron inelastic scattering cross section for polyethylene at temperatures of 296, 77 and 4 K, resp., compared with the nuclear absorption cross-section. Neutron energies are expressed in Kelvin [HL05].

decreased the absorber temperature to 79 K only.[2] After experiencing this with polyethylene mounted in the experiment it was decided to sacrifice the possibility to vary the height of the absorber to be able to reach liquid-helium temperature. Hence, after finishing the runs with PE, the titanium absorber was directly mounted on the inner wall of the storage vessel, still maintaining a similar shape as on the copper blades originally foreseen.

The data collected in the 2006 beam time comprises measurements without absorber down to liquid-helium temperature, with polyethylene at different absorber heights down to approximately liquid-nitrogen temperature and with titanium at fixed height down to 4.5 K.

## 6.3 Beam time 2007: Revised cooling

Some beam time during the 2006 experiment run was needed to learn about the behavior of the system: optimum filling, storage and emptying

---

[2] The lowest absorber temperature achieved with only liquid nitrogen cooling was 115 K.

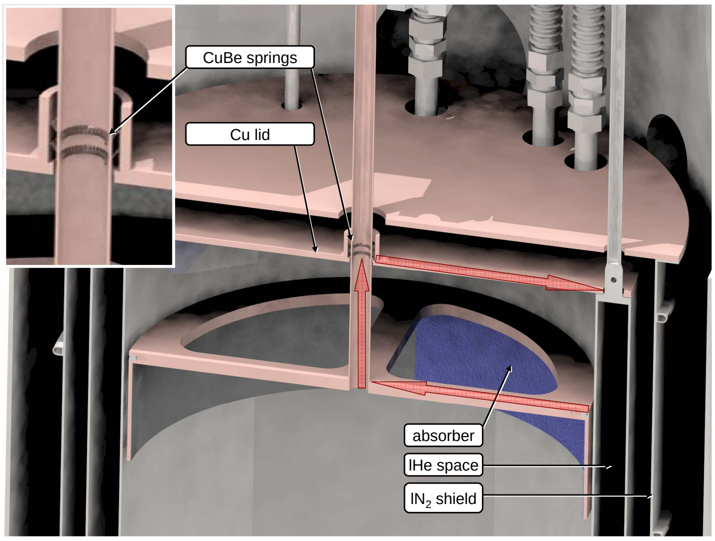

Figure 6.5: Contact of helium lid to the copper absorber support tube. The red arrows symbolize the conductive heat transfer path.

times, cooling procedure, statistics needed and so on. In 2007, the beam time could be used more efficiently to collect valid data.

The revised absorber cooling system described in section 5.3 allowed to achieve temperatures below 20 K, maintaining the variability of the absorber height. Additional minimization of the heat input through the UCN guides in combination with better radiation shielding of the system helped reducing the helium consumption by more than a factor of two.

While analyzing the 2006 data it turned out that the absorber scheme is quite powerful and eliminates the marginal UCN so fast, that statistics became very limited for some parameter sets. Hence, the focus of the second beam time was on measuring polyethylene down to very low temperatures and with less absorber surface: of the three copper blades, only one was covered with PE for a significant part of the data taking. This worked out as foreseen; through better statistics, the errors became smaller and the effects more pronounced, especially looking at the temperature dependence.

Additionally, right next to the storage valve (V2) an inlet for $O_2$ gas into the trap was installed to freeze out solid $O_2$ at the cold inner surfaces of the helium cryostat. Solid oxygen has a very small imaginary part of the Fermi potential ($W_{F,abs} = 5.9 \cdot 10^{-7}$neV), so the storage lifetime can be much higher than for stainless steel. Several freeze out trials were performed to see the influence of the solid oxygen on the storage lifetime and also to see if the neutron lifetime extrapolation as described in section 2.2 can be performed with AbEx.

# Chapter 7

# AbEx: Data Analysis and Results

The principle of data analysis of the experiments 2006 and 2007 is similar, so it will be described together just mentioning the small differences and refinements for the 2007 data.

## 7.1 Structure of the raw data

Every neutron signal registered in the $^3$He detector is stored in a ROOT tree with a unique event number. The tree is stored in a file named with the date and time of the run for later recognition. For each event the time stamp of detection and the signal height are stored along with a boolean signaling an overflow of the ADC. The 2006 data also contains the input register value, which describes the experiment status of AbEx through an integer between 0 and 3. For 2007 this was changed (see section 5.5.2) and the status codes are stored as separate events. They can later be distinguished from real UCN events through the channel number of the ADC. These so called heart-beat events are recorded with a repetition rate of approximately 10 per second to arrive at an accurate measurement of the storage lifetime. The raw time histogram for a typical run can be seen in figure 7.1. Here the heart-beat channels are already excluded and a signal-height cut placed to choose only real UCN events in the detector.

## 7.2 Data analysis step by step

The parameters of the respective experiment run (absorber type, U height, absorber height, ROOT tree file name and so on) were written down in a table file at ILL and are read in by the ROOT data processing macro, which

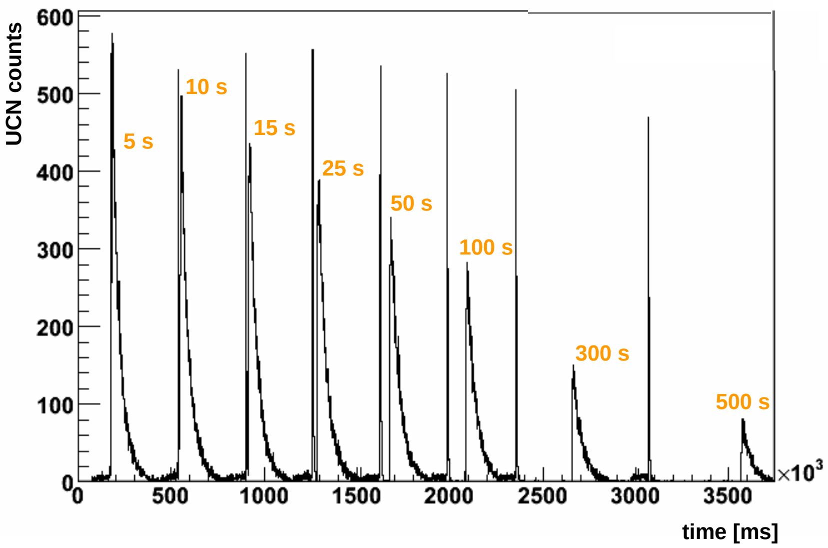

Figure 7.1: Raw time histogram of UCN counts. U-height $h_U = 400$ mm, height of full polyethylene absorber ring $h_{abs} = 751$ mm above trap bottom, absorber temperature $T_{abs} = 22$ K, bottle temperature $T_{bottle} = 4.6$ K. The respective storage times in the trap are marked in the histogram.

opens the corresponding ROOT file.

Data analysis is done on a run-by-run basis, so the first step of processing the root file is separating the individual runs. The decision on the starting point of a storage cycle is taken through changes of the experiment status codes: the code changes from 4 (cleaning) to 1 (filling). In 2007 however this was not that easy because the SADC system was very sensitive to electronic noise caused by the magnetic valves of the pressurized-air steering of the UCN valves. Hence, every time the valves were operated, the status signals fluctuated: therefore, an algorithm to detect the fluctuations and correct them had to be implemented, only confirming a change of status code after it was constant for at least 4 s. By this method the storage start and end time and the end of the counting period were also determined.

The UCN counts from the beginning of the UCN storage to the end of the cleaning period are then histogrammed and the analysis performed on this histogram (see figure 7.2). The binning of the time spectrum is chosen accordingly: the shorter the storage time the smaller the bin width.

A significant challenge for the analysis is posed by the short storage times necessary for absorber characterization. For storage times below 20 s UCN stored in the tube "T" below the cryogenic vessel between the valves V1

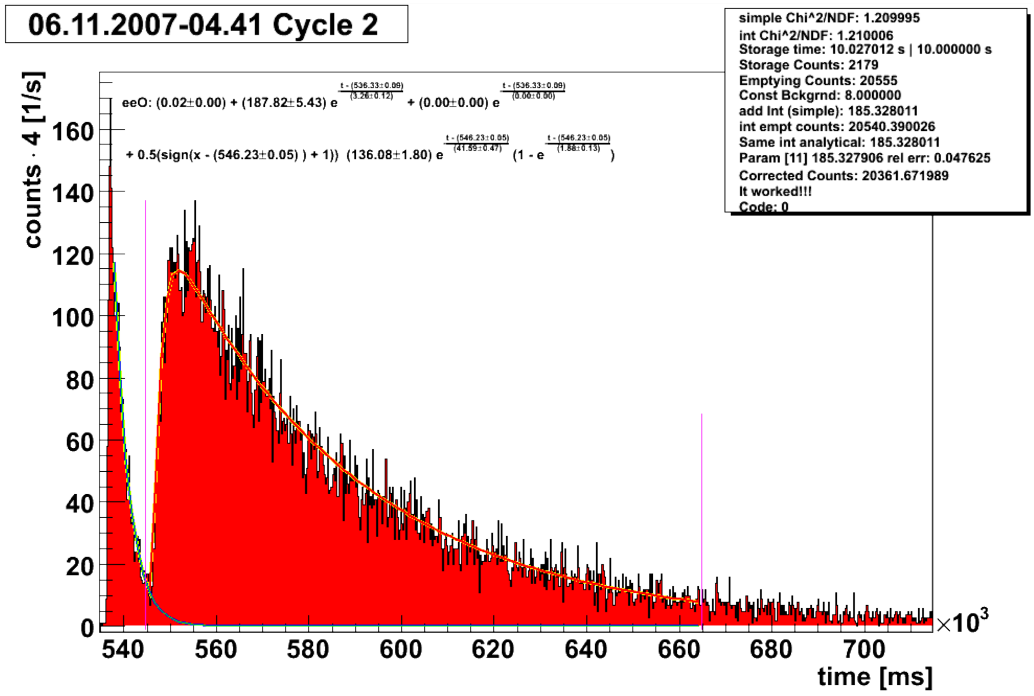

Figure 7.2: Time spectrum of UCN counts for one storage cycle including fit functions for background subtraction. The fit function (*ee*0) with the final parameters is printed, along with some data of the analysis of the current run.

and V3 have not completely vanished when the actual counting period starts. The storage lifetime of these UCN lies in the range of 2 s to 5 s. Hence, it contributes an exponential background to the UCN counts, which has to be subtracted. This can only be achieved by fitting the whole time histogram from the falling edge of the histogram during the storage period to the end of the counting period. Statistical emptying and filling processes are best described by exponential functions, hence for the dataset analyzed, the fit function consists of three falling and one rising exponential

$$\begin{aligned} F_{\mathrm{s}}(t) = B_{\mathrm{c}} &+ N_{\mathrm{s}1} \cdot e^{-\frac{t-T_{\mathrm{ss}}}{\tau_{\mathrm{s}1}}} + N_{\mathrm{s}2} \cdot e^{-\frac{t-T_{\mathrm{ss}}}{\tau_{\mathrm{s}2}}} \\ &+ \Theta(t-T_{\mathrm{cs}}) \cdot N_{\mathrm{c}} \cdot \left(1 - e^{-\frac{t-T_{\mathrm{cs}}}{\tau_{\mathrm{cr}}}}\right) \cdot e^{-\frac{t-T_{\mathrm{cs}}}{\tau_{\mathrm{cf}}}} \end{aligned} \tag{7.1}$$

with the Heavyside step-function $\Theta$. The first two falling exponential functions ($\tau_{\mathrm{s}1}$ and $\tau_{\mathrm{s}2}$) describe the emptying of the tubes below the storage volume into the detector, the rising exponential ($\tau_{\mathrm{cr}}$) the increase of incoming UCN to the detector and the last falling exponent ($\tau_{\mathrm{cf}}$) the emptying of the storage volume. The time offsets of the storage and counting period $T_{\mathrm{ss}}$ and $T_{\mathrm{cs}}$ are set to the respective starting times. They are not fixed, as the UCN have to traverse the guide system to the detector with a length of around 3 m, which could lead to an additional delay. $B_{\mathrm{c}}$ is the constant background, which comes from false counts in the $^{3}$He detector, e.g. stray neutrons in the reactor hall, leaky UCN valves or electronic noise. It is not a fit parameter, but determined for each experiment run from an averaged count rate at the end of the cleaning phases and right before filling starts and fixed to this value. The maxima of the histogram are used to set the initial values of $N_{\mathrm{s1}}$, $N_{\mathrm{s2}}$ and $N_{\mathrm{c}}$ and finally the time constants for the two falling exponents of the storage period, $\tau_{\mathrm{s1}}$ and $\tau_{\mathrm{s2}}$, and the falling and rising time constants $\tau_{\mathrm{cf}}$ and $\tau_{\mathrm{cr}}$ are initialized with the same values for all runs.[1]

A $\chi^2$ and a Maximum-Likelihood fit are performed, depending on the filling degree of the histogram: for small statistics per bin the Maximum-Likelihood method works better. To determine the exponential background, the area below the first falling exponents

$$I_{\mathrm{BG}} = \int_{T_1}^{T_2} \left( N_{\mathrm{s1}} \cdot e^{-\frac{t-T_{\mathrm{ss}}}{\tau_{\mathrm{s1}}}} + N_{\mathrm{s2}} \cdot e^{-\frac{t-T_{\mathrm{ss}}}{\tau_{\mathrm{s2}}}} \right) \mathrm{dt} \tag{7.2}$$

is calculated between $T_1$ and $T_2$, the start and the end of the counting period, respectively. The error of this integral is not trivial to calculate, as the fit parameters of equation 7.1 might be correlated, which complicates error propagation dramatically. Instead, the integral function 7.2 itself is placed into the fit function in a next step (see appendix F). Then the fit procedure is repeated with the new function and the error of $I_{\mathrm{BG}}$ is automatically obtained through the Minuit fit routines of ROOT.

If this is successful, the result appears as can be seen in figure 7.2; the fit function without the integral parameter is displayed with the final parameters and their uncertainties. The fit functions are plotted in yellow ($F_{\mathrm{s}}$) and red ($F_{\mathrm{f}}$), blue and green curves show the exponential background. The latter ones include the parameterization of the integral.

The cycle histograms change completely for different experiment parameter sets: figure 7.3 shows two example sets of parameters. On the left, the "U" is at zero and the absorber at 551 mm above bottle ground, on the right the "U" is higher and the absorber lower leading to significantly less counts for the same storage times. When the "U" is above the height of the

---

[1] The initialization values are: $\tau_{\mathrm{s1}} = 3$ s, $\tau_{\mathrm{s2}} = 30$ s, $\tau_{\mathrm{cf}} = 30$ s and $\tau_{\mathrm{cr}} = 2$ s.

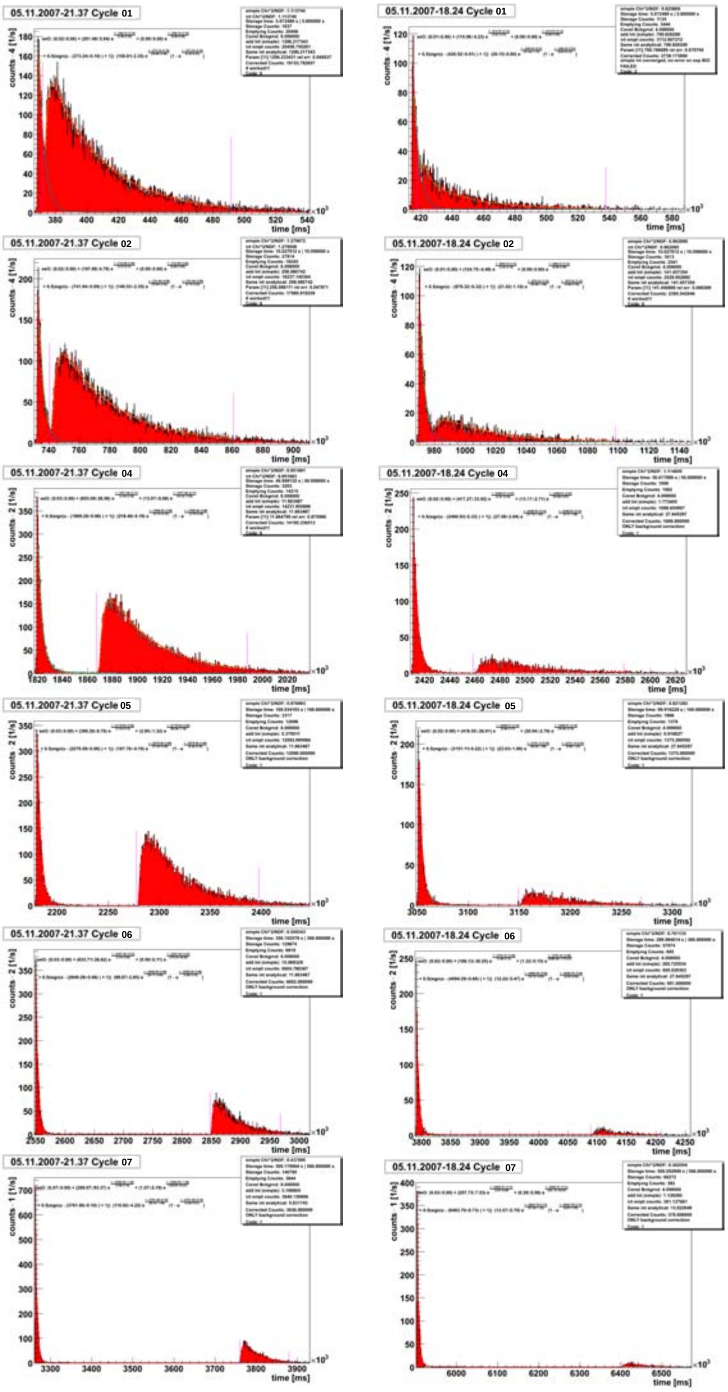

Figure 7.3: Examples of time histograms with a 360° PE absorber ring for two different sets of parameters: absorber height 551 on the left side and 351 mm on the right, U-height 0 and 200 mm, absorber temperature 18 and 15 K, respectively. Storage times between 5 and 500 s.

absorber, it is even more like that and the long storage times were often omitted, because very few UCN survived to collect sufficient statistics.

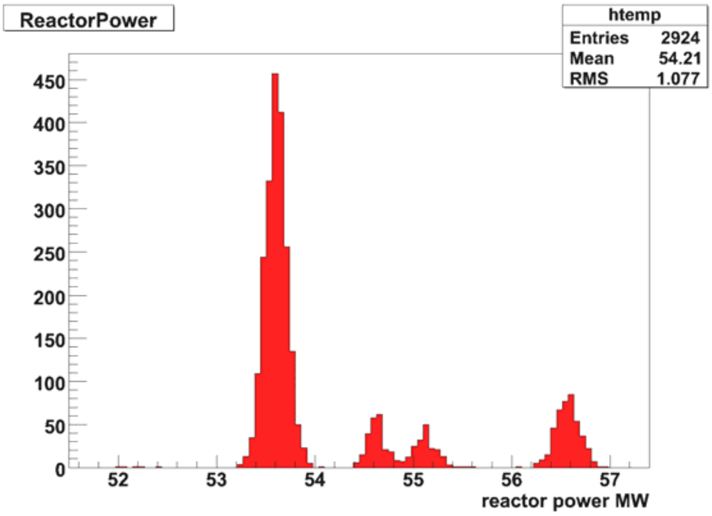

Figure 7.4: Reactor power distribution for all 2924 analyzed experiment cycles in November 2007.

After determining the number of UCN, that survived the storage time, with its error, the slow DAQ data, i.e. temperatures and pressures, is processed. It is read in from the table file written during the runtime and the corresponding data retrieved by comparing the date and time information of the DAQ and the slow DAQ files. The relevant data during the respective storage period is collected and if there are more values available the averaged is calculated. The same is done with the reactor power data, which is provided by the ILL for users as a text file. The UCN flux depends linearly on the thermal power of the reactor, so all counts are normalized to 54 MW, which was the nominal value for the beam time November 2007. Figure 7.4 shows the histogrammed distribution of the reactor power over time.

All the relevant data of the cycle is then stored in a new ROOT tree for further analysis.

After having prepared all the values for the different parameter sets, the next step is to calculate the lifetimes of UCN in the trap. This lifetime includes the $\beta$ decay and the loss lifetime. To do this, all the corresponding information has to be collected, the counted UCN plotted against the storage time and fitted with an exponential curve. Two lifetimes are then determined, the storage lifetime $\tau_{\text{st}}$ and the loss lifetime $\tau_{\text{loss}}$ (cf. section 2.3).

The evaluated data is (again) stored in a ROOT tree.

There are two cases of fits: if the "U" is below the height of the absorber, the more interesting UCN are the ones with longer storage lifetime, i.e. after the absorber has removed the high-energy neutrons. When the "U" is above the absorber, only the high-energy particles are detected, so longer storage times are not possible. For these reasons, a cut was performed on the data to arrive at sensible storage lifetime values; only storage times $T_{\mathrm{st}} \geq 25\,\mathrm{s}$ are chosen, when the "U" is below the absorber. This results in a bias towards longer storage lifetimes, but reflects the realistic situation that one waits to start storage lifetime measurements, until the absorber has successfully removed the unwanted UCN.

## 7.3 UCN energy spectrum

It is quite important for UCN storage experiments to know the energy distribution in the vessel. Some lifetime extrapolation methods (cf. section 2.2), depend on this knowledge. In a dedicated procedure, the UCN spectrum was measured with the "U" of AbEx, but without storing.

The two UCN valves V1 and V3 (compare 5.4) were opened for this measurement and, to see the influence of the storage bottle with the absorber, the storage valve V2 opened or closed. In this way, the detector was continuously connected to the neutron source and the number of UCN counted for 100 s for each of 15 different "U" positions. Figure 7.5 shows the integral spectrum on the left side and the differential energy distribution on the right for both cases (V2 closed and open). One can see that less UCN reach the detector when the storage bottle is connected. The reason is quite obvious, as the titanium absorber foil was installed in the experiment, at a height of 600 mm. It corresponds to an energy of 61.5 neV and in the differential spectrum the density decreases above this value; many of the neutrons entering the storage vessel are removed by the absorber even in the case of an open bottle. Moreover, neutrons that do not reach the absorber, having less than 61.5 neV energy, are also more likely to be lost if they enter the trap because this results in many additional reflections which lead to loss. Many UCN, however, never enter the trap and find the direct way to the detector.

When the storage valve is closed, the differential spectrum still has a maximum around 50 neV and is not, as one would expected, a Maxwellian spectrum ($\propto E$) up to much higher energies. This is very likely a result of the transmission function of the gravitational spectrometer, which is not

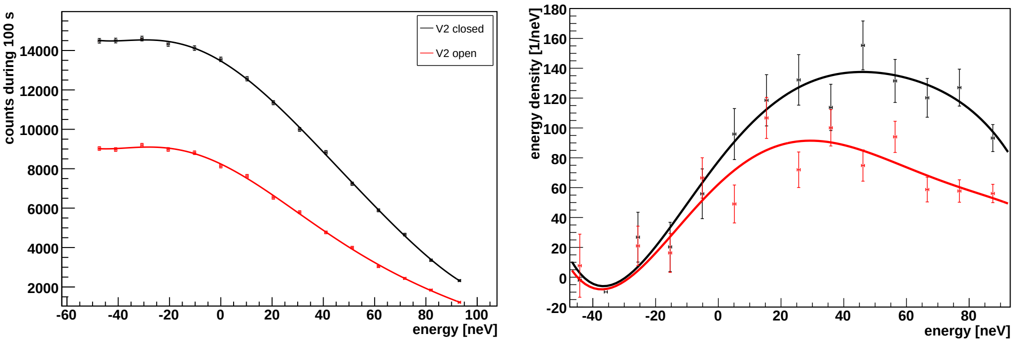

Figure 7.5: UCN energy spectrum of PF2 at ILL, Grenoble, measured in continuous mode with a "U" for storage valve V2 of AbEx open and closed. The energy is with respect to the bottom of the storage vessel. (Left) integral spectrum - (right) differential spectrum.

constant over a broad energy range.

## 7.4 Leakage rate of UCN valves

Four types of valves were used at the ILL: two valves from CubeD$_2$ (V1 and V3), one VAT vacuum-tight valve with a protection ring when opened, a rotating valve which is located right after the UCN turbine at PF2 and the storage valve V2. During our beam time 2006 we encountered quite a high UCN background count rate during periods where the CubeD$_2$ valves were closed. Therefore it was decided to operate the rotating PF2 valve simultaneously with valve V1. As a result, the background vanished almost completely. A leak test of the UCN valves was performed afterwards with full beam, only closing the valve to be tested. Big differences in the UCN tightness were encountered: the ILL-built PF2 valve, despite not being vacuum tight, surpasses the commercial high-vacuum VAT valve, whereas the CubeD$_2$ valve cannot keep up in terms of UCN tightness (see table 7.1).

## 7.5 Comparison with Monte Carlo simulation

The C++ program for neutron tracking in PENeLOPE, described in chapter 4, can also easily be adapted to simulate the absorber experiment. The magnetic field interpolation may be omitted and the inner reflecting cylin-

| **Valve closed** | **UCN counts in 100** s | **leakage rate** |
|---|---|---|
| all open | $302723 \pm 550$ | 1 |
| PF2 valve | $3 \pm 1.7$ | $(9.9 \pm 5.7) \cdot 10^{-6}$ |
| VAT valve | $9 \pm 3$ | $(2.9 \pm 1.0) \cdot 10^{-5}$ |
| CubeD$_2$ | $596 \pm 24$ | $(1.97 \pm 0.08) \cdot 10^{-3}$ |

Table 7.1: Leakage rate of the UCN valves used for AbEx at the PF2 facility, ILL.

der of PENeLOPE is also absent, but the main structure and equations remain the same. The capabilities of the simulation are:

- Neutron tracking in the gravitational field.
- Reflection (specular and diffuse) at the walls of the storage vessel (stainless steel) implemented, including statistical non-specular reflection .
- Reflection at the copper lid on top of the storage vessel.
- Absorber geometry and theory included (complex step potential). Because of its complexity, the absorber support structure is not incorporated.
- Possible slit at storage valve of AbEx implemented as loss mechanism.

With the help of this code, the theories used to describe UCN loss, upscattering and absorption can be applied to simulate AbEx, compare the experimental results and help predicting results of future experiments.

To do this, the Monte Carlo simulation is carried out several times adjusting the Fermi potentials $V_F$ of the stainless-steel storage walls and the absorber material so that the results fit to the experiment. Thus, one can check the simulation results and maybe determine deviations of the experimental results from the theoretical predictions. Starting points are the theoretical parameters (cf. table 2.1) of the Fermi potentials. The parameters to be adjusted are $W_F$ of stainless steel and $U_F$ of the respective absorber because they have the biggest influence on the storage lifetime curve, as will be shown below. Figure 7.6 shows one example curve.

However, the fit does not converge for all cases, because of the effect of the support structure: sometimes the experimental storage lifetimes for $h_U \leq h_{abs}$ are chronically smaller than in the simulation, even when the absorber is assumed to be black for UCN ($U_F = 0, W_F \neq 0$). Multiple reflection at the copper support structure, especially in the slit between

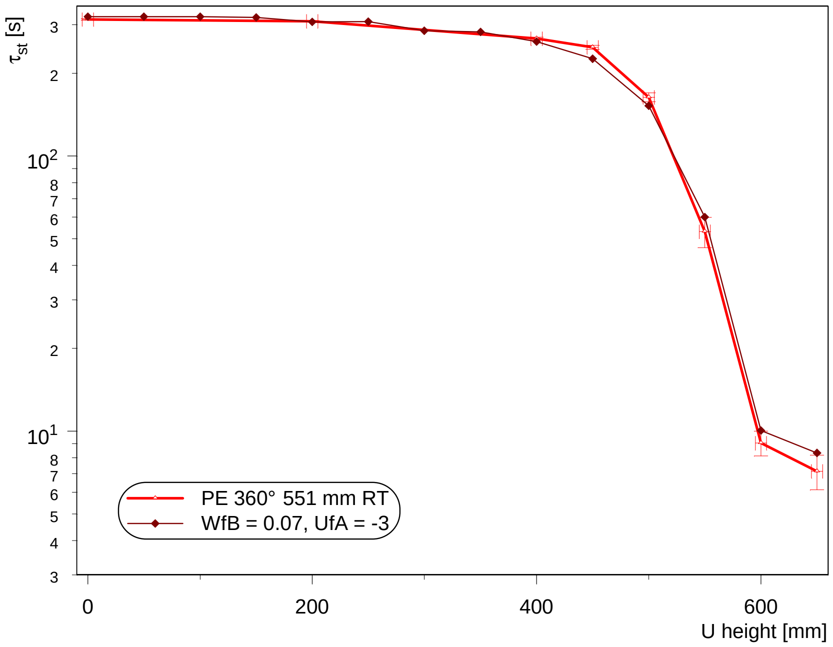

Figure 7.6: Matching of Monte Carlo simulation to AbEx data for a 360° absorber ring of polyethylene at room temperature 551 mm above trap bottom. Fermi Potentials used: stainless steel $V_{\mathrm{F,SS}} = (183.04 + i0.07)\,\mathrm{neV}$, polyethylene: $V_{\mathrm{F,PE}} = (-3 + i0.002)\,\mathrm{neV}$.

the blades and the trap walls leads to significant losses. Table 7.2 shows the cases where it worked quite well. The main conclusions drawn from it should be, that the storage bottle worked much better in 2007, because the imaginary part of the Fermi potential of the storage material for that year is lower throughout the table. The real part of the absorber is closer to zero for room temperature measurements leading to shorter storage lifetimes for high-energy UCN.

## 7.6 General efficiency of the proposed absorber geometry

The goal of introducing an absorber to PENeLOPE is to eliminate the UCN of kinetic energy exceeding the magnetic trap depth within a reasonable period of time. Effectively, the fraction of neutrons above the trap depth of PENeLOPE surviving the cleaning phase should be low enough *not* to influence the measured neutron lifetime on a level above $10^{-4}$. If

| **Year** | **Configuration** | **$W_F$ of trap [neV]** | **$U_F$ of absorber [neV]** |
|---|---|---|---|
| 2006 | no abs., RT | 0.25 | – |
| 2006 | no abs., $lN_2$,lHe | 0.15 | – |
| 2006 | Ti 360°, RT | 0.2 | $-5$ |
| 2006 | Ti 360°, $lN_2$ | 0.2 | 2 |
| 2006 | Ti 360°, lHe | 0.2 | $-10$ |
| 2007 | Ti 120°, RT | 0.082 | $+6$ |
| 2007 | PE 360°, RT | 0.07 | $-3$ |
| 2007 | PE 360°, $lN_2$ | 0.075 | $-4$ |
| 2007 | PE 120°, RT | 0.04 | 1.5 |
| 2007 | PE 120°, lHe | 0.05 | $+3$ |

Table 7.2: Results for Fermi potentials after adjusting Monte Carlo simulation to experimental data, RT: room temperature, $lN_2$: liquid nitrogen temperature, lHe: liquid helium temperature.

one draws very conservative conclusions from figure 7.7 for the three differences of U- and absorber height $\Delta h = 0$, 50 and 100 mm one arrives at storage lifetimes well below $\tau_{\mathrm{st}} < 70$, 15 and 10 s. Translating this into a fraction of surviving UCN after e.g. 100 s cleaning time results in $N/N_0 < 0.23|_{0\,\mathrm{mm}}$, $1.3 \cdot 10^{-3}|_{50\,\mathrm{mm}}$ and $4.5 \cdot 10^{-5}|_{100\,\mathrm{mm}}$. This means that the lower edge of the absorber in PENeLOPE should be set at a height corresponding to the magnetic trap depth minus 10 cm. By doing this it is safe to say, that after the cleaning phase of 100 s, the number of UCN above trap depth is reduced to $4.5 \cdot 10^{-5}$ of the number before. Now, again taking a pessimistic approach, one may assume all neutrons with up to 40 neV above threshold have the same storage lifetime, and the ones with even higher energies do not play a role.[2] To calculate the effect of the marginal UCN on the measured neutron lifetime, one needs to know the ratio of the marginal UCN (with energies between 110 and 150 neV) to the stored UCN (0 to 110 neV) initially present in the trap: it is 0.85 using the expected $v^2$-spectrum of UCN sources. Assuming a mean storage lifetime $\overline{\tau}_{\mathrm{st}} = 500$ s for these marginal UCN,[3] the time evolution of neutrons in PENeLOPE during the storage phase is described by

$$N(t) = N_0 \cdot \left( e^{-t/\tau_{\mathrm{n}}} + R \cdot e^{-t/\overline{\tau_{\mathrm{st}}}} \right), \tag{7.3}$$

---

[2] The storage lifetime gets shorter for higher energies, therefore this is a plausible assumption (cf figure 5.1).

[3] A storage lifetime in the center of the interval [0 s, 885.7 s] produces the biggest systematic effect.

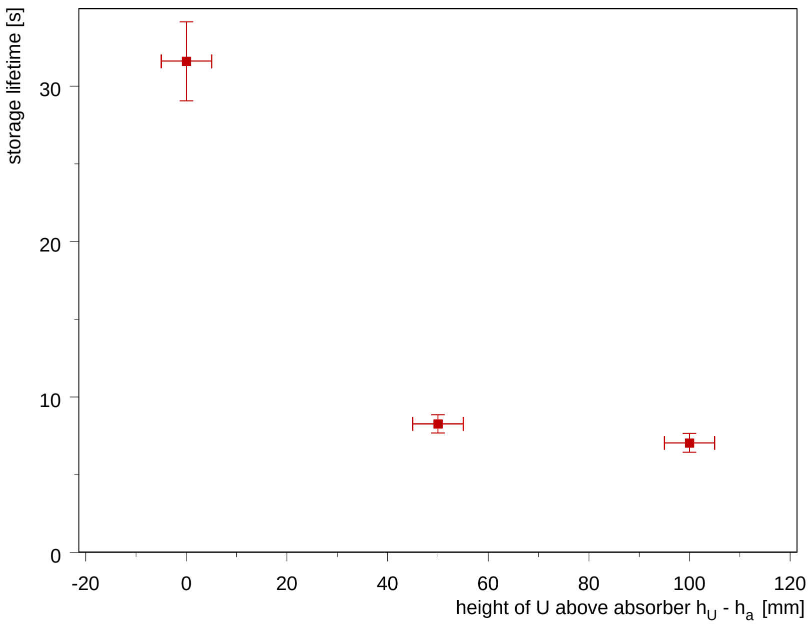

Figure 7.7: Mean storage lifetimes against U-height minus height of lower absorber edge for all runs of AbEx (PE, Ti, 10 K to 293 K) with a full absorber ring.

where $R = 4.5 \cdot 10^{-5} \cdot 0.85 < 4 \cdot 10^{-5}$ describes the ratio of marginal UCN surviving the cleaning phase to magnetically trapped UCN. The second addend in equation 7.3 produces the systematic false effect shortening the measured neutron lifetime. Filling histograms according to equation 7.3 and then fitting with only one exponential decay, the false effect can be quantified: even at a statistical precision $\delta\tau_{\text{stat}} = 0.03$ s, the assumed neutron decay lifetime is still within the error bar. This precision is almost one magnitude lower than the goal of PENeLOPE.

Additionally, the Monte Carlo simulations show that UCN of less than 40 neV above the trap depth have a storage lifetime in the magnetic field of PENeLOPE of $\tau_{\text{st}} > 800$ s, which reduces the effect even more.

To cut a long story short, the proposed absorber setup should by far be efficient enough to remove marginally trapped UCN from the trap to ensure reaching a neutron lifetime precision well below 0.1 s, no matter at which temperature the absorber is kept at and whether polyethylene or titanium is used.

## 7.7 Titanium and polyethylene at different temperatures

### Material comparison at room temperature

The essence of UCN physics in material traps incorporating absorbers can be inferred from plots of the UCN storage lifetime against U-height. Here, one may compare different absorber geometries, materials, absorber heights or temperatures. Figure 7.8 shows an example: the "U" cuts the UCN spectrum from the bottom; neutrons with kinetic energy lower than the corresponding height $E_{\text{kin}} < mgh_{\text{U}}$ cannot reach the detector. Hence, for U-heights below the absorber, the storage lifetime $\tau_{\text{st}}$ depends mostly on the conditions of the storage surfaces below the absorber. This can be seen by comparing the 2006 and 2007 data (see green data set in figure 7.8): storage lifetimes for lower energies are consistently two to three times higher in 2007! Two possible explanations can be found. Either the

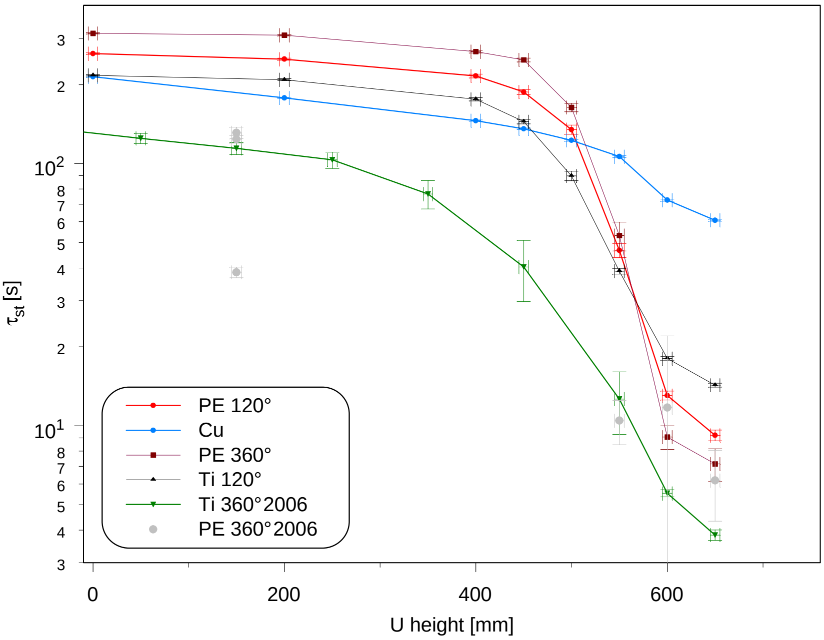

Figure 7.8: Storage lifetimes of neutrons against U-height above the bottom level of the trap. The absorber was 551 mm above this level, except for 2006 data, where it was at 600 mm. For better comparison, these are shifted 50 mm to the left. 120°: only one of the three copper support plates were covered with absorber, 360°: all three copper support plates were covered with absorber.

bottle treatment done before the beam time 2007 reduced the wall losses,[4] and/or the unavoidable slit between the storage-valve underside and the trap bottom was smaller. The latter could come about because even the slightest misalignment of the valve V2 affects the cross section of the slit.

A second effect that can be seen in this range is the sensitivity on the absorber efficiency; the more efficient the absorber, the higher the storage lifetime. A more efficient absorber results in shorter $\tau_{\mathrm{st}}$ for high-energy UCN, so after 25 s, which is the shortest storage time used in the case $h_{\mathrm{U}} < h_{\mathrm{abs}}$, the high-energy neutrons are removed almost completely. If the absorber is less efficient (as it is the case when only $120^\circ$ of absorber are installed instead of $360^\circ$), the neutrons with enough kinetic energy to reach the absorber ring are removed more slowly and therefore they reduce the mean storage lifetime of all UCN to a greater extent.

In the high-energy range, one can directly compare the absorber power of different setups. The effect of the support structure is visible in the blue curve of figure 7.8; multiple reflections between the Cu blades and the stainless-steel storage walls lead to higher losses, as well as absorption on the two temperature sensors mounted on the support wheel with their cables: this results in a knee in the curve at 550 mm. Nevertheless, compared with the absorber, this effect is quite small (the storage lifetime for $h_U = 650$ mm is only reduced to 61 s, in contrast to 7 s for polyethylene). Subtracting the effect of the absorber support structure to isolate the absorber efficiency is not performed because if one does so for all U-heights, the resulting storage lifetimes would be negative in the interval $0 < h_{\mathrm{U}} < h_{\mathrm{abs}}$. The alternative, to correct only for higher $h_{\mathrm{U}}$ would introduce a further bias and could be disputable.

From figure 7.8 it is visible that titanium and polyethylene at room temperature are comparable, with slightly faster removal of high-energy UCN for polyethylene. The two graphs taken in 2006 drop out a little because of the different bottle storage lifetimes mentioned above; the light gray one for polyethylene is only shown to get a feeling of the larger error bars in 2006 and that the 2007 data is much more reliable.

**Temperature dependence of storage lifetimes of the copper support structure without absorber**

Figure 7.9 shows the data set for the copper support without any absorber material attached. The temperature dependence is clearly visible:

---

[4] Cleaning procedure 2007: washing with laundry detergent and mechanical rubbing, rinsing first with normal, then with demineralized water. In 2006, the trap was not cleaned after returning from the electro-polishing procedure.

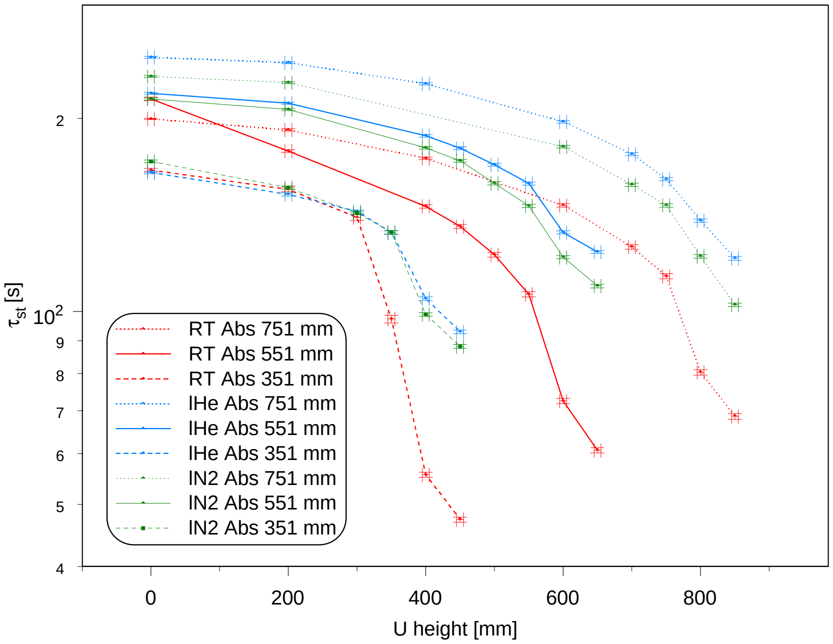

Figure 7.9: Storage lifetimes of neutrons stored in the AbEx trap against U-height above trap bottom level. No absorber material was attached to the copper support structure. Heights of this support structure: 351, 551 and 751 mm above bottom, at liquid helium, liquid nitrogen and room temperature.

the lower the temperature, the higher the storage lifetime. Especially for $h_U > h_{abs}$ the change is biggest between room and liquid-nitrogen temperature. This is also where the upscattering cross section changes dramatically, which, in turn, influences the imaginary part of the Fermi-potential $W_F$. As copper has a high real part $U_F = 170\,\text{neV}$, almost all UCN hitting it are below the critical velocity and do not get into the copper, so the knee in the curves at $h_U = h_{abs}$ comes from multiple reflections at the structure and resulting losses. Particularly UCN entering the slit between the outside of the copper blades and the stainless steel wall, which has a clearance $< 2$ mm will undergo hundreds of reflections. Hence, the upsacttering probability of the exponential tail of the neutron wave function inside Cu is reduced at lower temperatures and the storage lifetime higher for high-energy UCN.

The absorber height also plays a role, changing the ratio of the absorber structure surface to the (stainless-steel) storage surface below: at lower heights, this ratio is higher and with that the loss probability. This causes

a larger storage lifetime of high energy UCN with increasing absorber height.
Another fact to keep in mind when comparing with results including an absorber is that $\tau_{st}$ is the highest for $h_U < h_{abs}$ when the system is cooled with liquid helium.

### Temperature dependence of storage bottle without absorber

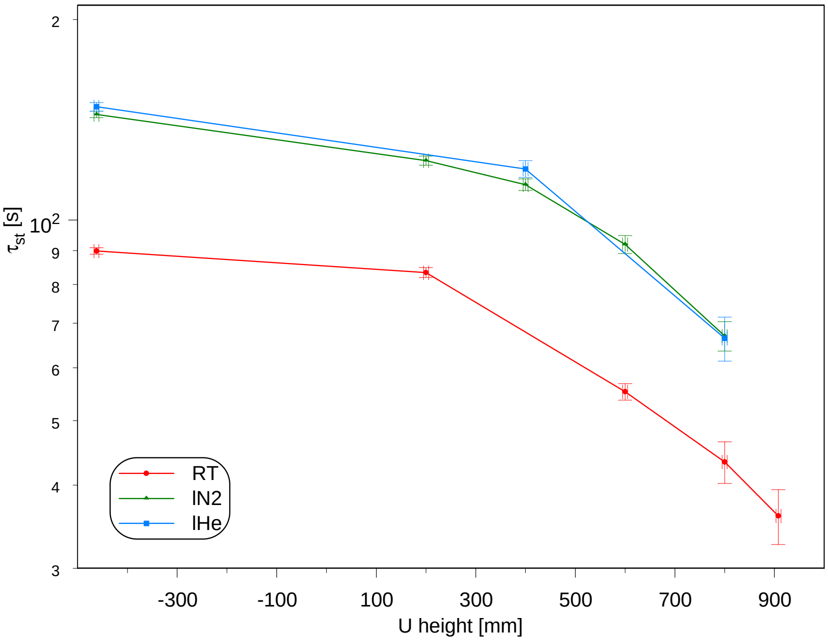

Figure 7.10: Storage lifetimes of neutrons stored in the AbEx trap against U-height above trap bottom level for an empty storage bottle.

Figure 7.10 shows the storage lifetimes in the empty UCN storage vessel of AbEx during the beam time 2006; it is clearly visible that without introducing means to cut the UCN spectrum at the top, it is not necessary to cool down the reflection surface below liquid nitrogen temperature.

### Temperature dependence with polyethylene absorber

The clearest conclusions can be drawn from data where only one of the copper blades is covered with polyethylene; statistics for "U" positions above absorber are better in this case, because more neutrons survive the storage period. This results in smaller error bars and more pronounced effects. As figure 7.11 visualizes, the temperature dependence with absorber

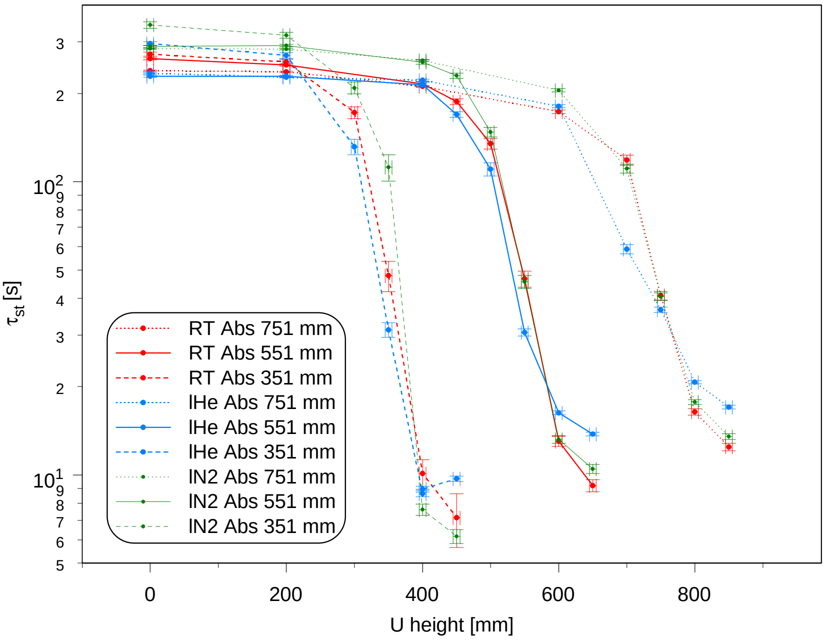

Figure 7.11: Storage lifetimes of neutrons stored in the AbEx trap against U-height above trap bottom level. Polyethylene absorber, one copper blade covered with PE: 120°. Absorber heights: 351, 551 and 751 mm above bottom, at liquid helium, liquid nitrogen and room temperature.

is somehow inverted: when $h_U < h_{abs}$, the storage lifetime is the highest at liquid nitrogen temperature, but for $h_U > h_{abs}$ this is the case for liquid helium temperature. These two facts have a connection: as explained above, the absorber efficiency influences the storage lifetimes also for low U-heights. At liquid-helium temperature, the storage lifetime for UCN with $E_{kin} < E_{pot}(h_{abs})$ would be the highest because of reduced upscattering at the stainless steel walls as shown during the reference measurement without absorber. The longer storage lifetimes of UCN having higher energy compensate this effect. A greater fraction of these is still present after the shortest storage time of 25 s. This, in turn, reduces the mean storage lifetime.

Nevertheless, it is not quite clear, why for $h_U > h_{abs}$ the storage lifetime is significantly higher only at liquid helium temperature. This cannot be explained by the smaller upscattering cross section, as shown in chapter 6.1. An explanation may lie in hydrogen freeze out on the absorber surface: solid $H_2$ has a Fermi potential $U_F = -51\,\text{neV}$, which is more negative than PE and would lead to a higher reflection probability for UCN with a low velocity component rectangular to the absorber surface. Hence, a longer storage lifetime results. Hydrogen seems a quite natural assumption, as most other components of the residual gas are frozen out at liquid nitrogen temperature already and in addition, the residual gas at pressures below $10^{-4}$ mbar mostly comprises of hydrogen.

### Temperature dependence with titanium absorber

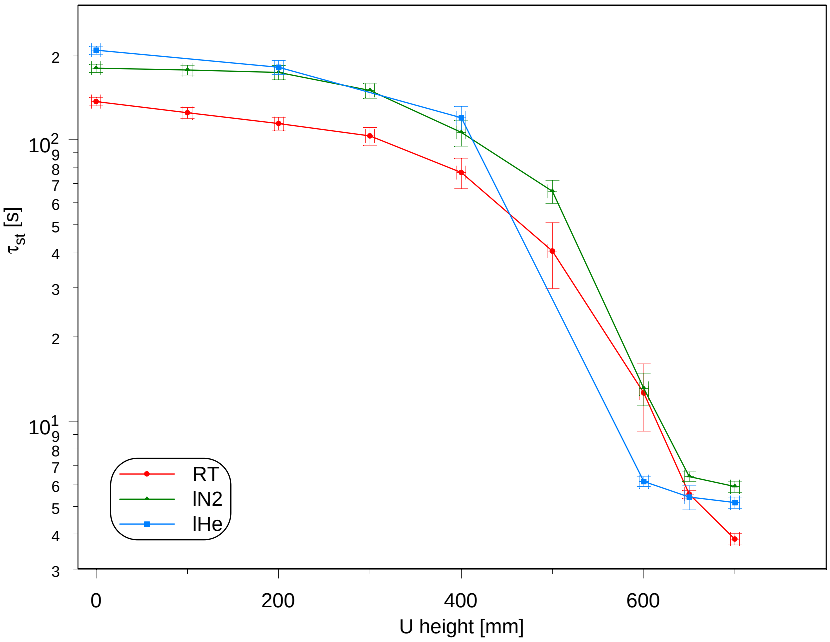

Figure 7.12: Storage lifetimes of neutrons stored in the AbEx trap against U-height above trap bottom level for titanium absorber, full 360° at 600 mm above bottom, at liquid helium, liquid nitrogen and room temperature.

As already mentioned, in 2006 the titanium absorber was directly put on the storage walls at a height of 600 mm to ensure its cooling, therefore only this absorber height is available to analyze the temperature dependence. It is shown in figure 7.12.

The storage lifetime of high-energy UCN ($h_U > 600$ mm) is also larger for lower temperature, but $\tau_{st}$ is the highest at liquid nitrogen temperature. Maybe the polyethylene foil used is more porous and therefore may adsorb more hydrogen on its surface. However, the values at liquid helium and nitrogen temperature for $h_U = 700$ mm are almost compatible considering their error bars. Nevertheless, here one can clearly see the dependence of the averged storage lifetime of all UCN in the trap ($h_U < h_{abs}$) on the storage lifeftime of high energy neutrons: unlike with polyethylene, $\tau_{st}$ is the highest at liquid helium temperature.

### Trial freeze-out of solid oxygen on the storage wall surfaces

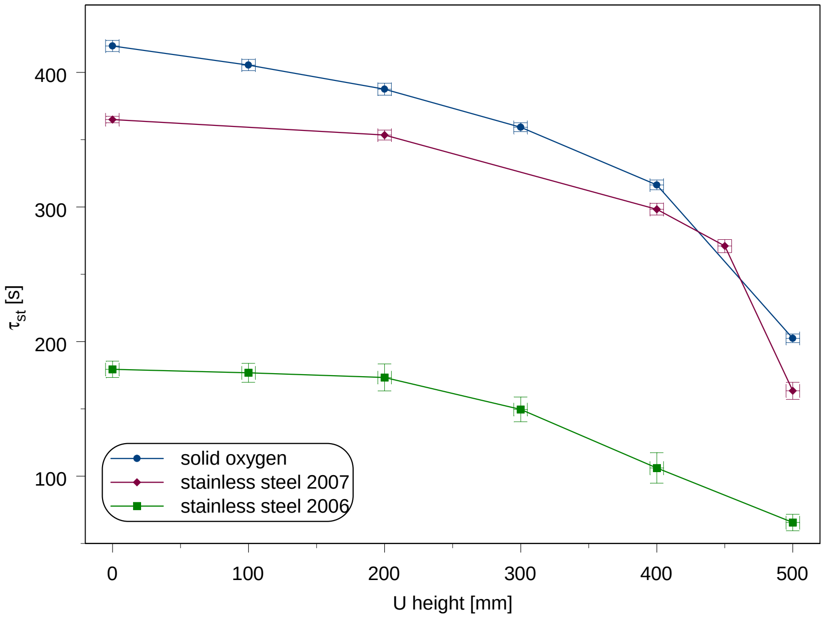

Figure 7.13: Best storage lifetimes achieved in AbEx 2006, 2007 and with solid oxygen coating.

For several storage cycles during the 2007 run the storage walls were covered with solid oxygen, as it has very low absorption cross section (four orders of magnitude smaller than that of stainless steel).
The procedure was to let a controlled amount ($n \approx 7 \cdot 10^{-3}$ mol) of oxygen gas flow into the trap through a needle valve, while the storage vessel was cooled with liquid helium. This was repeated several time and UCN storage runs with fixed storage time $T_{st} = 200$ s were performed in between. After five runs, the UCN counts after a storage time of 200 s reached a plateau and the freeze out was stopped. During the whole process, the absorber (PE in this case) was kept above the boiling point of oxygen, $T_b = 90.20$ K, to avoid covering its surface, too.
In the ideal world, a perfectly smooth surface without cracks and holes

covered with a solid $O_2$ layer should allow UCN storage lifetimes much longer than 800 s. As can be seen in figure 7.13, we could only reach storage lifetimes up to $\tau_{\mathrm{st}} = 420 \pm 6\,\mathrm{s}$. The main reason is the very simple flow scheme of oxygen gas into the UCN trap: the gas flows in through the storage valve V2 and therefore the outer bottom edge of the storage vessel and the upper part of the stainless steel wall are not in direct line of sight for the $O_2$ molecules. It is highly probable that the oxygen will stick to the cold surface at around 4 K on its first contact, so the storage surfaces might have been covered only partially.

The potential of solid oxygen is visible, but a lifetime extrapolation was not feasible for the short storage lifetimes achieved. For the future a more complicated freeze out scheme is advised: a gas spray system could be mounted on the absorber support wheel with direct line of sight to all storage surfaces. It could then also be moved vertically to cover the trap walls more uniformly.

## 7.8 Discussion of the AbEx results

There are several remarkable points resulting from the data analysis of AbEx:

- Probably the most important confirmation is that the absorber scheme of one ring with a height of 10 cm at the outer walls of PENeLOPE's UCN storage vessel is powerful enough to reduce the systematic effect of marginally trapped UCN below our precision goal.

- Polyethylene can be used as an effective UCN absorber in the temperature range of superconducting coil operation. When the absorber is thick enough (orders of magnitude larger than de Broglie wave length of UCN), it is more important that the absolute value of the real part of the Fermi potential $|U_{\mathrm{F}}|$ is as small as possible. As soon as the UCN overcomes the barrier at the surface and penetrates the absorber, even a very small absorption or upscattering cross section (which translates to $W_{\mathrm{F}}$) suffices to remove the UCN. Surface contaminations, however, play an important role by possibly increasing $|U_{\mathrm{F}}|$ and hence the reflection probability. This could be seen in the case of polyethylene.

- The dependence of the storage lifetime on the imaginary part or the Fermi potential $W_{\mathrm{F}}$ of the storage surface for $E_{\mathrm{UCN}} < U_{\mathrm{F}}$ is large compared to the case of an absorber; during every reflection, the UCN wave function reaches into the material on the scale of the depth of penetration and therefore "sees" up scattering or absorbing centers. In the course of the many hundred reflections even small differences in $W_F$ add up and result in quite different storage lifetimes. This effect is visible when cooling down the stainless steel storage vessel walls and also the copper absorber support structure, where multiple reflections are the major loss mechanism as well. Thus, the storage lifetime in the storage vessel is largest at liquid-helium temperature, but only when the absorber efficiency is not reduced significantly at the same time.

- The common notion that "absorbers" like polyethylene, where the UCN upscattering cross section at room temperature is much higher than the absorption cross-section, should not be used in cryogenic environments cannot be confirmed. As mentioned above, the reduction of the cross section is not important as long as the material is thick compared with the deBroglie wavelength of the incident neutron.

# Chapter 8

# Precision Goals and Status of PENeLOPE

The first ideas for a magnetic UCN storage experiment to measure the lifetime of the free neutron came up at the institute E18 in the 1990s. The proposals how to implement it changed from a "2m-pole" trap in azimuthal direction [Zim00] over a setup with permanent magnets to the superconducting solution [Pic04] to be realized in the next years. The superconducting multipole arrangement described in chapter 3 proved to be superior in many ways, especially considering the statistics that can be reached and the possibility to examine systematic effects.

## 8.1 Expected precision and error budget of neutron lifetime measured with PENeLOPE

### 8.1.1 Statistical precision

The statistical precision, that can be reached during one neutron storage cycle by counting the decay protons, depends on the UCN source, the experiment will be placed at. Table 8.1 summarizes how much statistics can be collected at different sources and what precision may be expected.

### 8.1.2 Estimation of systematic effects

Besides acquiring sufficient statistics, it is crucial to keep the systematic effects on the measured neutron lifetime under control:

| UCN source | neutrons per filling | $\Delta\tau_{\text{stat}}$ per cycle | cycles for $\Delta\tau_{\text{stat}} = 0.1\,\text{s}$ | days to reach $\Delta\tau_{\text{stat}} = 0.1\,\text{s}$ |
|---|---|---|---|---|
| ILL | $2.6 \cdot 10^6$ | 1.95 s | 1960 | 82 days |
| PSI | $1.5 \cdot 10^8$ | 0.53 s | 29 | 1.2 days |
| FRM2 | $5 \cdot 10^8$ | 0.29 s | 9 | 0.4 days |

Table 8.1: Statistics of PENeLOPE at different UCN sources counting neutron-decay protons. Assumed UCN densities: Institut Laue-Langevin (ILL), Grenoble, France 50 cm$^{-3}$, Paul-Scherrer Institut (PSI), Villigen, Switzerland, 2000 cm$^{-3}$, Maier-Leibnitz Forschungsneutronenquelle (FRM2), Munich, Germany, $10^4$ cm$^{-3}$; filling efficiencies were taken into account. The proton detection efficiency was set to 60% to be on the safe side. The uncorrelated proton-detector background was assumed to be 100 s$^{-1}$, but set as a free parameter in the exponential fit-procedure.

- **Neutron spin-flip:** If the spin of a stored UCN flips, it will become attracted by high-field areas and subsequently be lost at the walls. Calculations yield an upper limit for the spin-flip probability during a storage time of 1500 s of less than $10^{-5}$, which results in a spin-flip loss time $\tau_{\text{sf}} > 10^8$ s. The consequential systematic effect on the measured neutron lifetime is $\Delta\tau_{\text{spinflip}} < 0.01$ s.

- **Marginally trapped UCN:** As desribed in chapter 7, the absorber scheme developped for PENeLOPE is sufficient to suppress this effect: during 100 s of cleaning time with the absorber in place, the ratio of marginally trapped UCN to magnetically stored UCN is reduced to less than $2 \cdot 10^{-5}$.
  In the energy range up to 40 neV above trapping energy, Monte Carlo simulations of stored neutrons in PENeLOPE yield only around 100 wall collision per UCN during the whole storage period, resulting in a loss lifetime of those UCN $\tau_{\text{lm}} = 1.4 \cdot 10^5$ s. Here a loss probability of $1 \cdot 10^{-4}$ per wall collision was assumed. This leads to a total lifetime $\tau_{\text{marginal}} = \frac{\tau_{\text{n}}\tau_{\text{lm}}}{\tau_{\text{n}}+\tau_{\text{lm}}} > 880$ s, using the Particle Data Group average $\tau_{\text{n}} = 885.7$ s. Simulating the process of fitting to the proton time spectrum with a much lower storage lifetime for marginally trapped UCN $\tau_{\text{marginal}} = 500$ s shows no systematic effect down to a statistical precision $\Delta\tau_{\text{stat}} = 0.03$ s.

- **Absorption of UCN by rest gas atoms:** To reduce the decay-proton scattering on rest gas atoms down to a tolerable level, the vacuum has to be better than $p = 1 \cdot 10^{-7}$ mbar [Brö04]. For this pressure, taking the worst case scenario of a pure nitrogen atmosphere ($\sigma_{\mathrm{abs,th}} = 1.3\,\mathrm{barn}$), the UCN loss time computes to $\tau_{\mathrm{abs}} = 1.1 \cdot 10^{7}$ s and the effect on $\tau_{\mathrm{n}}$ is $\Delta\tau_{\mathrm{abs}} = 0.07\,\mathrm{s}$. In real vacuum systems, at those pressures, the rest gas is mainly hydrogen ($\sigma_{\mathrm{abs,th}} = 0.33\,\mathrm{barn}$), altering those numbers to $\tau_{\mathrm{abs}} = 6.3 \cdot 10^{7}$ s and $\Delta\tau_{\mathrm{abs}} = 0.01$ s.[1] Having such large cold surfaces in the cryostat,[2] it should be possible to go down to even better vacua to further reduce this effect.

- **Time variation of the spatial UCN distribution in the trap:** In reference [Brö04], this was examined following the approaches of Ignatovitch and Golub [Ign90, G+91] with the result that no time variation is to be expected.

### 8.1.3 Possibilities to analyze systematic effects

In addition to the fact that all systematics we could think of are below the precision goal of $\Delta\tau_{\mathrm{n}} = 0.1$ s, the many variable parameters of PENeLOPE provide the opportunity to investigate many systematical aspects:

- Variation of the storage coil current results in the variation of the trapping potential; effects depending on the UCN energy may be examined.
- Variation of the spin-flip-suppression (racetrack) coil current should result in a variation of the spin-flip probability and the number of detected UCN during magnetic storage (cf. chapter 4).
- Variation of absorber height or leaving out the absorber both lead to a variation of the ratio magnetically stored UCN to marginally trapped UCN (cf. chapter 7).
- Variation of the vacuum pressure changes the UCN scattering probability on rest gas.
- Introducing a gravitational spectrometer between source and trap produces a cut on the lowest energy of trapped UCN.
- Variation of the proton-extraction and acceleration voltage results in a variation of the proton collection efficiency and the energy deposition per proton in the detector.

---

[1] With all surfaces at around 4 K in the storage volume, upscattering will be largely suppressed.

[2] The surface of the helium cryostat (cf. figure 8.1) adds up to around 10 $\mathrm{m}^2$.

- Analysis of the UCN energy spectrum after storage may help determining energy dependent systematics.
- Introduction of an electron veto detector above the thin proton detector allows ruling out correlated electron background.

Additionally, the two lifetime measurement principles (proton detection and counting remaining UCN) allow a mutual cross-check. Considering the number of experiment runs necessary to examine this parameter space thoroughly, it is clear that the ultimate precision that can be reached depends on the functioning of the new high-density UCN sources mentioned.

### 8.1.4 Estimated error budget of PENeLOPE

An example of how the overall error budget might look like is shown in table 8.1.4.

| **Uncertainty** | **Value** |
|---|---:|
| Statistical @ PSI after 10 days | 0.034 s |
| Neutron spin flip | $< 0.01$ s |
| Marginally trapped UCN | $< 0.03$ s |
| UCN scattering on rest gas | $< 0.07$ s |
| Time variation of UCN distribution | - |
| Total (quadratic sum) | **0.084 s** |

Table 8.2: Error budget for the neutron lifetime assuming operation at a UCN source comparable to the one constructed at Paul Scherrer Institut, Villigen, Switzerland.

## 8.2 Status of PENeLOPE

### 8.2.1 Feasibility and design study

Planning, designing and constructing such a sophisticated instrument including superconductors and consequentially cryogenics is quite a complex task. The design of the magnetic and electric fields and the coil geometry was done at our institute E18, but some engineering design

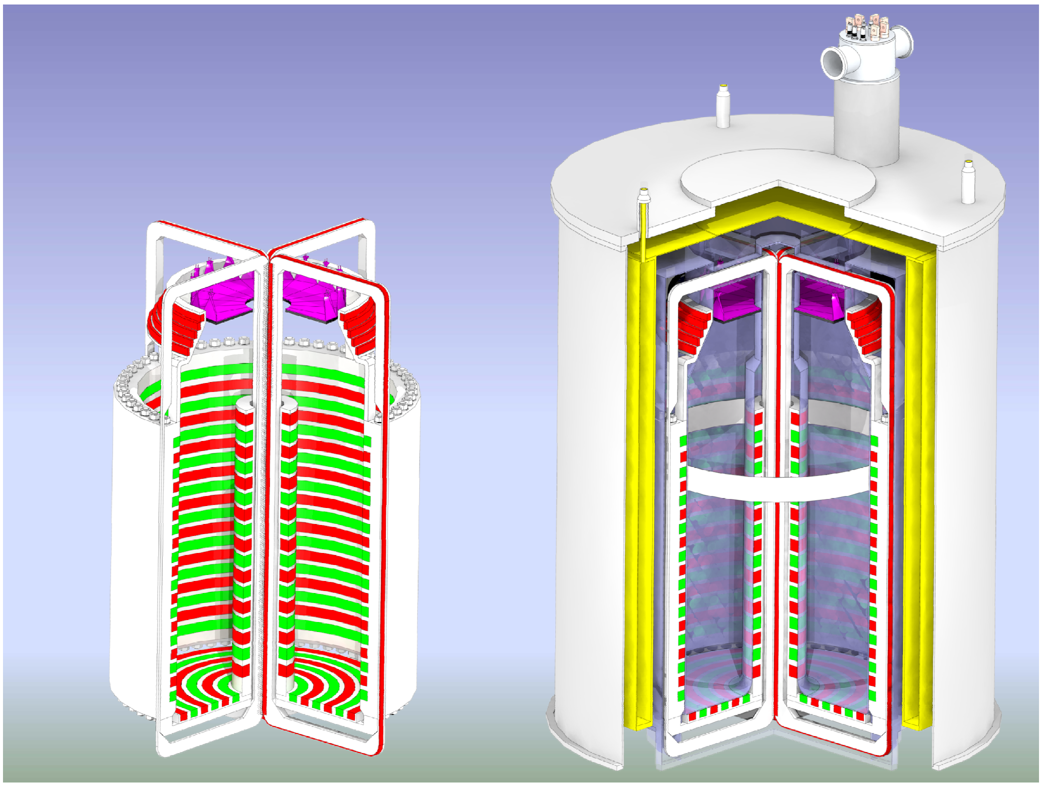

Figure 8.1: Cutaway view of coil support (left) and cryostat of PENeLOPE (right). Color code: Red, green: coils; white support structure; blue (transparent): helium cryostat; yellow: nitrogen shield; grey: vacuum vessel; purple: light guide of the proton detector.

and work on the coils and cryostat had to be outsourced: a feasibility study [SM05] and a cryostat design study [Mil07] were given out to Scientific Magnetics,[3] Culham, GB; their results shall be summarized here very briefly [SM05, Mil07]:

- The use of magnetic materials near the coils to shape the field does not yield a significant improvement in the usable field. Hence, air-coils are preferred for their convenience and magnetic materials shall be avoided in the vicinity.
- The conductor strand to be used shall be the CERN LHC inner strand, Cu-(Nb-Ti) with a ratio Cu to superconductor of 1.9 to 1 and a maximum current of 420 A.

---

[3] Scientific Magnetics was named Space Cryomagnetics until 2005.

- Ramping of the coils from zero to full current should be possible within 100 s.

- Protection against the destruction of the coils during a superconductor quench may be realized through magnet subdivision by resistor and diode networks.

- Cooling will be realized by immersing the coils in a liquid helium bath cryostat. The estimated heat load in the helium cryostat at 4.2 K is 5.5 W under static conditions but full current. During experiment runs, the magnets will be ramped approximately every 30 to 45 minutes and the averaged additional heat load will be 3.3 to 5 W.
  This results in a boil-off rate of 7.6 $\mathrm{dm}^3$ liquid helium per hour in static conditions under full current and additional 4.6 to 6.9 $\mathrm{dm}^3$ because of ramping. Hence, the estimated liquid helium consumption per experiment day is around $300 - 350\,\mathrm{dm}^3$.

- The power supply of the storage coils has to provide 33 kW and around 320 A. The racetrack coils need 250 A and 10 V.

- Coil support may be realized using an aluminum body held together by 60 aluminum bolts, see figure 8.1 (left).

- The critical part of the liquid helium cryostat is the access opening at the top, where the detector shall be installed. At the moment it has a radial clearance of 710 mm, but the four horizontal arms of the racetrack coils traverse this opening, making installations in the storage vessel tricky. Leaving out the focusing coils as discussed in chapter 4 could amend this situation.

- The annular gap to fill in the neutrons while the coils are demagnetized may have a clearance of 19 mm translating into a surface of more than 500 $\mathrm{cm}^2$. Using the approximative formula 2.5, the mean time to extract the neutrons assuming a mean velocity $\bar{v} = 2.8\ \mathrm{m/s}$ equals $\tau_{\mathrm{empt}} < 12\,\mathrm{s}$ with no magnetic field present in the trap.

Figure 8.2: Two test coils similar to the outer storage coils of PENeLOPE.

### 8.2.2 Coil test setup

In the feasibility study [SM05] it was also advised to build a demonstration magnet to confirm the coil support, quench protection and ramping schemes. Additionally the spatial distribution of the magnetic flux density shall be measured and compared to numerical results. In 2005 two coils on a scale of 0.8 of the outer storage coils of PENeLOPE were ordered and delivered together with the corresponding current leads in 2006. They are shown in figure 8.2 and represent a realistic scenario to test the criteria mentioned above. Cooling of the coils will realized by immersing them in liquid helium, held in an aluminum cryostat. All necessary parts have been delivered and are currently assembled; a first energization of the coils is expected in the second quarter of 2008.

# Chapter 9

# Summary and Outlook

The lifetime of the free neutron $\tau_n$ is an essential physics parameter. Its precise knowledge helps testing the Standard Model of particle physics, because together with the ratio of the weak coupling constants $\lambda = g_\mathrm{A}/g_\mathrm{V}$ the first element $V_\mathrm{ud}$ of the Cabibbo-Kobayashi-Maskawa quark-mixing matrix may be determined. This, in turn, is necessary to check the matrix for unitarity, which should be fulfilled if the three-generation Standard Model is valid.

Going back to some minutes after the Big Bang, the neutron lifetime also plays a vital role; after the universe had cooled down sufficiently, so that the conversion proton to neutron and vice versa was not in thermal equilibrium any more, neutron decay was the only reaction changing the proton over neutron ratio. If it were too short, in order for deuterium fusion to take over to tie the neutron to a proton and make it stable, the universe nowadays would consist purely of hydrogen, not a very pleasurable thought. Already small changes of the neutron lifetime alter the element composition of the universe today, most noticeably the helium abundance.

Being very long, around 15 minutes, measuring the lifetime has been a challenge since the discovery of the neutron by Chadwick in the 1930s and still is. Especially its lack of electric charge makes confining neutrons very hard. Therefore, the first lifetime experiments used neutron beams, thermal at first, from a reactor, then cold beams from a liquid deuterium converter and detected the decay products. Later in the 1960s with the discovery that ultra slow (or cold) neutrons (UCN) are reflected by certain materials under all angles of incidence, neutron storage experiments in material bottles became possible. Here the number of remaining neutrons was compared after different storage times to determine the lifetime. So the error bars shrank over the decades, but still not satisfactory, because both methods, beam and material storage, have their shortcomings. In the last years, UCN material bottles delivered the most precise results, however, the two most recent measurements disagree by more than $6\sigma$ (cf. chapter 2). Therefore, the last value $\tau_n = 878.7 \pm 0.8$ s [S+05] was not even included in the world average of the Particle Data Group $\tau_n = 886.5 \pm 0.8$ s because of this discrepancy [Y+06].

Hence, a more precise and preferably different measuring technique is required to resolve this: magnetic UCN storage. To this end, PENeLOPE, a magneto-gravitational trap was designed. Magnetic storage, exploiting the force on the magnetic moment ($\mu_\mathrm{n} = -60.3\,\mathrm{neV/T}$) in an inhomogeneous magnetic field, does not have the problem of losses at the material walls and is able to achieve much longer storage lifetimes for UCN. The only known loss mechanism is depolarization of the neutron if the adiabatic condition (equation 3.6) is not fulfilled. This is the case if the change of the magnetic field is too fast for spin reorientation. The magnetic field design of PENeLOPE guarantees adiabaticity, always providing a field large enough to compensate for the rotation of the flux vector. In this way, the spin-flip probability can be reduced orders of magnitude below values which would affect the desired precision for the neutron lifetime 0.1 s (cf. chapter 4).

The field is generated by superconducting coils in a vertical multipole configuration, leaving the top open, because UCN do not overcome the gravitational potential. This allows to extract the decay protons, guide them onto a detector and record the decay rate in real-time; a large area detector scheme has been devised and tested. In addition, the traditional storage measurement technique of counting remaining neutrons will also be applied. With a storage volume of around $700\,\mathrm{dm}^3$, a statistical precision of $\Delta\tau_\mathrm{stat} = 0.1$ s is reached within days at new strong UCN sources, so that the focus may lie on examining all possible systematic effects.

Extensive simulations of the particle behavior in the trap were performed with a self-written Monte Carlo code arriving at the following results (cf. chapter 4):

- The magnetic trap depth of PENeLOPE is 107.8 neV; above this value UCN will undergo wall collisions and losses are unavoidable.

- The collection efficiency for magnetically stored neutrons to a standard $^3$He detector is around 76 %.

- With a detector surface of 3050 $\mathrm{cm}^2$ the decay-proton detection efficiency may be as high as 76 %.

- Around 6 % of the UCN depolarized during magnetic storage may be collected.

- The use of focusing coils to scale down the proton detector should be reconsidered, as without them only 20 % more detector surface is needed, the proton extraction efficiency increased by at least 6 % and the system complexity decreases significantly.

One of the major systematic problems of magnetic storage are marginally trapped UCN, i.e. neutrons with an energy higher than the trap depth, but still a long survival time (cf. chapter 5). If a significant number of those existed in the trap, the measured lifetime would be systematically reduced. PENeLOPE will use an absorber ring, which is active during the filling period of the trap, when the coils are turned off and the magnetic field is low (cf. figure 8.1). After ramping up the coil current, the UCN cannot reach the absorber, because the magnetic field protects it. Reducing systematic effect in the system is essential to a precise neutron lifetime measurement, therefore a preexperiment, called AbEx, was designed, built and carried out to examine the power of the removal scheme: a cylindrical stainless-steel UCN trap in the form of a liquid helium cryostat was equipped with an absorber support structure that may be cooled down to around 4 K to simulate the condition of PENeLOPE during operation of the superconducting coils. Two ring-shaped absorber materials were tested at the Institut Laue-Langevin in Grenoble during two beam times at the UCN source. The results are:

- The ring-absorber scheme is powerful enough to remove high-energy UCN from the trap to reach our precision goal of $\Delta\tau_n < 0.1$ s.

- Both absorber materials can also be used at liquid helium temperature, as the temperature dependence of the complex Fermi potential $W_F$ is not essential as long as the absorber sheet is thick enough (cf. section 7.8).

- Cooling down the storage vessel is only efficient down to liquid nitrogen temperatures, below that, the storage lifetime does not rise significantly.

Another important test experiement has been built and is currently commissioned: a coil-test setup with two solenoids similar to the main storage coils of PENeLOPE to ascertain if the coils reach their nominal current and the aspired ramping-speed (zero to nominal current in around 100 s) is possible.

The engineering details of PENeLOPE have been addressed and a draft design of the coil support and the cryostat is ready. The next step is to develop the proton-extraction electrodes inside the storage volume necessary to collect protons emitted into the lower hemisphere, away from the detector.

The final technical design followed by the construction of the superconducting coil-system may be initiated as soon as the necessary funds are allocated and the first magnetic storage of ultra-cold neutrons in PENeLOPE achieved early in 2010.

# Appendix A

# Calculation of Derivatives Used For the 2-D Interpolation Routine of the Monte Carlo Code

Due to some ripple encountered in the derivative $\frac{\partial B_{r,z}}{\partial(r,z)}$ in the earlier version of the interpolation routine, calculation of the derivatives was refined from a second to a fourth order algorithm;

**Second order centered difference scheme:** The derivates and cross-derivatives of the magnetic flux density $B_\mathrm{r}$ or $B_\mathrm{z}$ at grid point ${}_{[j][k]}$ can be approximated by using the adjacent grid points

$$\begin{aligned}
\frac{\partial B_{r,z}}{\partial r}{}_{[j][k]} &= \frac{B_{r,z}{}_{[j+1][k]} - B_{r,z}{}_{[j-1][k]}}{r_{[j+1][k]} - r_{[j-1][k]}} \\
\frac{\partial B_{r,z}}{\partial z}{}_{[j][k]} &= \frac{B_{r,z}{}_{[j][k+1]} - B_{r,z}{}_{[j][k-1]}}{z_{[j][k+1]} - z_{[j][k-1]}} \\
\frac{\partial^2 B_{r,z}}{\partial r \partial z}{}_{[j][k]} &= \frac{B_{r,z}{}_{[j+1][k+1]} - B_{r,z}{}_{[j+1][k-1]} - B_{r,z}{}_{[j-1][k+1]} + B_{r,z}{}_{[j-1][k-1]}}{\left(r_{[j+1][k]} - r_{[j-1][k]}\right) \cdot \left(z_{[j][k+1]} - z_{[j][k-1]}\right)}.
\end{aligned}$$

**Fourth-order centered difference scheme:** A better estimation is achieved through using the next two grid points in both directions

$$\begin{aligned}
\frac{\partial B_{r,z}}{\partial r}[j][k] &= \frac{-B_{r,z}[j{+}2][k] + 8B_{r,z}[j{+}1][k] - 8B_{r,z}[j{-}1][k] + B_{r,z}[j{-}2][k]}{12(r[j][k] - r[j{-}1][k])} \\
\frac{\partial B_{r,z}}{\partial r}[j][k] &= \frac{-B_{r,z}[j][k{+}2] + 8B_{r,z}[j][k{+}1] - 8B_{r,z}[j][k{-}1] + B_{r,z}[j][k{-}2]}{12(z[j][k{+}1] - z[j][k])} \\
\frac{\partial^2 B_{r,z}}{\partial r \partial z}[j][k] &= \frac{1}{12(r[j][k] - r[j{-}1][k]) \cdot 12(z[j][k{+}1] - z[j][k])} \\
( \quad & B_{r,z}[j{+}2][k{+}2] - 8B_{r,z}[j{+}2][k{+}1] + 8B_{r,z}[j{+}2][k{-}1] - B_{r,z}[j{+}2][k{-}2] \\
- \quad & 8B_{r,z}[j{+}1][k{+}2] + 64B_{r,z}[j{+}1][k{+}1] - 64B_{r,z}[j{+}1][k{-}1] + 8B_{r,z}[j{+}1][k{-}2] \\
+ \quad & 8B_{r,z}[j{-}1][k{+}2] - 64B_{r,z}[j{-}1][k{+}1] + 64B_{r,z}[j{-}1][k{-}1] - 8B_{r,z}[j{-}1][k{-}2] \\
- \quad & B_{r,z}[j{-}2][k{+}2] + 8B_{r,z}[j{-}2][k{+}1] - 8B_{r,z}[j{-}2][k{-}1] + B_{r,z}[j{+}2][k{-}2] \quad ).
\end{aligned}$$

The result can be seen in figure A.1, where the interpolation along a vertical line is plotted and the version with second order centered differencing clearly shows the structure of the input table file with a grid-point distance of 2 mm.

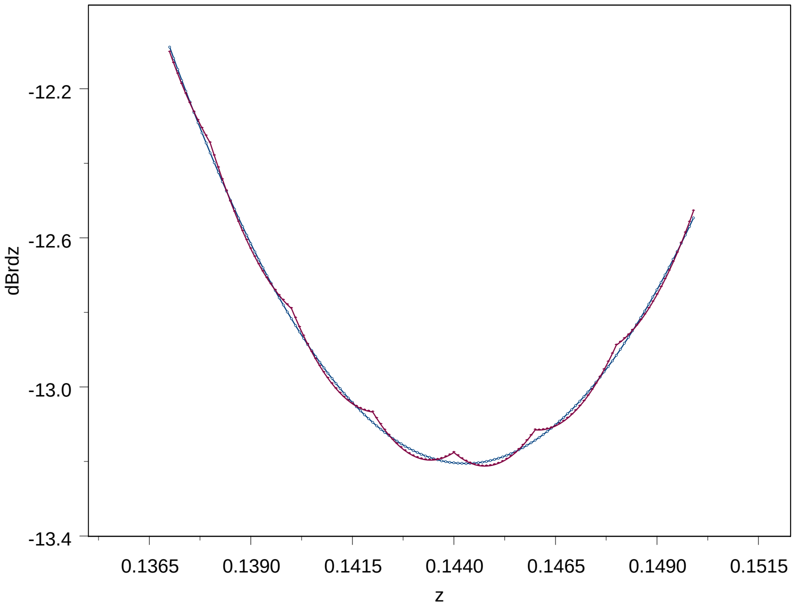

Figure A.1: Comparison of second and forth order centered differencing scheme: red curve: second order, blue curve: fourth order.

# Appendix B

# Ansatz for Spin-Tracking Suggested by Yuri Sobolev [Sob03]

The Bloch equation for a spin $S$ in the magnetic field is

$$\frac{d\mathbf{S}}{dt} = [\boldsymbol{\omega} \times \mathbf{S}]\,, \tag{B.1}$$

where $\boldsymbol{\omega} = \gamma_{\mathrm{n}} \cdot \mathbf{B}$ and the gyromagnetic ratio $\gamma_{\mathrm{n}} = 1.83247183(46) \times 10^{8}\,\mathrm{s}^{-1}\mathrm{T}^{-1}$. $\mathbf{S}$ is supposed to be a unity vector, $|\mathbf{S}| = 1$. In Cartesian coordinates, the cross product becomes

$$\begin{aligned} \dot{S}_x &= \omega_y S_z - \omega_z S_y \\ \dot{S}_y &= \omega_z S_x - \omega_x S_z \\ \dot{S}_z &= \omega_x S_y - \omega_y S_x . \end{aligned} \tag{B.2}$$

The vector $\mathbf{S}$ can also be expressed in cylindrical coordinates, where $S_x = S_\rho \sin\phi$ and $S_y = S_\rho \cos\phi$ and the derivatives

$$\begin{aligned} \dot{S}_x = \dot{S}_\rho\, \sin\phi + S_\rho\, \dot{\phi}\, \cos\phi \\ \dot{S}_y = \dot{S}_\rho\, \cos\phi - S_\rho\, \dot{\phi}\, \sin\phi . \end{aligned} \tag{B.3}$$

Setting equation (B.2) equal to (B.3), (B.3) equal to (B.4) and replacing the Cartesian by cylindrical coordinates leads to

$$\begin{aligned} &\dot{S}_\rho\, \sin\phi + S_\rho\, \dot{\phi}\, \cos\phi = \omega_y S_z - \omega_z S_y = \overbrace{(S_y)}\, \omega_y S_z - \omega_z S_\rho\, \cos\phi \\ &\dot{S}_\rho\, \cos\phi - S_\rho\, \dot{\phi}\, \sin\phi = \omega_z S_x - \omega_x S_z = \overbrace{(S_x)}\, \omega_z S_\rho\, \sin\phi - \omega_x S_z \\ &\dot{S}_z = \omega_x S_\rho \cos\phi - \omega_y S_\rho \sin\phi = \sqrt{1 - S_z^2}\, \left(\omega_x\, cos\phi - \omega_y\, \sin\phi\right), \end{aligned} \tag{B.4}$$

where $S_\rho = \sqrt{1-S_z^2}$.
Its derivative

$$\dot{S}_\rho = -\frac{S_z}{\sqrt{1-S_z^2}}\dot{S}_z$$

can be inserted, after equation (B.4) was solved for $\dot{\phi}$. After some simple conversions, the result is:

$$\dot{\phi} = -\omega_z + \frac{S_z}{\sqrt{1-S_z^2}}\left(\omega_y\, cos\phi + \omega_x\, \sin\phi\right)$$

Then the component of the Larmor precession in $z$-direction is added to the polar angle, which leads to the substitution $\Phi = \phi + \omega_z t$, so $\phi = \Phi - \omega_z t$ and $\dot{\phi} = \dot{\Phi} - \omega_z$. If the component of the Larmor precession parallel to the z-axis is constant, the time derivative is $\dot{\Phi} = \dot{\phi} + \omega_z$.
In general it is: $\dot{\Phi} = \dot{\phi} + \omega_z + \dot{\omega}_z t$. From now on we assume it to be constant.
Introducing this, the result is:

$$\begin{aligned} \dot{S}_z &= \sqrt{1-S_z^2}\left(\omega_x\, cos(\Phi - \omega_z t) - \omega_y\, \sin\left(\Phi - \omega_z t\right)\right) \\ \dot{\Phi} &= \frac{S_z}{\sqrt{1-S_z^2}}\left(\omega_y\, cos(\Phi - \omega_z t) + \omega_x\, \sin\left(\Phi - \omega_z t\right)\right) \end{aligned}$$

The components of the larmor precession $\omega_i$ can be calculated, when the components of the magnetic field are known in this Cartesian reference frame through $\omega_i = -\gamma_{\mathrm{n}} B_i$.
If there is a starting angle $\phi_0 > 0$, the total angle becomes $\phi = \Phi - \omega_z t + \phi_0$ and the equations transform to:

$$\begin{aligned} \dot{S}_z &= \sqrt{1-S_z^2}\left(\omega_x\, cos(\Phi - \omega_z t + \phi_0) - \omega_y\, \sin\left(\Phi - \omega_z t + \phi_0\right)\right) \\ \dot{\Phi} &= \frac{S_z}{\sqrt{1-S_z^2}}\left(\omega_y\, cos(\Phi - \omega_z t + \phi_0) + \omega_x\, \sin\left(\Phi - \omega_z t + \phi_0\right)\right) \end{aligned}$$

If this equation shall be integrated numerically, the starting values that have to be known are $S_z$ and $\phi_0$. $t$ and $\Phi$ are zero at the beginning of the integration. The $\omega_i$ have to be updated for every call of those equations by the integrator. When the integration is finished, the end values are $S_z$ and the total angle is as above $\phi = \Phi - \omega_z t + \phi_0$.
For the general case ($\omega_z$ not constant) the equations are:

$$\begin{aligned} \dot{S}_z &= \sqrt{1-S_z^2}\left(\omega_x\, cos(\Phi - \omega_z t + \phi_0) - \omega_y\, \sin\left(\Phi - \omega_z t + \phi_0\right)\right) \\ \dot{\Phi} &= \frac{S_z}{\sqrt{1-S_z^2}}\left(\omega_y\, cos(\Phi - \omega_z t + \phi_0) + \omega_x\, \sin\left(\Phi - \omega_z t + \phi_0\right)\right) + \dot{\omega}_z t \end{aligned}$$

# Appendix C

# Derivation of the Neutron Reflection Probability

In the quantum mechanics text book by F. Schwabl [Sch05], the transmission and reflection probabilities for a potential step $V$ without imaginary component is deduced. This formalism can be extended to a complex potential such as $V_\mathrm{F} = U_\mathrm{F} + iW_\mathrm{F}$: The reflection probability in [Sch05] is given by

$$r = \left| \frac{k-q}{k+q} \right|^2 ,$$

and the wave numbers

$$k = \sqrt{2mE}/\hbar \quad \text{and} \quad q = \sqrt{2m(E - V_\mathrm{F})}/\hbar .$$

Taking the absolute value of a fraction with several square roots and complex numbers is quite a lengthy task, which was performed with the help of Maple[1] resulting in

$$r = \frac{U_\mathrm{F}^2 + W_\mathrm{F}^2}{\left[ E + \sqrt{2E \cdot \left(\sqrt{(E-U_\mathrm{F})^2 + W_\mathrm{F}^2} + E - U\right)} + \sqrt{(E-U_\mathrm{F})^2 + W_\mathrm{F}^2} \right]^2} .$$

Substituting $Q = \sqrt{(E-U_\mathrm{F})^2 + W_\mathrm{F}^2}$ leads to equation 6.4.

---

[1] Maplesoft Maple 10.

# Appendix D

# ILL Research Proposal 3-14-204

# ILL RESEARCH PROPOSAL

Printed : 22/11/2006

Experiment Title : **Characterisation of absorber proper ties and material storage capabilit ies at liquid helium temperature fo r PENeLOPE**

Proposal Number

**3-14-204**

Proposer (to whom correspondence will be addressed)

| Name and first name | Address | Phone / Fax / Email |
|---|---|---|
| **PICKER Ruediger** | **DEPT PHYS E18, TU MUENCHEN**<br>TU MUENCHEN<br>JAMES-FRANCK-STRASSE<br>85748 Garching bei München<br>ALLEMAGNE | +49 89 289 12 484<br>+49 89 289 12 570<br>rpicker@e18.physik.tu-muenchen.de |

New neutron user? **No**
New ILL user? **No**

Co-proposers (mark the main proposer in each laboratory with an asterisk)

| Name and first name | Laboratory | Country |
|---|---|---|
| **GUTSMIEDL Erwin** | **DEPT PHYS, TU MUENCHEN, GARCHING** | **Allemagne** |
| **AMOS Peter** | **DEPT PHYS E18, TU MUENCHEN** | **Allemagne** |
| **MÜLLER Axel Reimer** | **DEPT PHYS E18, TU MUENCHEN** | **Allemagne** |
| **HARTMANN Joachim *** | **DEPT PHYS, TU MUENCHEN, GARCHING** | **Allemagne** |
| **PAUL Stefan** | **DEPT PHYS, TU MUENCHEN, GARCHING** | **Allemagne** |
| **GELTENBORT Peter *** | **ILL, GRENOBLE** | **France** |
| **ALTAREV Igor *** | **DEPT PHYS, TU MUENCHEN, GARCHING** | **Allemagne** |

Local contact(s) : **GELTENBORT Peter**

Suggested keyword number **3-14**

This proposal is :

[ x ] A new proposal.
[ ] A continuation proposal.
[ ] A resubmission.

The main research area of your proposal is

[ ] Biology [ ] Chemistry [ ] Physics [ ] Materials [x] Methods and instrumentation
[ ] Engineering [ ] Soft condensed matter [ ] Other :

Industry : **NOT Related to industrial applications**

| Instrument required | Days | |
|---|---|---|
| **PF2 UCN** | **30** | UCN beam with enough space and access from above, < one cycle |

Requested starting time :

| | | |
|---|---|---|
| 1. Jan/Feb | 2. Mar/Apr | 3. May/Jun |
| 4. Jul/Aug | 5. Sep/Oct | 6. Nov/Dec **x** |

Unacceptable Dates : **before Octobre**

Sample availability

## Sample description

Substance/Formula :

|  |  |  |  |
|---|---|---|---|
| Mass (in mg) : |  | Size (in mm3) : |  |
| State : |  |  |  |
| Surface area : |  | Space group : |  |
| Unit cell dimension : | a = | b = | c = |
| T (k) = | $\alpha$ = | $\beta$ = | $\gamma$ = |
| Sample container : |  |  |  |

## Safety aspects

The sample is : **CRYOGENICS DEVICE SUPPLIED BY USER (RISK)**

Is there any danger associated with the proposed sample or its preparation at ILL ?

[ ] Yes [ ] Uncertain [x] No If Yes or Uncertain, please give details of the risks asociated :

Is the sample a transuranium sample [ ] Yes [x] No

## Experimental details

Energy / wavelength range : **< 100 neV**

Resolution in energy or wavelength : **1 neV**

Range of momentum transfer :

Resolution in momentum transfer :

## Sample environment equipement (supplied by ILL)

Environment equipment : **device supplied by user (extern)**

Temperature range (stability) : **4.2K - 300K** Pressure range : **0 - 1 bar**

Magnetic-field strength (stability) **-**

Is there any danger associated with ancillary equipement ? [ ] Yes [x] Uncertain [ ] No

If Yes or Uncertain, please give details of the risks associated :

**Helium Bath Cryostat**

## To be filled in by ILL

| Sample environment code | Comments by Health Physics Officer and Safety Engineer |
|---|---|
| **EXT** |  |

## Abstract

With the planned experiment PENeLOPE, which will utilise real-time decay-proton detection of magnetically stored UCN, we envisage a measurement of the neutron lifetime with an accuracy of around 0.1 s.

In order to achieve this, the knowledge of all systematic effects is crucial, the experiment will not be limited by statistics. As already made clear by the magnetic storage experiment for UCN conducted at NIST, a key issue are marginally trapped neutrons, which have a kinetic energy higher than the trap depth, but still have a lifetime in the trap comparable to the decay-lifetime.

These neutrons shall be removed by absorbing them during the material wall storage phase of PENeLOPE, before the magnetic field is ramped up. In the proposed pre-experiment this scheme will be tested, especially at liquid helium temperatures: In a (cooled) storage volume of around 300 l we want to mount different (cooled) absorber materials at different heights, perform a storage experiment and measure the integral UCN spectrum above threshold. This shall be achieved by installing a rotatable "U" between the storage volume and the detector.

**scientific background and detailed description of the proposed experiment, see also guidelines**
*(please respect the available space)*

The neutron lifetime $\tau_{\rm n}$ plays a vital role in understanding big bang cosmology by influencing the relative abundance of primordial helium in the early universe. $\tau_{\rm n}$ also opens the way to determine the coupling constants of weak interaction and hence the element $V_{\rm ud}$ of the CKM matrix precisely. Latest experimental results indicate this matrix to deviate from unitarity by about 3 $\sigma$ and therefore challenges the three-generation standard model. The most precise measurements of $\tau_{\rm n}$ n were performed by storing ultra-cold neutrons (UCN) in material bottles. There are, however, losses during the many wall collisions whose nature is not yet fully understood. Therefore systematic errors cannot be decreased much below their present values. The $6\sigma$ difference between the world average for $\tau_{\rm n}$ from the PDG [1] and the latest experimental result [2] is a strong indication for such problems. Magnetic storage has recently been proven to be a viable alternative [3].

In the planned lifetime measurement PENeLOPE the volume between two nested cylinders made from magnetic multipole fields is used to store the UCN. Filling and emptying of the neutrons is realized through a slit in the outer bottom corner while the storage-coil current is ramped down. $\tau_{\rm n}$ shall be measured by real-time detection of decay protons as well as by counting the integral number of neutrons after varying storage times. The proton detector, a CsI scintillator, is situated on top of the storage volume; the decay protons are accelerated and focused onto it through a potential difference in the storage volume and an additional focusing coil around the detector. Depolarized neutrons shall also be monitored; they are not stored magnetically, but can still be collected when the inner walls of the trap are covered with a neutron reflecting material like diamond-like carbon. Using the UCN source at the ILL it may be possible to store up to $10^7$ neutrons per cycle in the experiment. Hence, the measuring time to get sufficient statistics is short and runs under many different conditions can be realized to investigate the systematics of the device. We thus envisage a relative accuracy for $\tau_{\rm n}$ of $10^{-4}$.

In order to achieve this, it is crucial to investigate *all* systematic effects. It is known throughout the UCN community that marginally trapped neutrons are a major source for decreasing the neutron storage-time: UCN with a slightly larger energy than the trap depth might have trajectories to stay in the trap on time scales comparable to the decay lifetime. PENeLOPE will have a depth of around $110\,$neV, so it is necessary to remove neutrons with higher energies. This shall be managed after filling the trap while the magnetic field is still very low. During this time an absorber installed at the walls at a height corresponding to $80\,$neV shall eat all marginal UCN. When the coil current is ramped up, the neutrons will not reach this absorber any more, but they will be heated by up to $30\,$neV. So if the absorbing scheme is perfect, we should not have UCN above $110\,$neV.

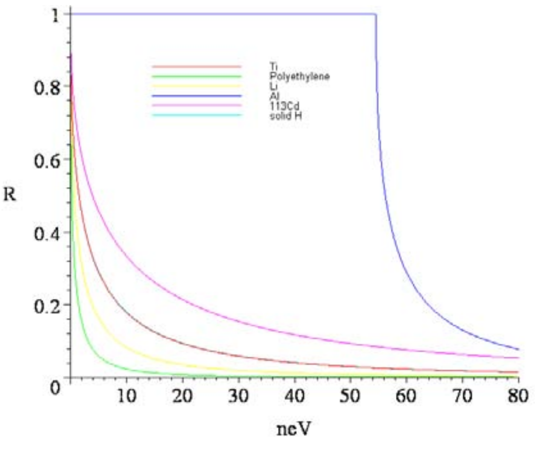

Fig. 1: Reflection probabilities of different absorbing materials

This may very well be not the case. As theory predicts, absorbers with non-zero real *and* imaginary parts V and W, respectively, of the Fermi potential may show a significant reflection probability for UCN at kinetic energies well above the real part of the Fermi potential. It may be seen from figure 1 that for titanium, a widely used absorber with $V+i\cdot W=(-50.76+i\cdot 0.025)$ neV, the reflection probability at $80$ neV is still $10\%$. The curves in this figure where obtained by solving the complex potential step problem quantum mechanically. Monte Carlo simulations incorporating these findings showed that a non-neglible fraction of UCN that hit the absorber still may survive the cleaning period, especially those that possess a relatively low kinetic energy when hitting the absorber (see figure 2, next page). This behavior of absorbers was also observed by several other experiments [4], but not studied in detail yet.

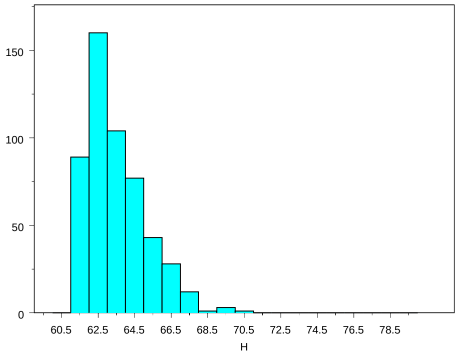

Fig. 2: Surving marginal UCN out of 30000 (Absorber height: $0.6$ m), H: kinetic energy [neV]

At the ILL PF2 UCN source, we would like to make a storage experiment which simulates the situation of PENeLOPE during the cleaning phase and allows to confirm or reject the theoretical assumptions concerning absorbers.

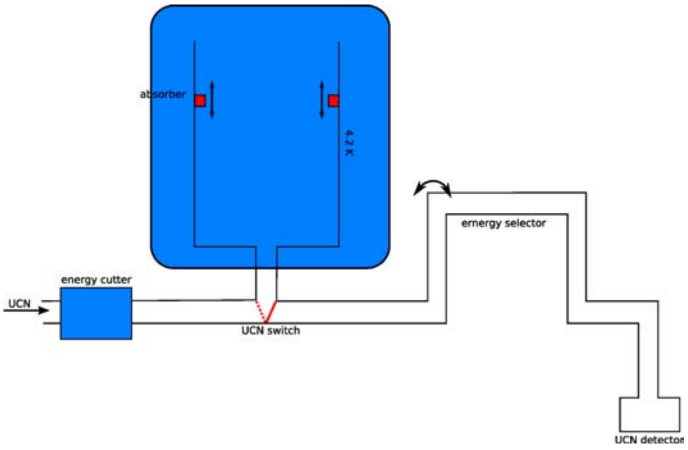

Fig. 3: experimental setup (not to scale)

A relatively large cylindrical storage volume with walls at $4.2\,$K shall be filled with UCN and an absorber ring shall be put at different heights at its outer walls. As can be seen in figure 3, the UCN spectrum shall be cleaned of neutrons with $E_{\mathrm{kin}} > 160\,$neV by a multireflection box with stainless-steel walls. A UCN switch shall then guide the neutrons either to the storage volume or from this volume to the detector (a $^3$He counter or a PIN diode with Li converter). A helium bath cryostat will cool the walls and with that the absorber down to around $4.2\,$K. In front of the detector a rotatable ”U” selects only UCN above a threshold energy corresponding to the height of the upper part of the ”U”. With this setup, the integral UCN spectrum can be recorded and hence the energy-dependent absorbing power of our scheme tested. Furthermore, different absorber shapes, heights and materials will be analysed to come up with the most effective scheme to absorb UCN above a certain energy.

A helium bath cryostat, which is used for testing coils comparable to the ones to be used in PENeLOPE, may be modified for this experiment to incorporate a cylindrical storage volume that can be filled from the bottom. The integrating nature of the storage-spectrometer requires sufficient statistics and additional set-up time is needed because of cryogenics. Therefore 30 days of beamtime will be necessary.

[1] S. Eidelman et al. (Particle Data Group), Phys. Lett. B **592**, 1 (2004) and 2005 partial update for 2006 (URL: http://pdg.lbl.gov).
[2] A. Serebrov et al., Phys. Lett. B **605**, 72 (2005).
[3] V. Ezhov et al., J. Res. Natl. Inst. Stand. Technol. **110**, 345-350 (2005).
[4] V. V. Nesvizhevsky et al., Phys. Rev. D **67**, 102002 (2003)

# Publication

22/11/2006

|  |  |  |  |
|---|---|---|---|
| **Proposal:** | **3-14-204** | **Council:** | 4/2006 |

**Title:** Characterisation of absorber properties and material storage capabilities at liquid helium temperature for PENeLOPE

**This proposal is a new proposal**

**Research Area:** Methods and instrumentation

**Industry:** **Not related to industrial application**

**Main proposer:** **PICKER Ruediger**

TU MUENCHEN
PHYSIK DEPARTMENT E18
JAMES-FRANCK STR
D-85748
GARCHING

Phone: +49 89 289 12 484
Fax: +49 89 289 12 570
E-mail: rpicker@e18.physik.tu-muenchen.de

New neutron user? No
New ILL user? No

**Local Contact:** GELTENBORT Peter

| Instrument | Req. Days |
|---|---|
| PF2 UCN | 30 |

**Publication:**

R. Picker et al., J. Res. Natl. Inst. Stand. Technol. 110, 357-360 (2005)

# Appendix E

# ILL Research Proposal 3-14-227

# ILL RESEARCH PROPOSAL

Printed : 18/07/2007

Experiment Title : **Continuation of AbEx to test storage and absorber characteristics at low temperatures**

Proposal Number

**3-14-227**

Proposer (to whom correspondence will be addressed)

| Name and first name | Address | Phone / Fax / Email |
|---|---|---|
| **PICKER Ruediger** | **DEPT PHYS E18, TU MUENCHEN**<br>TU MUENCHEN<br>JAMES-FRANCK-STRASSE<br>85748 Garching bei München<br>ALLEMAGNE | +49 89 289 12 484<br>+49 89 289 12 570<br>rpicker@e18.physik.tu-muenchen.de<br>New neutron user? **No**<br>New ILL user? **No** |

Co-proposers (mark the main proposer in each laboratory with an asterisk)

| Name and first name | Laboratory | Country |
|---|---|---|
| **PAUL Stefan** | **DEPT PHYS, TU MUENCHEN, GARCHING** | **Allemagne** |
| **ALTAREV Igor** | **DEPT PHYS, TU MUENCHEN, GARCHING** | **Allemagne** |
| **WIRTH Hans-Friedrich** | **DEPT PHYS, TU MUENCHEN, GARCHING** | **Allemagne** |
| **GELTENBORT Peter** | **ILL, GRENOBLE** | **Institut Laue-Langevin** |
| **MUELLER Axel Reimer** | **DEPT PHYS, TU MUENCHEN, GARCHING** | **Allemagne** |
| **BITTNER Bernhard** | **DEPT PHYS, TU MUENCHEN, GARCHING** | **Allemagne** |
| **HARTMANN Joachim** | **DEPT PHYS, TU MUENCHEN, GARCHING** | **Allemagne** |
| **GUTSMIEDL Erwin** | **DEPT PHYS, TU MUENCHEN, GARCHING** | **Allemagne** |
| **FRANKE Beatrice** | **DEPT PHYS E18, TU MUENCHEN** | **Allemagne** |

Local contact(s) : **GELTENBORT Peter**
**PLONKA Christian**

Suggested keyword number **3-14**

This proposal is :

[ ] A new proposal.
[x] A continuation proposal. Previous proposal number **3-14-204**
[ ] A resubmission.

The main research area of your proposal is

[ ] Biology [ ] Chemistry [x] Physics [ ] Materials [ ] Methods and instrumentation
[ ] Engineering [ ] Soft condensed matter [ ] Other :

Industry : **NOT Related to industrial applications**

| Instrument required | Days | |
|---|---|---|
| **PF2 UCN** | **21** | possible program: absorber tests 8 days, DLC 5 days, oxygen 8 days |

Requested starting time :

| | | |
|---|---|---|
| 1. Jan/Feb | 2. Mar/Apr | 3. May/Jun |
| 4. Jul/Aug | 5. Sep/Oct **x** | 6. Nov/Dec **x** |

Unacceptable Dates :

Sample availability

## Sample description

Substance/Formula :

Mass (in mg) : Size (in mm3) :

State :

Surface area : Space group :

Unit cell dimension : a = b = c =

T (k) = α = β = γ =

Sample container :

## Safety aspects

The sample is : **CRYOGENICS DEVICE SUPPLIED BY USER (RISK)**

Is there any danger associated with the proposed sample or its preparation at ILL ?

[ ] Yes [ ] Uncertain [x] No If Yes or Uncertain, please give details of the risks asociated :

Is the sample a transuranium sample [ ] Yes [x] No

## Experimental details

Energy / wavelength range : **neV**

Resolution in energy or wavelength : **neV**

Range of momentum transfer :

Resolution in momentum transfer :

## Sample environment equipement (supplied by ILL)

Environment equipment : **liquid nitrogen, liquid helium**

Temperature range (stability) : **4 to 293 K** Pressure range : **1e-7 mbar to 1.5 bar**

Magnetic-field strength (stability)

Is there any danger associated with ancillary equipement ? [ ] Yes [ ] Uncertain [x] No

If Yes or Uncertain, please give details of the risks associated :

## To be filled in by ILL

| | |
|---|---|
| Sample environment code<br>**X** | Comments by Health Physics Officer and Safety Engineer |

## Abstract

With the planned experiment PENeLOPE, which will utilise real-time decay-proton detection of magnetically stored UCN, we envisage a measurement of the neutron lifetime with an accuracy of around 0.1 s. In order to achieve this, the knowledge of all systematic effects is crucial. The experiment will not be limited by statistics. As already made clear by the magnetic storage experiment for UCN conducted at NIST, a key issue are marginally trapped neutrons, which have a kinetic energy higher than the trap depth, but still have a lifetime in the trap comparable to the decay lifetime. These neutrons shall be removed by absorbing them during the material wall storage phase of PENeLOPE, before the magnetic field is ramped up. The scheme was tested successfully in the beam time last December, but more statistics shall be collected and additional aspects shall be investigated. These will include DLC and frozen oxygen as storage material and also a multi-layer absorber structure.

## scientific background and detailed description of the proposed experiment, see also guidelines

*(please respect the available space)*

The neutron lifetime $\tau_\mathrm{n}$ plays a vital role in understanding Big Bang cosmology by influencing the relative abundance of primordial helium in the early universe. $\tau_\mathrm{n}$ also opens the way to determine the coupling constants of weak interaction and hence the element $V_\mathrm{ud}$ of the CKM matrix precisely. The most precise measurements of $\tau_\mathrm{n}$ were performed by storing ultra-cold neutrons (UCN) in material bottles. There are, however, losses during the many wall collisions, which are is not yet fully understood. Therefore systematic errors cannot be decreased much below their present values. The $6\sigma$ difference between the world average for $\tau_\mathrm{n}$ from the PDG [1] and the latest experimental result [2] is a strong indication for such problems. Magnetic storage has recently been proven to be a viable alternative [3].

In the planned lifetime measurement PENeLOPE the volume between two nested cylinders made from magnetic multipole fields is used to store the UCN. $\tau_\mathrm{n}$ shall be measured by real-time detection of decay protons as well as by counting the integral number of surviving neutrons after different storage times. The proton detector, probably a CsI scintillator, is situated on top of the storage volume; the decay protons are accelerated and focused onto it through a potential difference in the storage volume and an additional focusing coil around the detector. Using the UCN source at ILL it may be possible to store up to $10^7$ neutrons per cycle. Hence, the measuring time to get sufficient statistics is short and runs under many different conditions can be realized to investigate the systematics of the device. We envisage a relative accuracy for $\tau_\mathrm{n}$ of $10^{-4}$.

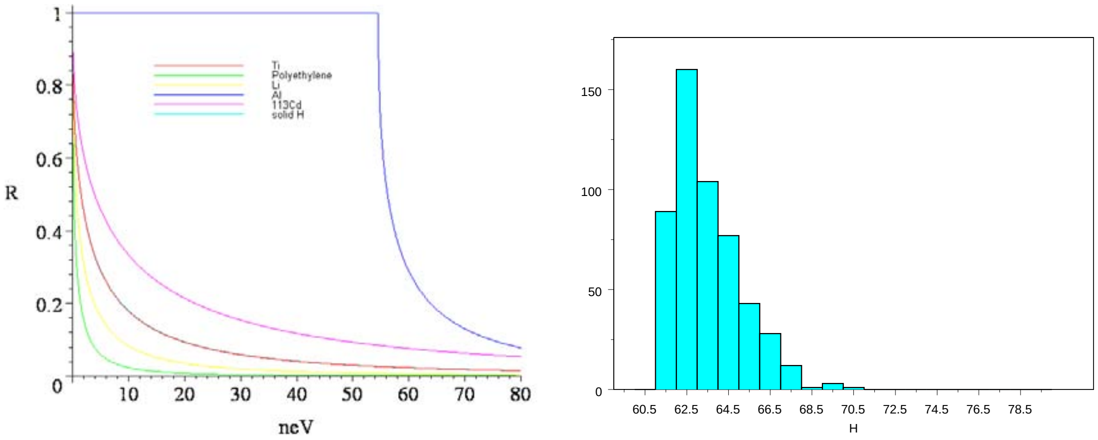

Fig. 1: (left) Reflection probabilities of different absorbing materials - (right) surviving marginal UCN out of 30000 (absorber height: 0.6 m), H: kinetic energy [neV]

In order to achieve this, it is crucial to investigate *all* systematic effects. It is known throughout the UCN community that marginally trapped neutrons are a major source for decreasing the neutron storage-time: UCN with a slightly larger energy than the trap depth might have trajectories to stay in the trap on time scales comparable to the decay lifetime. PENeLOPE will have a depth of around $110\,\mathrm{neV}$, so it is necessary to remove neutrons with higher energies. This shall be managed after filling the trap while the magnetic field is still very low. During this time an absorber ring of $10\,\mathrm{cm}$ height installed at the walls at a height corresponding to $80\,\mathrm{neV}$ shall eat all marginal UCN. When the coil current is ramped up, the neutrons will not reach this absorber any more, but they will be heated by up to $30\,\mathrm{neV}$. So, if the absorbing scheme is perfect, we should not have UCN above $110\,\mathrm{neV}$. This may very well be not the case. As theory predicts, absorbers with non-zero real *and* imaginary parts, V and W, respectively, of the Fermi potential may show a significant reflection probability for UCN at kinetic energies well above the real part of the Fermi potential. It may be seen from Figure 1 (left) that for titanium, a widely used absorber with $V + i \cdot W = (-50.76 + i \cdot 0.025)\,\mathrm{neV}$, the reflection probability at $80\,\mathrm{neV}$ is still $10\%$. The curves in this figure where obtained by solving the complex potential-step problem quantum mechanically. Monte Carlo simulations incorporating these findings showed that a non-negligible fraction of UCN that hit the absorber still may survive the cleaning period, especially those that possess a relatively low kinetic energy when hitting the absorber (see Figure 1, right). This behavior of absorbers was also observed by several

other experiments [4], but not studied in detail yet.
In December 2006 we conducted an experiment at the UCN turbine on Niveau D at ILL called AbEx (3-14-204) do study systematically how efficient this absorber scheme really is.

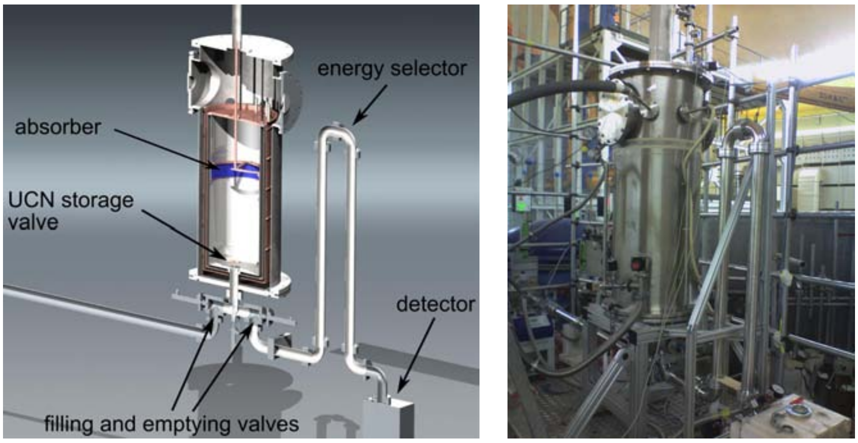

Fig. 2: (left) Cut-away view of the AbEx cryostat - (right) experimental setup on the UCN plattform

An electro-polished stainless-steel helium-bath cryostat with an inner diameter 400 mm and a height of 1000 mm is surrounded by a flow-through liquid-nitrogen shield made of copper. The absorbers (titanium and polyethylene in our case) are mounted on a support frame made of copper and have a height of 100 mm at a radius of 190 mm. A linear drive allows to move it along almost the total height of the storage bottle. Storage of neutrons is assured by closing the filling hole at the bottom center with a bath-tub-plug like neutron valve (UCN storage valve in Fig. 2 (left)). In order to connect the storage volume either to the UCN turbine or to the $^3$He detector two additional neutron valves are located below the cryostat. Energy selection of UCN is performed via a rotatable 'U' made of electro-polished UCN guides, so only UCN above a certain energy can reach the detector. The storage walls and the absorbers can be cooled down to either liquid-nitrogen or liquid-helium temperature, so one can measure at three different temperature values.
During the beamtime of 20 days, data could be taken for 382 hours or 15.9 days, which resulted in approx. $4.1 \cdot 10^7$ counted UCN. The neutron storage time in the bottle without absorber could be determined energy dependent at all three temperature points. Due to the increased heat input, PE as absorber material could only be measured down to $80$ K, but with Ti we could reach temperatures down to $5$ K by mounting it directly onto the storage walls.
The detailed data analysis is not finished yet, but one can already state, that the ring shape of the absorber was proven to be as effective as a whole horizontal disc of absorbing material in the storage volume: The storage time of UCN with a kinetic energy high enough to reach the absorber at its current height was always lower than $10$ s. This results in a reduction of marginally trapped neutrons to a level of $< 10^{-4}$ after $100$ s of cleaning time, which is sufficient for the aspired accuracy of PENeLOPE.
Due to the limited time available the heat input problem could not be solved, therefore statistics at liquid-helium temperature is limited and we want to continue measuring with this very versatile setup: First of all to get data on PE below $80\,$K and generally more statistics, secondly we also want to investigate a DLC-coated PET foil, and its UCN loss rate at low temperatures. Thirdly oxygen, which is known to have a very low UCN loss rate ($\mu \approx 6.1 \pm 0.6 \cdot 10^{-6}$) [5], may be frozen out on the steel walls of the storage vessel. Both materials may be used for material storage during the filling and cleaning phase of PENeLOPE, so it is vital to test their feasibility. We apply for three weeks of beam-time at the PF2 UCN position.

[1] W.-M. Yao *et al.*, J. Phys. G **33**, 1 (2006) (URL: http://pdg.lbl.gov).
[2] A. Serebrov *et al.*, Phys. Lett. B **605**, 72 (2005).
[3] V. Ezhov *et al.*, J. Res. Natl. Inst. Stand. Technol. **110**, 345-350 (2005).
[4] V. V. Nesvizhevsky *et al.*, Phys. Rev. D **67**, 102002 (2003)
[5] V. Nesvizhevskii, A. Serebrov, R. Taldaev *et al.*, Sov. Phys. JETP 75, 740 (1992).

# Publication

18/07/2007

**Proposal:** **3-14-227** **Council:** 4/2007

**Title:** Continuation of AbEx to test storage and absorber characteristics at low temperatures

**This proposal is continuation of: 3-14-204**

**Researh Area:** Physics

**Industry:** **Not related to industrial application**

**Main proposer:** **PICKER Ruediger**

TU MUENCHEN
PHYSIK DEPARTMENT E18
JAMES-FRANCK STR
D-85748
GARCHING

Phone: +49 89 289 12 484
Fax: +49 89 289 12 570
E-mail: rpicker@e18.physik.tu-muenchen.de

New neutron user? No
New ILL user? No

**Local Contact:** GELTENBORT Peter
PLONKA Christian

| Instrument | Req. Days |
|---|---|
| PF2 UCN | 21 |

**Publication:**

# Appendix F

# Complete Fit Function for One Storage Cycle of AbEx

Expression 7.2 can be integrated analytically to

$$
\begin{aligned}
I_{\mathrm{BG}} &= \left[-\tau_{\mathrm{s1}} N_{\mathrm{s1}} \cdot e^{-\frac{t-T_{\mathrm{ss}}}{\tau_{\mathrm{s1}}}} - \tau_{\mathrm{s2}} N_{\mathrm{s2}} \cdot e^{-\frac{t-T_{\mathrm{ss}}}{\tau_{\mathrm{s2}}}}\right]_{T_1}^{T_2} \\
I_{\mathrm{BGa}} &= -\tau_{\mathrm{s1}} N_{\mathrm{s1}} \cdot \left[e^{\frac{T_2-T_{\mathrm{ss}}}{\tau_{\mathrm{s1}}}} - e^{-\frac{T_1-T_{\mathrm{ss}}}{\tau_{\mathrm{s1}}}}\right] - \tau_{\mathrm{s2}} N_{\mathrm{s2}} \cdot \left[e^{-\frac{T_2-T_{\mathrm{ss}}}{\tau_{\mathrm{s2}}}} - e^{-\frac{T_1-T_{\mathrm{ss}}}{\tau_{\mathrm{s2}}}}\right]
\end{aligned}
$$

and the fit function finally comes to

$$
\begin{aligned}
F_{\mathrm{f}} = B_{\mathrm{c}} &+ \frac{\Delta_{\mathrm{BG}}}{I_{\mathrm{BGa}}} \left[\cdot N_{\mathrm{s1}} \cdot e^{-\frac{t-T_{\mathrm{ss}}}{\tau_{\mathrm{s1}}}} + N_{\mathrm{s2}} \cdot e^{-\frac{t-T_{\mathrm{ss}}}{\tau_{\mathrm{s2}}}}\right. \\
&+ \left. \Theta(x - T_{\mathrm{cs}}) N_{\mathrm{c}} \cdot e^{-\frac{t-T_{\mathrm{cs}}}{\tau_{\mathrm{cf}}}} \left(1 - e^{-\frac{t-T_{\mathrm{cs}}}{\tau_{\mathrm{cr}}}}\right)\right].
\end{aligned}
$$

Here, the fit procedures of ROOT determine the uncertainty in $\Delta_{\mathrm{BG}}$ which is equal to the error of $I_{\mathrm{BG}}$.

# List of Figures

# List of Tables

# Bibliography

[A$^+$00] S. Arzumanov et al. *Phys. Lett. B*, 483:15–22, 2000.

[A$^+$04] H. Abele et al. Quark mixing, CKM unitarity. *Eur. Phys. J. C*, 33:1–8, 2004.

[B$^+$99] S. Burles et al. Sharpening the predictions of Big-Bang nucleosynthesis. *Phys. Rev. Lett.*, 82(21):4176–4179, 1999.

[B$^+$00] Th. Brenner et al. Looking for surface states of ultra-cold neutrons. *Nucl. Instrum Methods A*, 440(3):722–728, 2000.

[B$^+$02] S. Baessler et al. The neutron decay spectrometer aspect. In H. Abele and D. Mund, editors, *Quark-Mixing, CKM-Unitarity*, pages 81–85, Heidelberg, 2002. Mattes Verlag.

[Brö04] J. Bröcker. Quellen systematischer Fehler bei der Messung der Neutronen-Lebensdauer mit einer magnetischen Flasche. Diploma thesis, TU Munich, November 2004.

[Byr97] J. Byrne. *Neutrons, Nuclei and Matter*. Institute of Physics Publishing, Bristol and Philadelphia, 1997.

[Byr02] J. Byrne. An overview of neutron decay. In H. Abele and D. Mund, editors, *Quark-Mixing, CKM-Unitarity*, pages 21–34, Heidelberg, 2002. Mattes Verlag.

[E$^+$05] V.F. Ezhov. et al. First ever storage of ultracold neutrons in a magnetic trap mad of permanent magnets. *J. Res. Natl. Inst. Stand. Technol.*, 110:345–350, 2005.

[G$^+$91] R. Golub et al. *Ultra-cold Neutrons*. Adam Hilger, Bristol, 1991.

[G$^+$01] A. Garcia et al. *Phys. Lett. B*, 500:66, 2001.

[GGL02] A. Garcia and J. Garcia-Luna. *Phys. Lett. B*, 546:247, 2002.

[H$^+$02] K. Hagiwara et al. *Particle Physics Booklet*. AIP, 2002.

[HL05] R.E. Hill and C.-Y. Liu. Temperature-dependent neutron scattering cross-sections for polyethylene. *Nucl.Instrum. Methods A*, 538:686–691, 2005.

[Ign90] V. K. Ignatovich. *The Physics of Ultracold Neutrons*. Clarendon Press, Oxford, 1990.

[M$^+$03] F. Mezei et al., editors. *Neutron Spin Echo Spectroscopy*. Springer, Berlin, 2003.

[M$^+$05] G.J. Mathews et al. Big bang nucleosynthesis with a new neutron lifetime. *Phys. Rev. D*, 71(021302(R)), 2005.

[M$^+$07a] A. Mann et al. A flexible advanced tca based sampling adc system for multimodality positron emission tomography. In *15th IEEE-NPSS Real-Time Conference*, volume N25-1, 2007.

[M$^+$07b] A.R. Müller et al. Paff, a low-energy, low-flux proton accelerator for detector tests. *Nucl.Instrum. Methods A*, 2007.

[Mat73] M. Matora. Probability of spin rotation of a non relativistic particle in a inhomogenious magnetic field. *Sov. J. Nucl. Phys.*, 16(3):349, 1973.

[Mee03] D. Meeker. Finite element method magnetics. `http://femm.foster-miller.net/`, 2003.

[Mil07] S. Milward. Cryostat report. Technical report, Scientific Magnetics, August 2007.

[MN98] M. Matsumoto and T. Nishimura. Mersenne twister: A 623-dimensionally equidistributed uniform pseudorandom number generator. In *ACM Trans. Modeling Computer Simulation*, volume 8, January 1998. p. 3-30.

[Mül08] A.-R. Müller, 2008. Private communication.

[Nac68] O. Nachtmann. Relativistic corrections to the recoil spectrum in neutron $\beta$-decay. *Z. Phys.*, 215:505–514, 1968.

[NS05] Jeffrey S. Nico and W.Michael Snow. Fundamental neutron physics. *Annu. Rev. Nucl. Part. Sci.*, 55:27–69, 2005.

[$P^+92$] W. H. Press et al. *Numerical Recipes in C.* Cambridge University Press, Cambridge, second edition, 1992.

[$P^+03$] B. Povh et al. *Particles and Nuclei.* Springer, Berlin, 5th edition, 2003.

[Pic04] R. Picker. A new superconducting magnetic trap for ultra-cold neutrons. Diploma thesis, TU Munich, June 2004.

[$S^+98$] A. P. Serebrov et al. *J. Exp. Theor. Phys.*, 86:1074, 1998.

[$S^+04$] T. Soldner et al. New limit on t violation in neutron decay. *Phys. Lett. B*, 581(1-2):49–55, February 2004.

[$S^+05$] A. Serebrov et al. *Phys. Lett. B*, 605:72–78, 2005.

[$S^+07$] D.N. Spergel et al. Three-year wilkinson microwave anisotropy probe (WMAP) observations: Implications for cosmology. *Astrophys. J. Suppl. Ser.*, 170:377–408, 2007.

[Sch05] F. Schwabl. *Quantenmechanik I.* Springer, Berlin, 6 edition, 2005. Korrigierter Nachdruck 2005.

[Sea92] V. F. Sears. Neutron scattering length and cross section. *Neutron News*, 3, 1992.

[SM05] R. Rajput-Ghoshal S. Milward. Neutron storage vessel feasibility. Technical report, Space Magnetics, January 2005.

[SO01] H. Shimizu and T. Oku. *J. Phys. Soc. Jpn.*, (20):431–435, 2001. Suppl. A.

[Sob03] I. Sobolev, 2003. Private communication.

[Tor07] D. Tortorella. Characterization of a solid deuterium converter for ucn in the framework of the mini-d2 project at the frm-ii reactor in munich. Phd thesis, TU Munich, February 2007.

[Vla61] V. V. Vladimirskii. *Sov. Phys. JETP*, 12:740, April 1961.

[Wei84] S. Weinberg. *The first three minutes.* Bantam Books, 1984.

[$Y^+92$] H. Yoshiki et al. Observation of ultracold-neutron production by $9 - \AA$ cold neutrons in superfluid helium. *Phys. Rev. Lett.*, 68:1323–1326, 1992.

[$Y^+06$] W.-M. Yao et al. *J. Phys. G*, 33(1), 2006. and 2007 partial update for edition 2008.

[Zel59] Y. Zel'dovich. *Sov. Phys. JETP*, 9:683, 1959.

[Zim00] O. Zimmer. A method of magnetic storage of ultra-cold neutrons for a precise measurement of the neutron lifetim. *J. Phys. G*, 26:67–77, 2000.

# Index

## Own Contributions

I began at E18 as a working student in 2002 and was immediately involved in the neutron lifetime project. At this time the permanent magnet solution was favored and I started out with optimizing the magnet layout using the finite element program FEMM [Mee03]. In my diploma thesis from June 2003 on, the focus was set on optimizing a superconducting coil setup for neutron storage and proton extraction as well as advancing the Monte Carlo simulation software described in chapter 4: after determining the final magnet layout, many aspects important for the particles present in a UCN storage experiment were simulated.

With the start of my PhD thesis, the physics simulations were continued with special focus on neutron spin tracking. From that moment on, the construction details became important, a company to build the magnet was found and I was in close contact with them during the feasibility and design study as well as the production of the test coil pair.

In 2006 my idea to test the absorber scheme of PENeLOPE (AbEx) was approved by Prof. Stephan Paul, I submitted an application to the Institut Laue-Langevin and we received beam time at the UCN source there. During 2006 and 2007 I was responsible for design and construction of AbEx, conducted the tests in Munich and was the experiment responsible during the beam-times at the ILL.

Thereafter, I carried out the data analysis of AbEx, which had to be started from scratch.

## Acknowledgements

My first acknowledgment goes to Stephan Paul because it was the casual atmosphere at E18 he had created that made me stay here for my whole research life up to now. In the last seven years I enjoyed very much working with all the interesting people he gathered at the institute. He also puts trust in these people letting them explore their own ideas and visions, but also encourages them to use their full capabilities. I will always keep one statement in mind, he told me last year, because it is true: "You work best when you're under pressure."

To Joachim Hartmann I am especially indebted, from the first day I came to E18, he was and is always the one I can come to when I have any question, be it physics or other. I hope he will share his lore and experience for many more years with people at the institute.

Further thanks goes to Axel Müller my office-mate for keeping a pleasurable atmosphere in the office and sometimes not saving his files...

For helping design and construct AbEx my appreciation goes to Peter Amos for the great engineering drawings he made and Rainer Stoepler for his skill in negotiating with the industry, but especially to Thomas Deuschle and Herbert Ruhland because without their support and dedication AbEx would never have flown.

For their participation and shift taking at ILL during the AbEx beam-times I thank Bea Franke, Hans-Friedrich Wirth and especially Igor Altarev for his UCN wisdom.

Thanks to Stefan Materne, who strengthened the lifetime work force at E18 and took over the coil test setup, so I had time to write my thesis.

The last, but not at all the least acknowledgment goes to my parents, for helping me grow up, always supporting me in every way and, most of all, giving me the feeling that they are there when I need them.